Local structure and lattice dynamics study of low dimensional materials using atomic pair distribution function and high energy resolution inelastic x-ray scattering

Chenyang Shi

Submitted in partial fulfillment of the

requirements for the degree

of Doctor of Philosophy

in the Graduate School of Arts and Sciences

COLUMBIA UNIVERSITY

2015

ABSTRACT

Local structure and lattice dynamics study of low dimensional materials using atomic pair distribution function and high energy resolution inelastic x-ray scattering

Chenyang Shi

Structure and dynamics lie at the heart of the materials science. A detailed knowledge of both subjects would be foundational in understanding the materials' properties and predicting their potential applications. However, the task becomes increasingly difficult as the particle size is reduced to the nanometer scale. For nanostructured materials their laboratory x-ray scattering patterns are overlapped and broadened, making structure determination impossible. Atomic pair distribution function technique based on either synchrotron x-ray or neutron scattering data is known as the tool of choice for probing local structures. However, to solve the "structure problem" in low-dimensional materials with PDF is still challenging. For example for 2D materials of interest in this thesis the crystallographic modeling approach often yields unphysical thermal factors along stacking direction where new chemical intuitions about their actual structures and new modeling methodology/program are needed. Beyond this, lattice dynamical investigations on nanosized particles are extremely difficult. Laboratory tools such as Raman and infra-red only probe phonons at Brillouin zone center. Although in literature there are a great number of theoretical studies of their vibrational properties based on either empirical force fields or density functional theory, various approximations made in theories make the theoretical predictions less reliable. Also, there lacks the direct experimental results that can be used to validate the theories.

In this thesis, we studied the structure and dynamics of a wide variety of technologically relevant

low-dimensional materials through synchrotron based x-ray PDF and high energy resolution inelastic x-ray scattering (HERIX) techniques. By collecting PDF data and employing advanced modeling program such as DiffPy-CMI, we successfully determined the atomic structures of (i) emerging Ti_3C_2, Nb_4C_3 MXenes (transition metal carbides and/or nitrides) that are promising for energy storage applications, and of (ii) zirconium phenylphosphonate ion exchange materials that are proposed to separate lanthanide ions from actinide ions in nuclear waste. Both material systems have two-dimensional layered nanocrystalline structure where we observed that the stacking of layers are not in good registry, also known as "turbostratic" disorder. Consequently the signals from a single layer of atoms dominate the experimental PDF–thus building up a single slab model and simulating PDF using Debye function analysis was sufficient to capture the main structural features in the measured PDF data. The information on correlation length of layers along the stacking direction, however, is contained in low-Q diffraction peaks in either laboratory x-ray or synchrotron x-ray scattering patterns.

On the lattice dynamics side, we first investigated the trend of atomic bonding strength in size dependent platinum nanoparticles based on temperature dependent PDF data and measured Debye temperatures. An anomalous bond softening was observed at a particle size less than 2 nm. Since Debye model gives a simple quadratic phonon density of states (PDOS) curve, which is a simplified version of real lattice dynamics, we are motivated to measure full PDOS curves on three CdSe nanoclusters by using non-resonant inelastic x-ray scattering technique. We observed an overall blue-shift of PDOS curves with decreased sizes. Our current exemplary studies will open the door to a large number of future structural and lattice dynamical studies on a much broader range of low-dimensional material systems.

Table of Contents

List of Figures

List of Tables

Acknowledgments

It's a thrill to arrive at this moment and years of hard work pays off. To finally get to this point, help and guidance from many teachers and friends are of crucial importance and I am truly grateful to everyone of them.

First of all, my special thanks go to my PhD adviser Prof. Simon Billinge. It is him who led me into the wonderful world of local structure and pair distribution function (PDF). Simon is a world-renowned expert on PDF with extremely busy schedule yet he always managed to and has been incredibly patient on advising me on how to think like a real scientist. I have been enjoying every of our discussion that often leads to new ideas or guidance for attacking the scientific problems at frontier. Having him as my adviser is my life-long fortune.

I would like to thank all my thesis examination committee members for attending my thesis defense from their busy schedules and for providing constructive comments/suggestions on my thesis. My sincere gratitude goes to Prof. Yury Gogotsi from Drexel University, Profs. Siu-Wai Chan and Irving Herman at Columbia University and Dr. Emil Božin from Brookhaven National Laboratory.

Dr. Pavol Juhás is like my second adviser. Each time I encountered technical difficulty in PDF, I resorted to him. And each time he addressed the problem in a most articulate and professional manner. After he moved to Brookhaven National Lab to start his new scientific endeavor, we continued to exchange ideas through emails. It's Pavol who helps me maintain my enthusiast on PDF, without terrified by the daunting technical details and programming puzzles.

I am grateful to Dr. Yan Li who worked at Brookhaven National Laboratory and is now an

editor for *Physical Review* journals. I appreciated her hard work and expertise on DFT. I enjoyed extensive discussion with her on the CdSe projects we have been working on in the past two years. Without her, the last chapter of the thesis would not be possible.

I would like to thank Dr. Milinda Abeykoon for his help on setting up countless PDF experiments at beamline X17A at National Synchrotron Light Source (NSLS), whether it be room temperature measurement or low temperature one using cryostream/cryostat. I and many others in the group benefited a lot from his professional knowledge and veteran experience on synchrotron instruments. Whenever there was a malfunction during experiment, simply a call to him would solve it. With Milinda as our beam scientist, the synchrotron experiment is never intimidating anymore.

Equally, the helps and supports from other members in and outside the Billinge group are much appreciated. They are Jin Wang, Kirsten Jensen, Max Terban, Soham Banerjee, Xiaohao Yang, Ben Frandsen, Chris Gutiérrez, Chris Farrow, Baruch Tabanpour, Karim Mukaddem, Alex Beecher, Profs. Jonathan Owen, James Im, William Bailey, Katayun Barmak, Chris Marianetti and Cevdet Noyan at Columbia Univeristy; Drs. Kevin Knox, Yong Cai, Eric Dooryhee, Sanjit Ghose at Brookhaven National Laboratory; Drs. Ayman Said, Bogdan Leu and Dillon Fong at Argonne National Laboratory; Michael Naguib, Majid Beidaghi, Babak Anasori at Drexel University and Rita Silbernagel, Prof. Abraham Clearfield at Texas A&M University.

Finally, I am deeply indebted to my parents. It is your persistence and emphasis on education that makes the first Doctor in the family possible. I felt very proud and excited at the PhD graduation ceremony with your presence. No words could describe my gratitude to my wife Dr. Shuoshuo Han who recently obtained her PhD degree in Geophysics from Columbia. It has always been your continuous and gracious love and support that sustain me to move ahead in study and life.

To my family

Part I

Main Text

Chapter 1

Introduction

In the past two decades, low-dimensional materials have been the center of focus of numerous research. These are functional materials with at least one of the three dimensions in the range of 1-100 nm. Due to surface effect [Ball and Garwin, 1992], quantum confinement effect [Goldstein *et al.*, 1992; Gu *et al.*, 2004], low-dimensional materials exhibit unique properties different from those of their bulk counterparts [Lu *et al.*, 2004; Alivisatos *et al.*, 1998; Alivisatos, 2004; Klimov *et al.*, 2007; Pandey and Guyot-Sionnest, 2008; Cossairt *et al.*, 2011]. In addition, the unique size dependent optoelectronic properties have made them ideal materials for a great number of applications such as highly efficient catalysis [Farrow *et al.*, 2013; Bediako *et al.*, 2012; McAlpin *et al.*, 2010; Lutterman *et al.*, 2009], bio-labeling [Chan and Nie, 1998; Chan *et al.*, 2004] and functionalization [Schroedter *et al.*, 2002; Gu *et al.*, 2003], novel luminescent materials [Fafard *et al.*, 1996; Parala *et al.*, 2000; Beecher *et al.*, 2014] nonlinear optics [Johnson *et al.*, 2002; Wang *et al.*, 2005], chemical sensors [Fan *et al.*, 2000; Ghosh *et al.*, 2003] and super high density information storage [Kyratsi *et al.*, 2003]. Low-dimensional materials can be divided into $0D$ (quantum dots), $1D$ (quantum wire) and $2D$ (quantum well) materials, based on number of dimensions confined. In this thesis, since $2D$ and $0D$ materials have been studied, a brief overview of both systems are given in the following section.

1.1 A brief overview of low-dimensional materials

1.1.1 Two-dimensional materials

Talking about two-dimensional ($2D$) materials, graphene is perhaps the most well-known compound [Novoselov *et al.*, 2004]. Isolated from graphite in year 2004, graphene has attracted tremendous attention from researchers around the globe due to its exceptional properties such as half-integer quantum Hall effect, extremely high carrier mobility, high thermal conductivity, high specific surface area and highest strength ever measured. All these excellent properties make it the ideal material for a wide variety of applications in nanotechnology [Geim and Novoselov, 2007; Singh *et al.*, 2011; Kuila *et al.*, 2012; Guo and Dong, 2011; Tang *et al.*, 2013]. The ever-lasting enthusiasm in graphene has also inspired scientists to explore other two-dimensional materials, comprising of single layer or few layers with compositions other than carbon. Indeed great progress has been made in searching for "graphene-analogous" materials [Tang and Zhou, 2013]. A number of emerging new $2D$ materials have been prepared and characterized. These include BC_3 [Ueno *et al.*, 2006], silicene [Kara *et al.*, 2012], MXene(transition metal carbides and nitrides, such as Ti_3C_2 [Lukatskaya *et al.*, 2013], Nb_4C_3 [Ghidiu *et al.*, 2014], V_2C, Nb_2C [Naguib *et al.*, 2013]), coordination polymers (such as $[Cu_2Br(IN)_2]_n$ [Amo-Ochoa *et al.*, 2010] and polymeric Fe-phthalocyanine [Abel *et al.*, 2011]). These novel $2D$ materials have very good properties and find themselves in various applications. For example the layered MXene materials whose structures have been studied in this thesis have shown great promise in technological applications. MXenes are a recently discovered large family of two-dimensional ($2D$) early transition metal carbides and/or nitrides that are extremely promising for applications in electronic device materials, sensors, conductive reinforcement additives to polymers, catalysis, and electrochemical energy storage materials [Naguib *et al.*, 2014; Naguib *et al.*, 2012a; Come *et al.*, 2012; Lukatskaya *et al.*, 2013].

1.1.1.1 Synthesis of $2D$ materials

Various experimental techniques have been applied to synthesize $2D$ materials. Micromechanical cleavage has proven an easy and fast way of obtaining highly crystalline atomically thin nanosheets. As originally used in peeling off graphene from graphite, the same technique has been extended to other graphene-analogous layered materials with weak van der Waals forces connecting the layers. The micromechanical cleavage was firstly applied to isolation of h-BN, MoS_2, $NbSe_2$, and $Ba_2Sr_2CaCu_2O_x$ [Novoselov *et al.*, 2005], and has been recently used to obtain nanosheets with 1 to 10 atomic layers thick of BN [Pacile *et al.*, 2008; Gorbachev *et al.*, 2011], MoS_2, $NbSe_2$, WSe_2 [Lee *et al.*, 2010], GaS, GaSe [Hu *et al.*, 2012; Late *et al.*, 2012], Bi_2Se_3 [Hossain *et al.*, 2011] and Bi_2Te_3 [Teweldebrhan *et al.*, 2010]. The disadvantage of this method is, however, the low yield of monolayer or thinner products.

Alternatively, chemical exfoliation such as liquid-phase exfoliation, and ion-intercalation induced exfoliation has been demonstrated to be able to effectively produce single layer products in large quantities. By using liquid-phase exfoliation, one first sonicates the layered bulk materials in polar solvents, surfactant or reaction reagents, and then exfoliate the resulting dispersions into thin layers with the help of centrifugation. A proper solvent should have a surface energy comparable to the van der Waals force of bulk materials, and be able to form stable dispersion with host materials against reaggregation. Till now using liquid-phase exfoliation technique $2D$ materials systems such as BN [Coleman *et al.*, 2011; Han *et al.*, 2008], WS_2, MoS_2, $MoSe_2$, $MoTe_2$, WSe_2 [Coleman *et al.*, 2011; O'Neill *et al.*, 2012; Matte *et al.*, 2011; Li *et al.*, 2013];VS_2, V_2O_5 [Feng *et al.*, 2012; Rui *et al.*, 2013] were reported. In comparison, ion-intercalation method is often used for exfoliating transition-metal dichalcogenides. The method starts with Li intercalation into layered bulk material, followed by subsequent exfoliation by immersing the Li-intercalated compounds in water by ultrasonication. This technique has been used to produce single-layer dichalcogenides of MoS_2, WS_2, TiS_2, TaS_2, and ZrS_2 [Zeng *et al.*, 2011]. The major difficulty comes from low Li concentration and a striking structural phase transformation after Li intercalation [Eda *et al.*, 2012].

Chemical vapor deposition (CVD) is another viable method for synthesis of $2D$ materials. This bottom-up self assembly method accompanies high-temperature chemical reactions of molecular precursors on a surface. The surface not only serves as a template but also catalyzes the epitaxial growth of solid films. The merit of this surface-assisted method is the production of clean single layer or few layers. By properly controlling different experimental conditions such as temperature and precursors used, synthesis of $2D$ materials such as BN [Shi *et al.*, 2010], hybrid h-BNC [Ci *et al.*, 2010] and MoS_2 [Zhan *et al.*, 2012] have been published.

As a modification of CVD method, surface-assisted epitaxial growth technique can be considered as molecular beam epitaxy (MBE) growth where the substrate surface serves as a seed crystal other than a template or a catalyst. This technique has been applied to fabricate one-atom-thick Si sheets (silicene) using Ag substrate [Padova *et al.*, 2011].

1.1.2 Zero-dimensional materials

Quantum dots (QDs) are semiconductor nanocrystals with size smaller than the characteristic Bohr radius, which is typically in the range of few to tens of nanometers, exhibiting size-dependent electronic and optical properties. CdSe QDs with high monodispersity have been prepared by Murray *et al.*, in 1993 that can emit at almost any visible wavelength [Murray *et al.*, 1993]. For diameters of CdSe QDs near or smaller than its Bohr radius of 5.6 nm, quantum confinement effect causes a larger band gap with decreasing size [Murray *et al.*, 1993]. QDs are zero-dimensional nanostructure with confinement in all three directions. Their electronic density of states exhibit discrete energy levels similar to atoms. Recent research on QDs include synthesis of II-IV, IV-VI, III-V, and group IV materials with band gap spanning from visible region to infrared [Murray *et al.*, 1993; Pietryga *et al.*, 2004; Lee *et al.*, 2009; Micic *et al.*, 1994]

1.1.2.1 Synthesis of quantum dots

Quantum dots can be synthesized through colloidal chemistry. As early as in year 1983, Rossetti *et al.* synthesized CdS QDs in aqueous solution and studied their quantum confinement effects [Ros-

setti *et al.*, 1983]. When utilizing size-dependent optical and electric properties of QDs, it requires a strict control of size distribution, and the synthesis of monodisperse QDs became significant for QD studies. In 1993, Murray *et al.* introduced hot-injection by mixing precursors at high temperature and controlling nanocrystals growth at a lower temperature [Murray *et al.*, 1993]. For a better size distribution, size selection technique was applied to obtain monodisperse CdSe QDs with less than 5% distribution. To avoid using pyrophoric dimethyl cadmium in the synthesis, a green precursor cadmium oxide with phosphonic acid was used by Peng *et al.* in 2001 [Peng and Peng, 2001]. With a less reactive precursor, the nucleation and growth regime can be well separated, resulting in better tunability in size and shape.

1.1.2.2 Surface passivation

For colloidal synthesis, strong binding ligands are used in order to stabilize QDs in solution and prevent QD aggregation. QDs surface chemistry plays a vital role in the optical and electronic properties, affecting the emission quantum yield and the band level energies of nanocrystals [Brown *et al.*, 2014]. For bare QDs, the surface atoms have unfilled dangling bonds. Passivation of QDs can be done in two ways, either by ligands or through bonding the surface atoms to another semiconductor material with a higher band gap, creating an abrupt potential wall on the surface [Alivisatos, 1996], which is known as "inorganic passivation". For QDs the surface is usually nonstoichiometric. A recent report suggests the surface composition of CdS QDs with either cation rich or anion rich stoichiometry could induce significant fluctuation of photoluminescence efficiency [Wei *et al.*, 2012]. A sulfur rich surface could introduce more trap sites, which produced centers for nonradiative relaxation while cadmium rich surfaces have been passivated for QDs, resulting a more stable bright emission.

1.1.2.3 QDs morphology control

For $0D$ semiconductor NCs, the shape could be approximated as spherical. However, as governed by kinetics during growth, high-energy facets can outgrow other facets, giving rises to asymmetric

growth of NCs [Bealing *et al.*, 2012]. For instance, in PbSe NCs, as the diameter increases, NCs undergo a morphology change from octahedron, through truncated octahedron, to cuboctahedron, to reduced cube, and finally cube where the binding ligand oleic acid plays an important role in the growth. Pietryga *et al.*, observed a spherical to cubic transition at 12 nm in diameter when preparing PbSe *QDs* [Pietryga *et al.*, 2004]. Such transition was also reported in PbTe *QDs* with a smaller transition size of 9.3 nm [Murphy *et al.*, 2006]. In this thesis, through well-controlled chemistry, the CdSe quantum dot nanoclusters were prepared to maintain an unique tetrahedral pyramid shape [Beecher *et al.*, 2014].

1.2 Why low-dimensional materials are different

1.2.1 Surface effects

In low-dimensional materials, surface atoms take up a large fraction of total atoms. These atoms have fewer nearest neighbors than atoms in the bulk, i.e. they are under-bonded. Since the surface area of a sphere is scaled as r^2, its volume is scaled as r^3, it is easy to find that the fraction of surface atoms or *dispersion* in a spherical particle is scaled as inverse of r. The same relation basically also holds for long cylinders of radius of r and for thin plates of thickness d [Roduner, 2006b]. The size dependence of *dispersion* is illustrated in left panel of Fig. 1.1 [Roduner, 2006a]. A series of materials' properties are found to follow this $1/r$ scaling law such as cohesive energy [Kohn *et al.*, 2001] as shown in the right panel of Fig. 1.1 and melting temperature [Unruh *et al.*, 1993; Koga *et al.*, 2004; Lai *et al.*, 1996].

1.2.2 Quantum confinement effects

The concept "quantum confinement" arises when the size of low-dimensional materials decreases to a value that is comparable to exciton Bohr radius. The direct consequence is that the electron energy level becomes discrete and the band gap opens up when compared with bulk matter. This can be explained quantitatively by considering the wavefunction and the energy level for a single

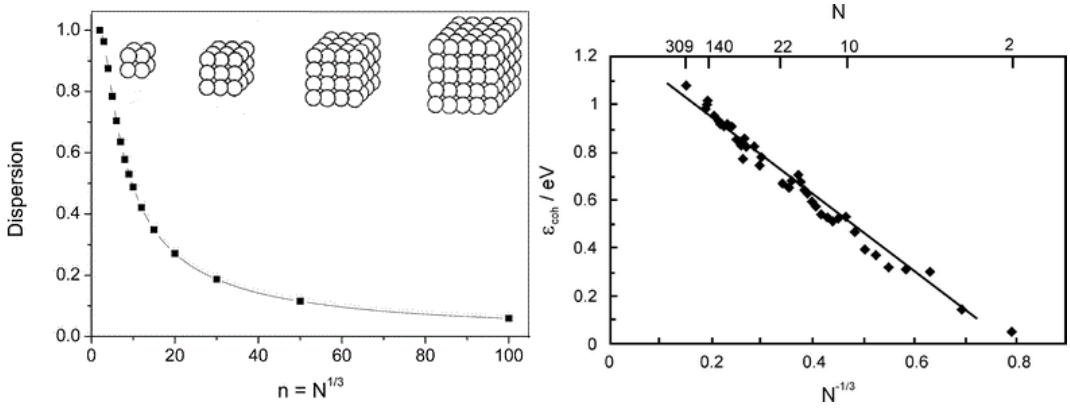

Figure 1.1: (left) Dispersion as a function of number of atoms n along each side for cubic clusters, total number $N = n^3$. (right) Cohesive energy as a function of size $N^{-1/3}$.

particle confined in a box as stated below,

$$\Psi_{n_x,n_y,n_z} = \sqrt{\frac{8}{L_x L_y L_z}} \sin\left(\frac{n_x \pi x}{L_x}\right)\left(\frac{n_y \pi y}{L_y}\right)\left(\frac{n_z \pi z}{L_z}\right) \tag{1.1}$$

$$E_{n_x,n_y,n_z} = \frac{\hbar^2 \pi^2}{2m}\left[\left(\frac{n_x}{L_x}\right)^2 + \left(\frac{n_y}{L_y}\right)^2 + \left(\frac{n_z}{L_z}\right)^2\right] \tag{1.2}$$

where L_x, L_y, L_z represent the lengths of box sides along three directions whereas n_x, n_y and n_z are the quantum numbers for an eigenstate. When $L_x = L_y = L_z \leq 2r_b$ (r_b, Bohr radius), the low-dimensional material is called a quantum dot; when $L_x = L_y \leq 2r_b \ll L_z$, it is referred to as a quantum wire; when $L_z \leq 2r_b \ll L_x = L_y$, it is a quantum well. Typical electronic density of states for low-dimensional materials is compared with bulk counterpart in Fig. 1.2 [Mino *et al.*, 2013]. Quantum confinement effect causes the electronic and optical properties of low-dimensional materials to deviate substantially from those of bulk materials.

1.3 Difficulties in studying structure and dynamics of low-dimensional materials

In pursuit of understanding material properties, and facilitating their technological applications, a detailed knowledge of the atomic scale structure and lattice dynamics is fundamental. The structure

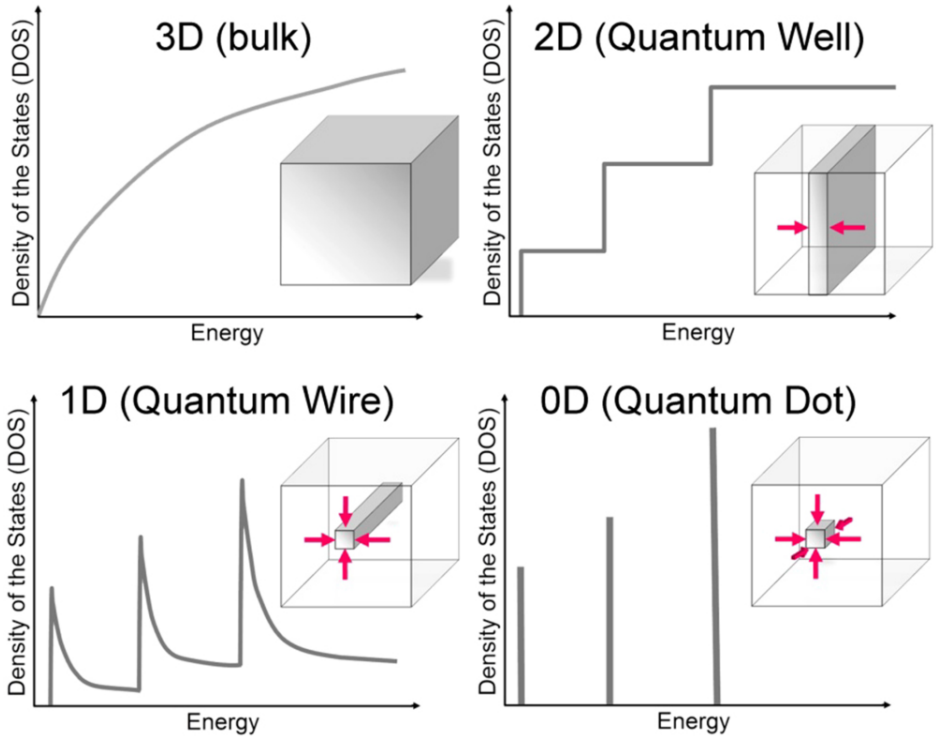

Figure 1.2: Electronic density of states for a bulk 3D crystalline material, a 2D quantum well, a 1D nanowire and a 0D quantum dot.

encodes information on how the atoms are stacked in the material that dictates the properties of materials system. Also important is a knowledge of the lattice dynamics of a material which gives detailed information about the atomic bonding in the system as well as many important properties such as heat and electrical transport, as well as information about anharmonicity and phase stability.

The study of structure and dynamics becomes increasingly difficult as the dimensions of materials are reduced. Consequently, fundamental questions such as "what are the structures of low-dimensional materials?" and "how does the atomic bonding change with particle size?" are unanswered except in special cases. These are difficult questions that are complicated by the materials' ultra-small sizes (typically less than 2 nm). For structural studies, when the structures extend only on the nanometer scale, traditional x-ray approaches yield broadened and overlapped Bragg peaks. This results in low information content in the diffraction data and, in general, insufficient for structure determination, sometimes referred to as the "nanostructure problem" [Billinge and Levin, 2007].

On the other hand, on the lattice dynamical side, inelastic neutron scattering (INS) is the tool of choice for investigating lattice dynamics of materials [Li *et al.*, 2011a; Frase *et al.*, 1998; Fultz *et al.*, 1996] since neutrons are penetrating; the momentum of neutrons allows them to probe phonons across several Brilloiun zones and the energy of thermal neutrons is comparable to the excitation energy of the phonons. However, INS has disadvantages for the study low-dimensional materials for at least two reasons. First, neutron experiments require a large quantity of sample, typically in the order of few grams, which can not be easily satisfied for most novel nanomaterials [Beecher *et al.*, 2014; Bediako *et al.*, 2012; Clearfield, 2008]. Second, for many important nanoparticles synthesized through a wet chemistry route, such as CdSe quantum dots, surface organic ligands are typically needed for stabilizing the core structure [Cossairt *et al.*, 2011; Beecher *et al.*, 2014]. In such cases the scattering signals are dominated by the incoherent hydrogen signals. This potentially excludes many technologically and scientifically important nanosystems. Laboratory tools such as Raman scattering [Rossetti *et al.*, 1983; Gorbachev *et al.*, 2011; Kim *et al.*,

2008; Purans *et al.*, 2007; Kelley *et al.*, 2013] are often applied to probe the vibrational properties of the materials. Raman scattering has a much higher resolution than inelastic neutron scattering, and the measurements are quick, suitable for studies as a function of external variables such as temperature or pressure [Dove, 2003]. However, because the wavelength of probing light is much longer than the interatomic spacings, Raman scattering only measures phonons with wavevectors close to zero, i.e., it only probes a subset of the optical modes (those satisfying the selection rules) at small momentum transfers at the Brillouin zone center. Infrared spectroscopy is another quick laboratory technique as Raman that involves an absorption process rather than phonon scattering interaction [Chen *et al.*, 2006; Dore *et al.*, 2004; Manaa, 2004; Alexandrov *et al.*, 1993]. Similar to Raman technique, infrared spectroscopy has selection rule (though different and complementary to Raman) and probes phonons at $k = 0$, thus it also fails to probe phonons at higher momentum transfer. Nuclear resonant inelastic x-ray scattering (NRIXS) that uses isotope resonators such as ^{57}Fe, ^{119}Sn, ^{151}Eu to achieve a better cross section has been used to study the vibrational properties in some nanosystems [Cuenya *et al.*, 2012; Cuenya *et al.*, 2011; Cuenya *et al.*, 2007; Cuenya *et al.*, 2009; Stankov *et al.*, 2008]. The basic idea is similar to inelastic x-ray scattering which will be discussed in details in Chapter Two of this thesis. The disadvantage of this technique is however, that particular resonators narrow down the number of materials that can be studied due to selectivity. Also, just like inelastic x-ray scattering technique, there is limited number of user facilities in the world.

On the theoretical side, lattice dynamics has been extensively studied by empirical interatomic force field (FF) [Rabani, 2002; Zhou *et al.*, 2013; Benkabou *et al.*, 2000; Lin *et al.*, 2014a; Han and Bester, 2011] or more accurately by *ab initio* density functional theory (DFT) [Stoffel *et al.*, 2010; Corso *et al.*, 1993; Kootstra *et al.*, 2000; Mohr and Thomsen, 2009; Sarasamak *et al.*, 2010; Han and Bester, 2012a; Han and Bester, 2012b]. The phonon eigenfrequencies ω and eigenvectors $a_{k\alpha}(\vec{\boldsymbol{q}})$ with wave vector $\vec{\boldsymbol{q}}$ can be calculated, within harmonic approximation, by solving the eigenstate

equation

$$\sum_{k'\beta} D^{k\alpha}_{k'\beta}(\vec{\boldsymbol{q}}) a_{k'\beta}(\vec{\boldsymbol{q}}) = \omega^2 a_{k\alpha}(\vec{\boldsymbol{q}}) \tag{1.3}$$

here D is dynamical matrix and given by the Fourier transform of force constant matrix

$$D^{k\alpha}_{k'\beta}(\vec{\boldsymbol{q}}) = \sum_{l} \frac{1}{\sqrt{m_k m_{k'}}} \frac{\partial^2 V}{\partial u_{0k\alpha} \partial u_{lk'\beta}} e^{i\boldsymbol{q}\boldsymbol{r}_l} \tag{1.4}$$

where l, k, α, m_k correspond to unit cell index, atomic index, Cartesian direction and mass of atom k, respectively. V is the potential energy and its second derivative with respect to atomic displacement $\frac{\partial^2 V}{\partial u_{0k\alpha} \partial u_{lk'\beta}}$ yields force constant matrix.

The difficulties for these simulations are as follows. Empirical force fields rely heavily on interatomic potentials which are typically derived from bulk properties such as elastic constants or phonon dispersion curves. Even for the same bulk material from which the potentials are derived, the empirical potentials can reproduce only a subset not all of materials properties. They become further inaccurate when applied to low-dimensional materials. Density functional theory, on the other hand, shows higher level of accuracy when compared with force fields method. However, the disadvantage of the DFT technique is its high demand of computation power. To simulate the vibrational properties of colloidal quantum dots capped by surface ligands, an approximation in theory such as using pseudohydrogens is often used [Han and Bester, 2012a; Han and Bester, 2012b; Han and Bester, 2011]. Since the actual weight of ligands is not always preciously known and is typically heavier than hydrogen, a simple approximation using hydrogen makes the simulated results less reliable.

1.4 Utilizing PDF and HERIX techniques to study structure and dynamics of low-dimensional materials

In this thesis, we studied the local structures of novel low-dimensional materials including MXene materials and zirconium phenylphosphonate (ZrPP) nanoparticles. MXene materials are recently discovered a new family of two-dimensional materials that show great promises in energy

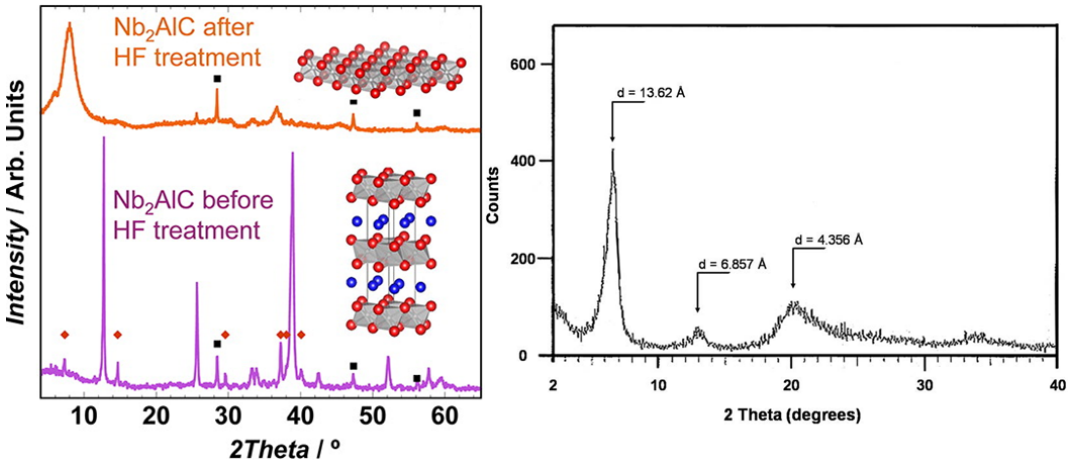

Figure 1.3: The laboratory x-ray diffraction pattern for Nb_2C MXene (left) and ZrPP (right).

storage application [Naguib *et al.*, 2014; Naguib *et al.*, 2012a; Come *et al.*, 2012; Lukatskaya *et al.*, 2013]. ZrPP samples happen to adopt layered structures. These materials are proposed to separate lanthanide ions from actinide ions in nuclear waste due to their unique selectivity towards +3 ions while having less affinity of lower charged ions [Burns *et al.*, 2012; Clearfield, 2008; Perry *et al.*, 2012]. More details on both materials systems will be introduced later in respective chapters (Chapter Three for MXene and Chapter Four for ZrPP).

To understand the performance of these systems, it is always the important first step to determine their structures. However, their laboratory x-ray diffraction patterns show little information except for few peaks corresponding to interlayer spacings (see Fig. 1.3) [Naguib *et al.*, 2013; Clearfield, 2008]. Quantitative intra-layer structural information is missing or impossible to be deduced. To tackle these problems, we used x-ray total scattering technique in combination with atomic pair distribution function (PDF). As opposed to Bragg scattering on nano systems, the PDF has well defined sharp peaks, giving rich information for structure determination. In search for structural solutions of these low-dimensional materials, DiffPy-CMI [Juhs *et al.*, 2015] modeling program is heavily relied on. It is a versatile software that allows many customized settings. In the thesis, I extensively applied a customized script "Cookiecutter" to create and model PDF of a single slab of atoms cut from the bulk crystalline materials. The script is designed to cut simple

geometry of nanoclusters out of bulk crystalline parent and then calculate its PDFs. A schematic of "Cookiecutter" is shown in Fig. 1.4

On the lattice dynamics side we first investigated the size dependent atomic bonding strenth of five carbon supported platinum nanoparticles. For bulk materials a single parameter such as Debye temperature may be used to quantify bond stiffness. To obtain Debye temperature it is common practice to collect temperature dependent x-ray diffraction (XRD) pattern and at each temperature to fit the measured pattern with a structure model to extract Debye-Waller (DW) factors. By fitting the temperature dependent DW factors with a Debye model [Debye, 1912], one obtains Debye temperature. However, the situation becomes complicated in nanosized materials. First the Bragg peaks are broadened or overlapped in laboratory XRD for nanomaterials; therefore accurate Debye-Waller factors cannot be obtained this way. Also, due to large number of underbonded atoms at surface, Debye temperature decreases with reduced size even if the bond stiffness stays the same. To address these issues, temperature dependent PDFs were collected to extract reliable thermal factors. Also "surface effect" of nanomaterials is accounted for when studying their atomic bonding strength. In platinum nanoparticle project we used a simple Debye model to explain the lattice dynamics but the real lattice dynamics can be better explained by full phonon density of states (PDOS). Looking at PDOS of GaAs [Jeong *et al.*, 2003] in Fig. 1.5, it is immediately obvious that Debye model is simplified as compared with real dynamics. Therefore in order to study lattice dynamics of low-dimensional materials, we should measure their full PDOS. In the thesis we took the initiative to map out PDOS of three "magic size" CdSe nanoclusters [Beecher *et al.*, 2014] using high energy resolution inelastic x-ray scattering (HERIX) technique. As far as we know, this is the first time PDOS of nanomaterials was measured using non-resonant inelastic x-ray scattering technique.

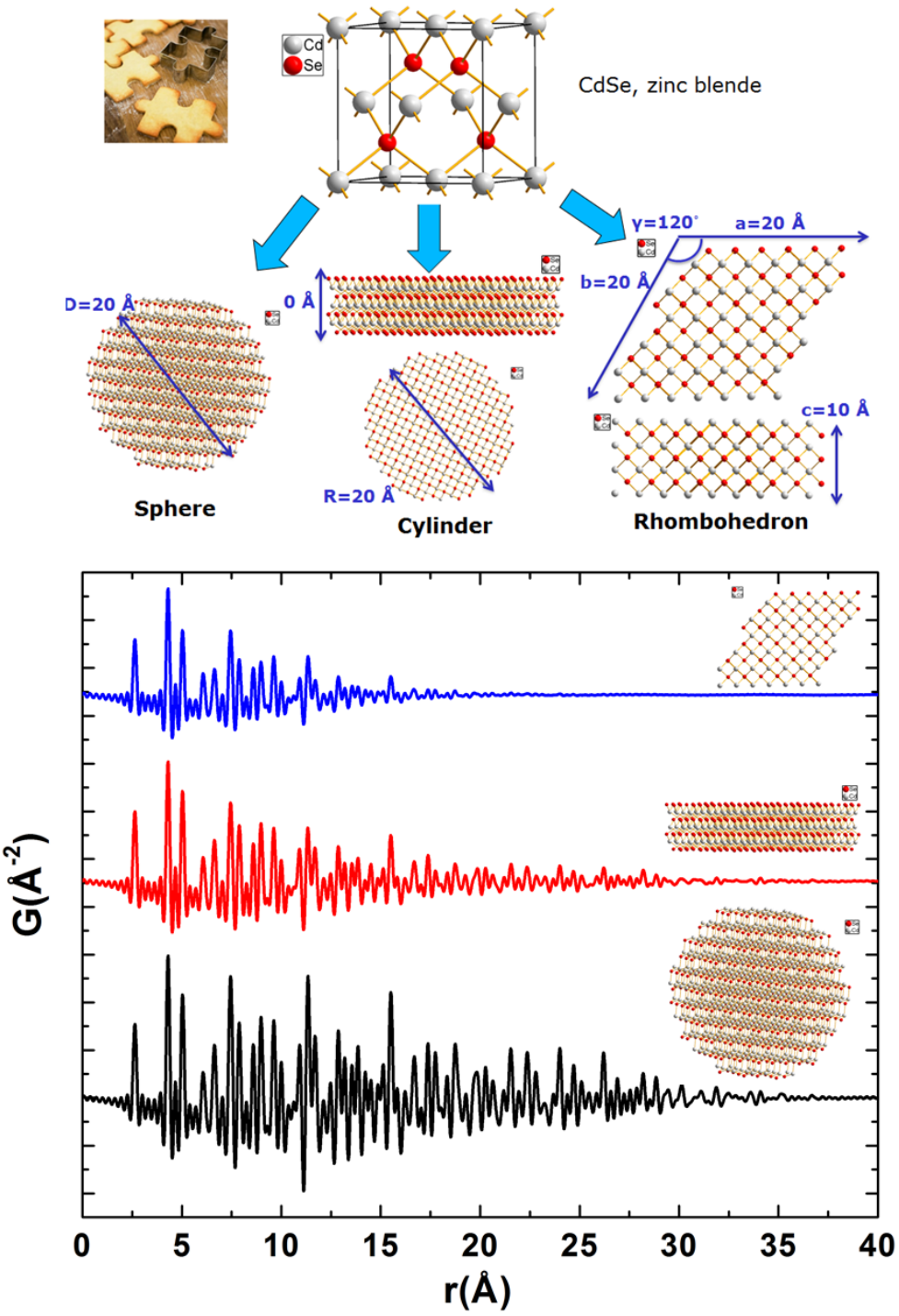

Figure 1.4: (top) Using "Cookiecutter" script, nanocrystals with spherical, cylindrical and rhombohedral shapes are easily cut out from bulk CdSe sample with a zinc blende structure. (bottom) Corresponding PDFs are calculated for simple geometries.

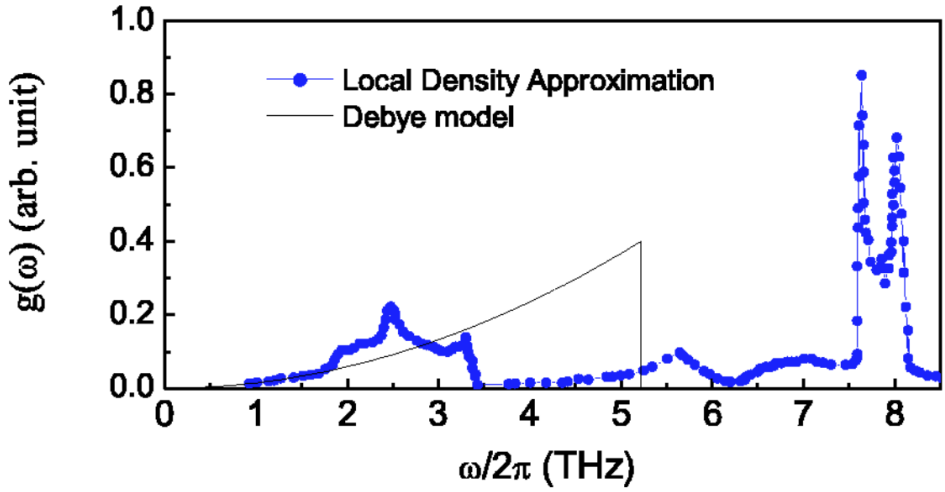

Figure 1.5: PDOS of GaAs. DFT and Debye model are in blue circles and thin black curve, respectively.

Chapter 2

Introduction to PDF and HERIX techniques

2.1 The nanostructure problem

Static structure, or how the atoms are arranged in materials, is among the central concepts in the physical sciences. Knowing the precise structure of the material system of interest dramatically facilitates the understanding of the properties and helps establish the structure-performance correlation. Experimentally, the traditional way to determine the structure of materials is through scattering techniques where x-rays, neutrons or electrons are commonly applied as scatterers. For crystalline materials, the scattering is in the form of sharp "Bragg peaks" whose position can be determined from the famous Bragg law [Bragg and Bragg, 1913; Bragg, 1914]

$$n\lambda = 2d\sin\theta \tag{2.1}$$

where λ is the x-ray wavelength and θ is the Bragg diffraction angle. A schematic of the scattering geometry that results in the Bragg equation is sketched in Fig. 2.1. Bragg's law lays the foundation for crystallography. In the past century as many as 29 nobel prize awards have been given for scientific achievements directly related to, or involving the use of, crystallographic methods and

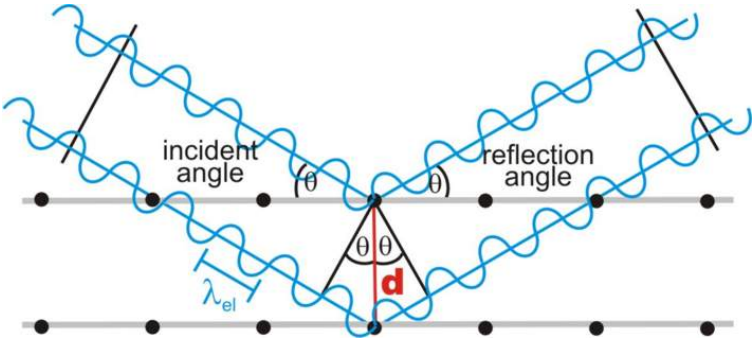

Figure 2.1: A schematic of Bragg scattering. The incident waves impinge on atomic planes separated by a distance of d with an incident angle θ. The path difference of waves shining on adjacent planes are therefore $2d\sin\theta$. The figure is adapted from http://www.microscopy.ethz.ch/bragg.htm.

techniques (http://www.iucr.org/people/nobel-prize). The structures of materials are routinely determined based on Bragg intensities observed in the scattering pattern. However, the Bragg peaks become broadened, or do not even exist, when the crystallite sizes are getting smaller. Eventually at the nanometer scale, the Bragg peaks are significantly broadened and overlapped, leaving little amount of useful information for a complete structural solution and giving rise to so-called *"nanostructure problem"* [Billinge and Levin, 2007]. As an example, the lab x-ray diffraction patterns of bulk zirconium phosphate (ZrP) and its nanocrystalline counterparts are shown in the left panel of Fig. 2.2. These data were collected using a copper K_α radiation. It is obvious that in contrast to well defined Bragg peaks observed in bulk ZrP sample, nanoparticulate samples exhibit few fairly broadened peaks from which only structural information on layer spacings can be deduced (these materials have well-known layered structures [Clearfield and Smith, 1969]). No intra-layer structural details can be obtained. In contrast, as we will show in this thesis, by applying the atomic pair distribution function (PDF) technique, a structural solution is possible. In the right panel of Fig. 2.2, the corresponding PDFs are plotted. It is readily seen that the PDF peaks of nanoparticulate samples are sharp and provide rich structural information for structure determination.

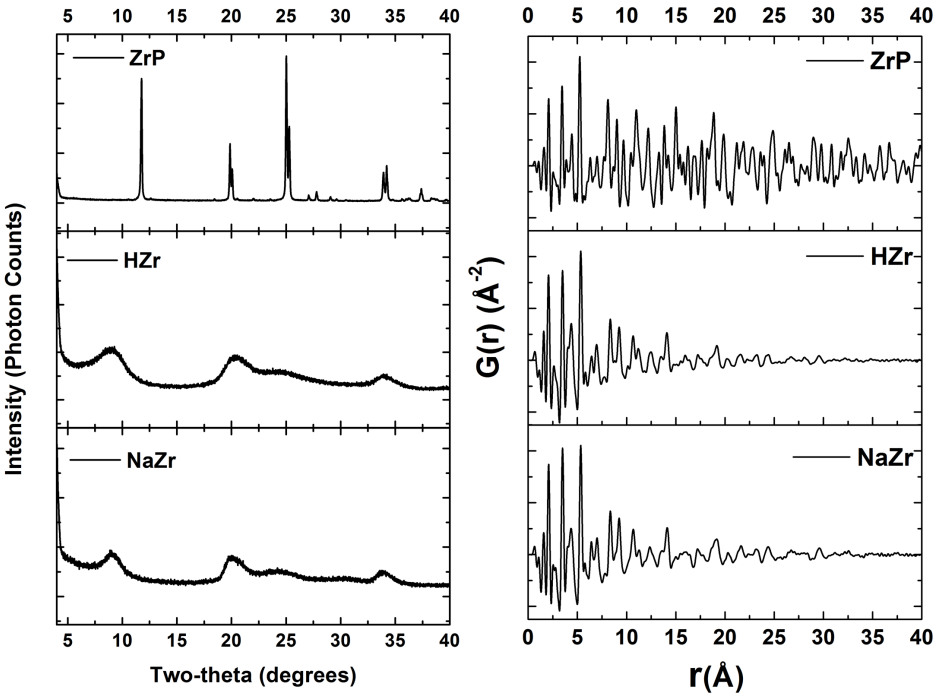

Figure 2.2: (left) Lab x-ray diffraction patterns of zirconium phosphate with the bulk sample shown in top panel followed by the nanoparticles below. (right) The corresponding atomic pair distribution functions of bulk and nanocrystalline samples measured at National Synchrotron Light Source (NSLS) at Brookhaven National Laboratory (BNL).

2.2 Atomic pair distribution function

The tool of choice to attack the *"nanostructure problem"* is to use PDF analysis of neutron or synchrotron x-ray total scattering data. These are powerful techniques for reconstructing three-dimensional ($3D$) atomic structure of nanoparticles with atomic level precision, even when the structural correlations extend only on the scale of a few nanometers. In a total scattering experiment both Bragg intensity and diffuse scattering signals are recorded simultaneously and treated on an equal basis. The resulting experimental curve, a PDF, contains both local structure and intermediate to long-range order structural information [Egami and Billinge, 2012]. In a typical x-ray total scattering experiment, powder samples are enclosed in a kapton capillary and are measured at some temperature. The rapid acquisition pair distribution function (RaPDF) method [Chupas *et al.*, 2003] using a large area 2D fast readout image plate detector is often applied. The raw 2D data are then azimuthally integrated and converted to 1D intensity versus 2θ. There are programs available for doing this processing stept, such as FIT2D [Hammersley *et al.*, 1996] or xPDFsuite [Yang *et al.*, 2015]. The empty capillary is measured so that the scattering from the container may be subtracted. The data are corrected for experimental aberrations [Egami and Billinge, 2012; Billinge and Farrow, 2013] and normalized to the total scattering cross-section, the square of the average atomic scattering factor, to produce $S(Q)$ and then Fourier transformed to obtain the reduced PDF, $G(r)$, according to

$$G_{obs}(r) = 2/\pi \int_{Q_{\min}}^{Q_{\max}} Q[S(Q) - 1] \sin Qr \, \mathrm{d}Q. \tag{2.2}$$

Here Q is the magnitude of the momentum transfer on scattering and $S(Q)$ is the properly corrected and normalized powder diffraction intensity measured from $Q_{\min}$ to $Q_{\max}$ [Egami and Billinge, 2012].There are also software programs for this such as PDFgetX3 [Juhas *et al.*, 2013] and xPDFsuite [Yang *et al.*, 2015]. The PDF, $G(r)$, yields the probability of finding a pair of atoms separated by a distance r.

On the other hand, the PDF can be simulated from a known structure model through

$$G_{calc}(r) = \frac{1}{Nr\langle f\rangle^2}\sum_{i\neq j} f_i f_j \frac{1}{\sqrt{2\pi}\sigma_{ij}} \exp\left[-\frac{(r-r_{ij})^2}{2\sigma_{ij}^2}\right] - 4\pi r\rho_0 \tag{2.3}$$

where ρ_0 is the average atom-pair density, $f_{i,j}$ describe the scattering abilities of atoms of probing waves and σ_{ij} accounts for finite peak width resulting from atomic vibrations and static disorder.

With experimental PDF data and structure models, quantitative structural information can be obtained by fitting calculated PDFs to measured ones. The starting point is a model of the structure which is defined with a set of model parameters p_i. The fitting process then amount to varying the parameters in such a way as to minimize a goodness of fit residuum, R_w.

$$R_w(p_1, p_2, ...) = \sqrt{\frac{\sum_n [G_{obs}(r_n - G_{calc}(r_n))]^2}{\sum_n G_{obs}^2(r_n)}} \tag{2.4}$$

A least-squares refinement of p_i is routinely carried out to minimize R_w. Several PDF modeling softwares are available free of charge, including PDFgui [Farrow *et al.*, 2007], DiffPy-CMI [Juhs *et al.*, 2015] and DISCUS [Neder and Proffen, 2008] and RMCprofile [Tucker *et al.*, 2007].

A typical procedure for PDF determination from experiment to modeling is displayed in the left panel of Fig. 2.3 [Billinge and Kanatzidis, 2004]. In this example, experimenters bring their samples to a synchrotron facility and conduct the PDF experiment. The 2D detector records the diffraction pattern. After proper normalization and data correction, the reduced structure factor $F(Q)$, which is defined as $Q[S(Q) - 1]$, and $G(r)$ are thus obtained. The x-ray total scattering experiments in Billinge's group were previously carried out at beamline X17A, at NSLS, Brookhaven National Laboratory whose experimental setups are shown at the right panel of Fig. 2.3. During the PDF experiment, the incident high energy x-ray with a typical wavelength 0.1839 Å comes from the right to the left and shines on the powder samples encapsulated in a kapton capillary tube with an outer diameter of 1 mm. The capillary geometry is used to achieve a sample powder average. A large charge coupled device (CCD) camera is applied to collect the x-ray diffraction pattern. The beamline end-station is also equipped with cryoguns so that the temperature can be tuned from base temperature 4 K to 500 K. In an experiment, users type in commands in the computer station

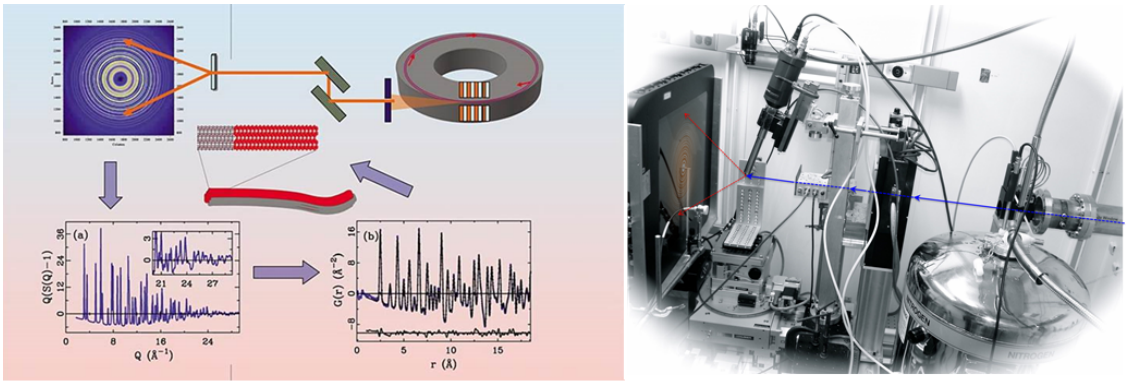

Figure 2.3: (left) An illustration of PDF technique from experiment through raw data reduction to structural models. Reproduced with permission from [Egami and Billinge, 2012] (right) X17A beamline setup at NSLS, Brookhaven National Lab, courtesy of Dr. Milinda Abeykoon.

outside the hutch to control the experiment. After the shutdown of NSLS I in September 2014, most PDF experiments in the group are carried out at at the x-ray powder diffraction (XPD) beamline at the new NSLS II facility at Brookhaven National Laboratory.

2.2.1 Extracting structural information from the PDF

In a single PDF curve rich structural information is encoded. Among many others, three pieces of information are readily available. One may obtain information on bond-lengthes by looking at peak position; coordination numbers (CNs) by integrating the PDF peak; bond length distributions by extracting PDF peak width which could be obtained by either fitting a peak such as a Gaussian function or carrying out a PDF model fit in a given r-range using programs such as PDFgui [Farrow *et al.*, 2007] or DiffPy-CMI [Juhs *et al.*, 2015].

2.2.2 PDF modeling approaches of low-dimensional materials

As displayed in right panel of Fig. 2.2, the PDF of bulk crystalline ZrP exhibits strong atomic correlation to 40 Å where we cut off the plot, but the PDF signals in nanoparticulate samples die out at ∼35 Å. If we don't consider the finite instrument resolution, the PDF signal in a bulk material

should oscillate to an infinite large r because one can always find atomic pairs with infinite large separation. In contrast, in finite sized object such as low-dimensional materials, the PDF intensity falls with r, which encodes important information on particle shape and size.

To calculate the PDF of a bulk crystalline material in real space, one uses

$$G_r = 4\pi r \left[\rho_{bulk}(r) - \rho_0\right] \tag{2.5}$$

where the pair density function $\rho_{bulk}(r)$ is calculated from a model with periodic boundary conditions [Proffen and Billinge, 1999], or from a box of atoms that is much larger in extent than the range of r of interest [McGreevy and Pusztai, 1988], using Equation 2.3.

There are in general two approaches in modelling the low-dimensional materials. The first approach is through a "characteristic function" to account for the finite size effect from nanosystems. It is the autocorrelation, or self convolution, of the shape function of the sample. The shape function defines the shape of the particle. It has the property that it has value unity inside the (average) nanoparticle and value zero outside. The PDF of the nanoparticle can be calculated theoretically from atomic models by multiplying the bulk $G_{bulk}(r)$ by the characteristic function, $\gamma(r)$ [Gilbert, 2008; Farrow and Billinge, 2009; Masadeh *et al.*, 2007; Yang *et al.*, 2013; Shi *et al.*, 2013; Farrow *et al.*, 2014],

$$G_{nano}(r) = \gamma(r) G_{bulk}(r). \tag{2.6}$$

Here $G_{bulk}(r)$ is a PDF calculated using periodic boundary conditions. One may analytically write down the characteristic functions for simple geometries such as sphere or cylinder. For example equations for calculating a spherical particle is written as follows:

$$\gamma(r) = \left[1 - \frac{3r}{2D} + \frac{1}{2}(\frac{r}{D})^3\right] \theta(D - r), \tag{2.7}$$

where,

$$\theta(D - r) = \begin{cases} 0 & d < r \\ 1 & d > r. \end{cases} \tag{2.8}$$

It actually calculates the ratio of common volume of two spheres relative to the volume of a single sphere where the two spheres each with a diameter D and both centers are separated by a distance

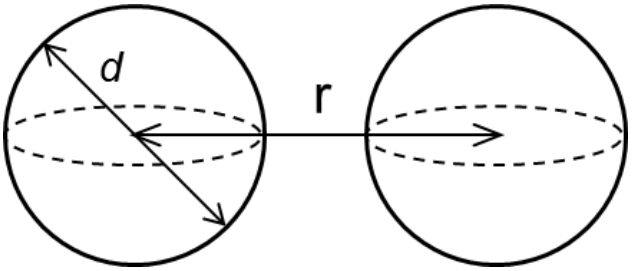

Figure 2.4: The schematic for calculating the spherical shape function.

r. As sketched in Fig. 2.4, if two spheres are more than D apart, there is no overlap between them. On the other hand, if both are completely overlapped, their common volume would be equal to the volume of a single sphere. Therefore the characteristic function gives a value between 0 and 1. It is worth mentioning that the PDFgui program [Farrow *et al.*, 2007] adopts the spherical shape function approach to model nanoparticle. Other shapes may be modeled by using the Diffpy-CMI software package [Juhs *et al.*, 2015] Shown in Fig. 2.5 is one such example from modeling spherical CeO_2 nanocrystals. It is clear that a spherical shape function in current example attenuates the PDF intensity quite well. More analytical shape functions for simple geometries are laid out in Kodama *et al*. [Kodama *et al.*, 2006] and in [Thorpe *et al.*, 2002] and have been implemented in DiffPy-CMI [Juhs *et al.*, 2015].

The characteristic function approach deals best with simple geometries and is only valid in situations where the particle shape and the underlying structure are decoupled [Gilbert, 2008]. However, in reality the low-dimensional materials may have arbitrary shapes or contain defects where the shape function approach fails. As an alternative, we can calculate PDF of a nanosystem via the Debye scattering equation [Debye, 1915] where the structure function $F(Q)$ is calculated through a Debye sum

$$F(Q) = \frac{1}{N\left\langle f(Q)\right\rangle^2}\sum_{i,j} f_i(Q)f_j(Q)\frac{\sin Qr_{ij}}{r_{ij}}\exp\left[-\frac{1}{2}\sigma_{ij}^2Q^2\right] \tag{2.9}$$

As usual, according to Equation 2.2, Fourier transforming $F(Q)$ one obtains $G(r)$. If the atomic coordinate of each atom is known beforehand, it is straightforward to use the Debye equation to

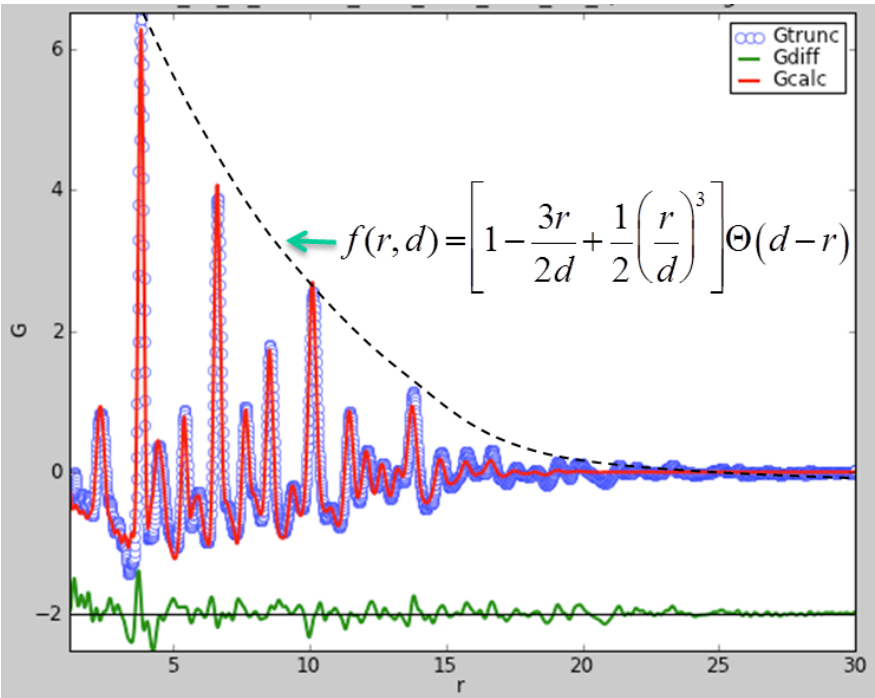

Figure 2.5: Modeling spherical CeO_2 nanocrystal using PDFgui. The blue circles and red solid lines correspond to respectively, measured and calculated PDFs, respectively. Green curve offset below is the difference curve.

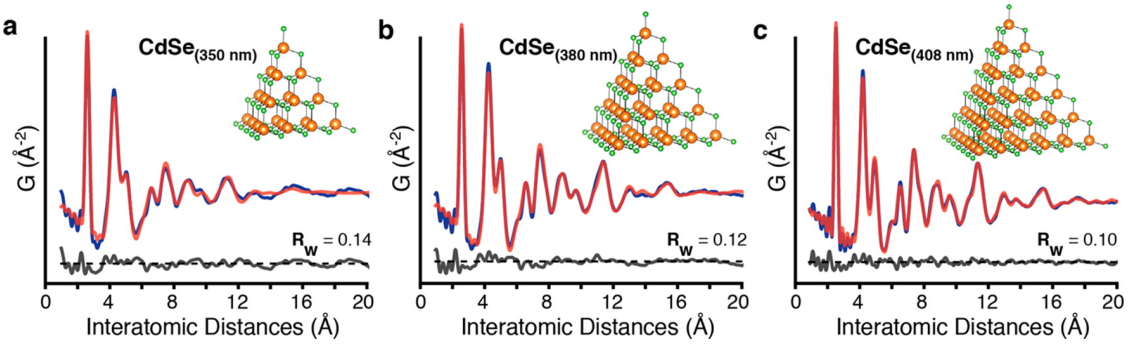

Figure 2.6: Modeling of pyramidal CdSe clusters with DebyePDFcalculator.

simulate the PDF. For example, in the Diffpy-CMI program, using DebyePDFcalculator, one may simulate the PDF for particles with arbitrary morphology. One such example to calculate the PDF of "magic size" CdSe quantum dots [Beecher *et al.*, 2014] is shown in Fig. 2.6. The quantum dots are tetrahedral in shape and the lattice planes line up with the particle edges. We see a good agreement between calculated and measured PDFs. The simulations of the PDF using the Debye equation have been routinely applied to a wide variety of nanosystems [Farrow *et al.*, 2013; Du *et al.*, 2012; Zhu *et al.*, 2014; Beecher *et al.*, 2014; Cernuto *et al.*, 2011; Guagliardi *et al.*, 2010; Cervellino *et al.*, 2010; Cademartiri *et al.*, 2006]. In this thesis, the same method has been extensively applied to study the local structures of emerging two-dimensional nanomaterials. It should be mentioned that the computation time using DebyePDFcalculator increases dramatically with number of atoms in the samples. In reality one needs to make a balanced decision between these two modeling approaches.

2.3 High energy resolution inelastic x-ray scattering (HERIX)

2.3.1 A brief introduction to phonons

When probing sources such as x-ray or neutrons interact with materials, there are a series of possible excitations in materials which is schematically shown in Fig. 2.7 based on different excitation energies. The excitations of interest in this chapter are phonons which have energy of the order of

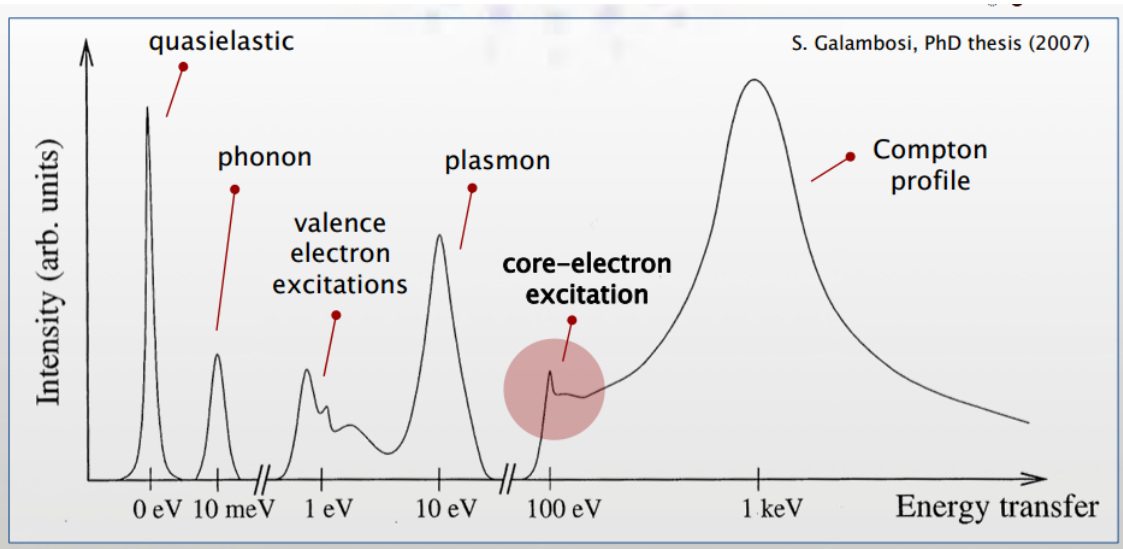

Figure 2.7: A schematic representation of the typical excitations in the materials. The figure is adapted from Galambosi PhD thesis which may be found at https://helda.helsinki.fi/bitstream/handle/10138/23292/electron.pdf?sequence=1.

meV.

The concept of phonons and their properties were firstly introduced by Nobel laureate Peter Debye in 1912 [Debye, 1912], which are defined as quanta of vibrational energy within a crystal structure. Phonons can be viewed as "quasi-particles" with a wave vector $\vec{q}$ and angular frequency ω. The energy of a phonon mode is $\hbar\omega$. It is possible to have multiple corresponding energy levels for a phonon with momentum $\vec{q}$. These branches are the different vibrational polarizations a phonon mode may possess. As shown in Fig. 2.8, each momentum point has two possible corresponding energies. Polarizations could be either longitudinal, where atoms oscillates in the direction of wave propagation, or transverse, where atoms oscillate perpendicular to the direction of propagation direction. The maximum number of phonon branches for a bulk model is the number of atoms per unit cell multiplied by the number of degrees of freedom the atoms have (normally three) where usually three is subtracted from the product if the shift of all atoms along x, y, z directions is not considered. These phonon branches are divided into two categories: acoustic and optical. Acoustic

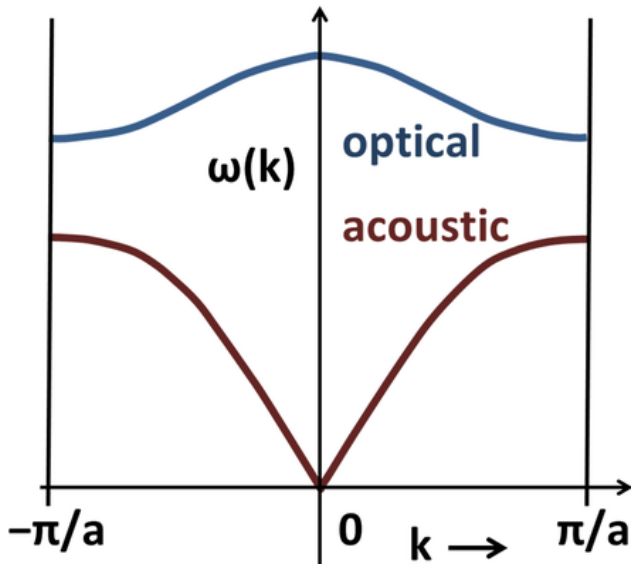

Figure 2.8: An example of phonon dispersion curve: each momentum $\vec{q}$ has two corresponding possible energies, which are denoted by optical and acoustic branches. respectively.

branches are defined by the relation $\omega(\vec{q} = 0) = 0$ with atoms vibrating in phase and optical branches are defined by the relation $\omega(\vec{q} = 0) \neq 0$ with atoms moving out of phase.

Different experimental and theoretical tools to measure and simulate phonons in materials are summarized in Chapter 1. For single crystals, phonon dispersion can be measured by inelastic x-ray/neutron scattering techniques where it shows the energy of phonon modes along high symmetry directions (left panel of Fig. 2.9 [Widulle *et al.*, 1999]). For a polycrystalline sample, phonon information along certain direction can not be deduced. Instead a powder averaged phonon density of states (PDOS) is of particular interest (right panel of Fig. 2.9) which describes all phonon modes carried with certain energies. PDOS is important in studying lattice dynamics of a material system. Once the PDOS is preciously known, a wide variety of thermodynamic quantities such as Gibbs free energy, vibrational entropy, and thermal factors, can be calculated within the harmonic approximation through well-established partition equations as listed below [Chaplot *et al.*, 2010; Dove, 2003; Dove, 1993].

$$E = \frac{1}{2} r \int_0^\infty g(\omega)(\hbar\omega) \coth\left(\frac{\hbar\omega}{2k_B T}\right) d\omega \tag{2.10}$$

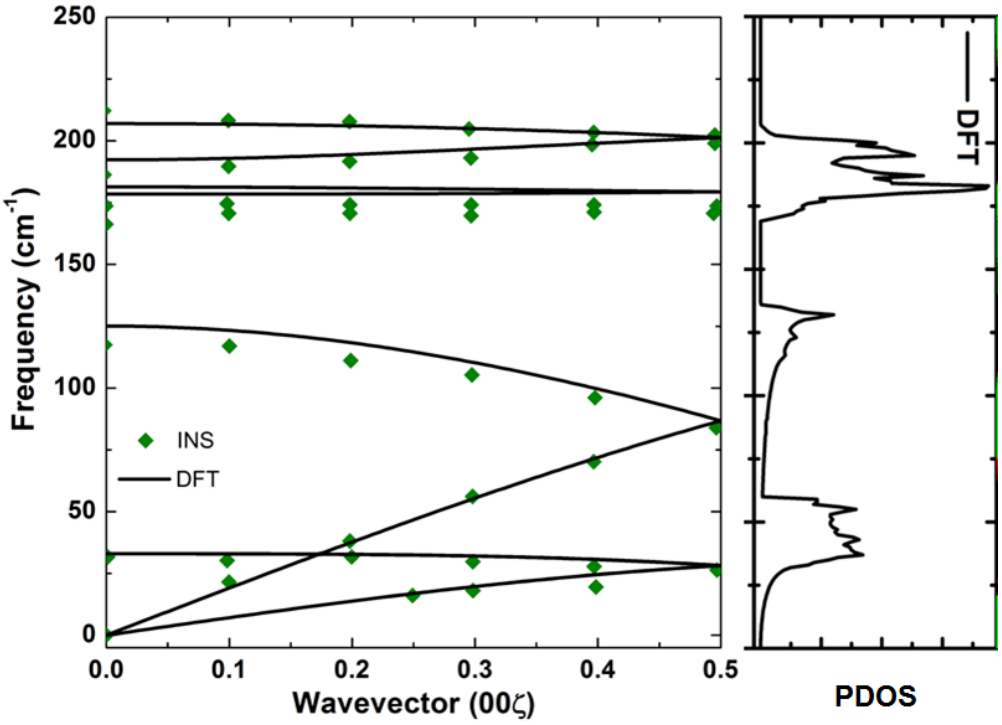

Figure 2.9: (left) The phonon dispersion curve along Γ-A direction for CdSe with wurtzite structure (right) Corresponding phonon density of states calculated by DFT.

$$F = rk_BT\int_0^\infty g(\omega)\ln\left[2\sinh(\frac{\hbar\omega}{2k_BT})\right]d\omega \tag{2.11}$$

$$C = rk_B\int_0^\infty g(\omega)\left(\frac{\hbar\omega}{k_BT}\right)^2\frac{\exp(\frac{\hbar\omega}{k_BT})}{\left[\exp(\frac{\hbar\omega}{k_BT})-1\right]^2}d\omega \tag{2.12}$$

$$S = rk_B\int_0^\infty g(\omega)\left(\frac{\hbar\omega}{2k_BT}\right)\left(\left[\coth(\frac{\hbar\omega}{2k_BT})-1\right]-\ln\left[1-\exp(\frac{\hbar\omega}{2k_BT})\right]\right)d\omega \tag{2.13}$$

$$\left\langle u_i^2\right\rangle = \frac{\hbar}{2M}\int\frac{1}{\omega}\coth\left(\frac{\hbar\omega}{2k_BT}\right)g(\omega)d\omega \tag{2.14}$$

where $g(\omega)$ is the PDOS, $\hbar$ is the Dirac constant, r is total freedoms of atoms in a unit cell and k_B Boltzmann constant; E, F, S, C and $\left\langle u_i^2\right\rangle$ correspond to respectively, internal energy, Gibbs free energy, vibrational entropy, specific heat and atomic displacement parameters.

2.3.2 Introduction to HERIX

Inelastic neutron scattering (INS) is often the tool of choice for probing phonons in materials [Chaplot *et al.*, 2010; Dove, 2003; Dove, 1993; Widulle *et al.*, 1999] since the energy of thermal neutrons is comparable to the phonon excitation/annihilation energy. In addition, the momentum of neutrons is large enough to measure phonons across several Brillouin zones in reciprocal space to be representative of the sample at different length scales. In contrast, studying phonons or collective motions of atoms using x-rays was once considered to be an "impossible" task since the ratio of energy resolution (meV) and incident x-ray energy (tens of keV) is in the order of 10^{-7}. Making instruments with this energy resolution is a daunting task [Ashcroft and Mermin, 1976].

However, inelastic x-ray scattering with meV resolution was made possible due to the high photon fluxes available from third generation synchrotron x-ray sources, extremely high quality silicon crystals as monochromators and analyzers and the creative extreme backscattering geometry setup [Chaplot *et al.*, 2010]. Currently HERIX beamlines are operational at the European Synchrotron Research Facility at Grenoble, France, the Advanced Photon Source at Argonne National Laboratory in United States and Spring-8 in Japan with an IXS beamline at Brookhaven National Laboratory in commissioning phase.

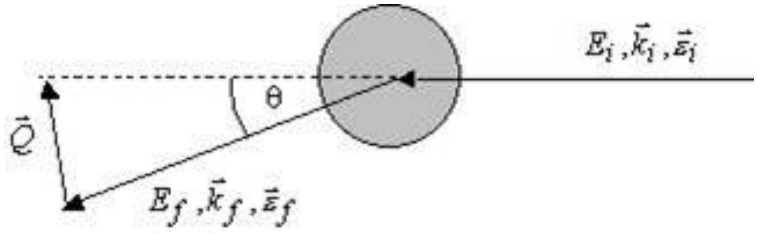

Figure 2.10: A schematic of inelastic x-ray scattering.

The scattering diagram of inelastic x-ray scattering is shown in Fig. 2.10. The incident x-ray carries energy and momentum, E_i and $\vec{k_i}$. After it interacts with the sample, the outgoing x-ray has a different energy, E_f and momentum $\vec{k_f}$. The energy transfer E and momentum transfer $\vec{Q}$ are recorded based on Equations 2.15 and 2.16.

$$E = E_i - E_f \tag{2.15}$$

$$\vec{Q} = \vec{k_i} - \vec{k_f} \tag{2.16}$$

The IXS scattering cross section $\frac{\partial^2\sigma}{\partial\Omega\partial E}$ describes the fraction of photons scattered inelastically in a solid angle Ω after loss or gain of some energy E. It can be expressed as in Equation 2.17.

$$\frac{\partial^2\sigma}{\partial\Omega\partial E} = r_0^2(\vec{\varepsilon_i}\cdot\vec{\varepsilon_f})^2\frac{k_i}{k_f}\left|f(Q)\right|^2 S(\vec{Q},E) \tag{2.17}$$

where r_0 is classical electron radius (2.8179×10^{-15} m), and $\vec{\varepsilon_i}$ and $\vec{\varepsilon_f}$ are polarization factors of incident and outgoing x-ray, respectively. From HERIX experiment, one obtains the dynamic structure factor $S(\vec{Q},E)$ which encodes the information on both spatial and temporal correlation of atoms. That is to say, if we know the position of atom A at some beginning time t, we know where to find another atom B at a later time $t+\Delta t$. Within the harmonic approximation, $S(\vec{Q},E)$ for single-phonon scattering has the form [Bosak and Krisch, 2005; Chaplot *et al.*, 2010; Dove, 2003]:

$$S(\vec{Q},E) = \sum_j \left\langle n(E) + \frac{1}{2} \pm \frac{1}{2} \right\rangle (E_j(\vec{q}))^{-1} F_{in}(\vec{Q})\delta(E \pm E_j(\vec{q})) \tag{2.18}$$

where the term in angle brackets is the Bose factor that yields the phonon occupancy at temperature T with plus and minus signs corresponding to phonon creation and annihilation scattering processes,

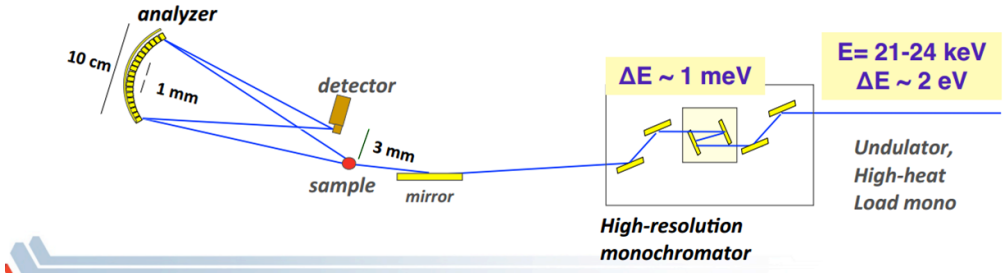

Figure 2.11: Experimental setup of inelastic x-ray scattering at beamline 30 at APS, Argonne National Laboratory.

respectively. $F_{in}(\vec{\boldsymbol{Q}})$ involves the sum over all atoms in the unit cell.

$$F_{in}(\vec{\boldsymbol{Q}}) = \left| \sum_k M_k^{-1/2} f_k(Q) [\vec{\boldsymbol{e_k^j}}(\vec{\boldsymbol{q}}) \cdot \vec{\boldsymbol{Q}}] \exp(i\vec{\boldsymbol{Q}} \cdot \vec{\boldsymbol{r_k}}) \exp(-\omega_k) \right|^2 \tag{2.19}$$

where M_k is the mass of atom k, $f_k(Q)$ is the atomic form factor, $\vec{\boldsymbol{e_k^j}}(\boldsymbol{q})$ corresponds to the eigenvector for phonon mode j of atom k with wavevector $\vec{\boldsymbol{q}}$, $\vec{\boldsymbol{r_k}}$ and $\exp(-\omega_k)$ are position of atom k and Debye-Waller factor, respectively.

2.3.3 HERIX experiment

The experimental setup for HERIX at beamline 30 at APS is shown schematically in Fig. 2.11. It utilizes the triple axis geometry as in inelastic neutron scattering developed by Brockhouse [Brockhouse and Hurst, 1952] where the three axes are the monochromator, sample stage, and spherical crystal analyzer. In the experiment, the momentum transfer is selected by rotating the 9 m long HERIX arm (Fig. 2.12) around the sample position in the horizontal plane. As for picking up different energy transfers, E_f, the analyzer side is fixed while E_i at the monochromator side can be varied freely either by changing the lattice spacing of the monochromator crystal through well controlled temperature changes, typically in the order of mK (such as at ID-28, European Synchrotron Research Facilities) or by changing the reflection angle of the incident x-ray using three pairs of in-line crystals at APS, Argonne National Laboratory.

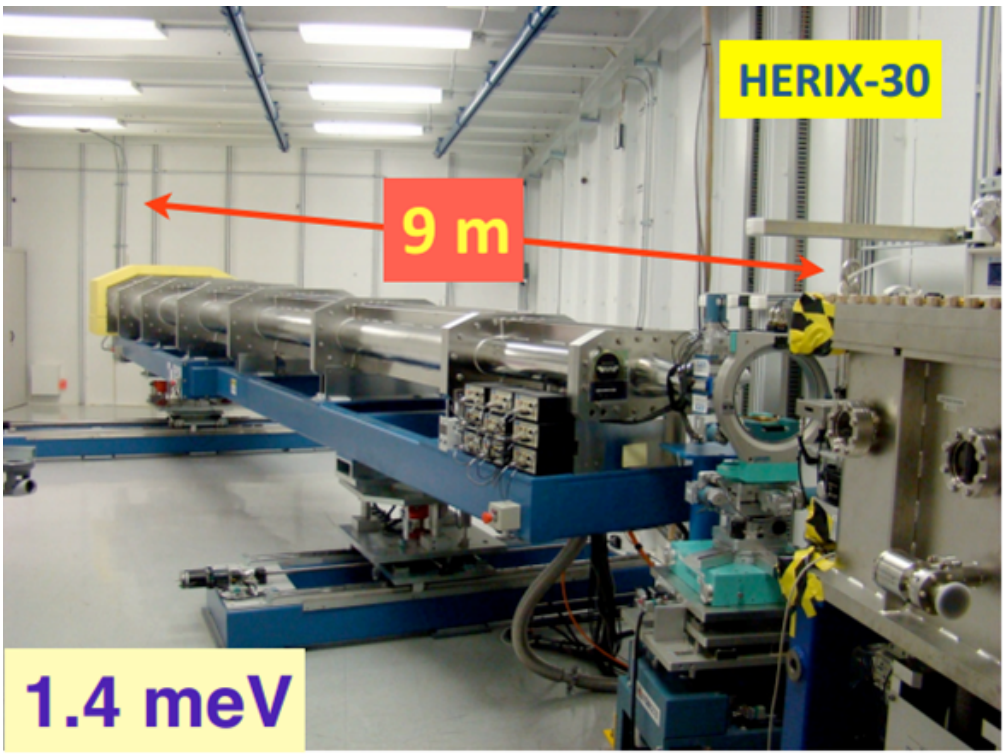

Figure 2.12: HERIX arm at beamline 30 at APS, Argonne National Laboratory.

The meV energy resolution is achieved by using a high order reflection from perfect crystals. The energy band width $\frac{\Delta E}{E}$ is given by

$$\frac{\Delta E}{E} = \frac{d_{hkl}}{\pi \Lambda_{ext}} \tag{2.20}$$

where d_{hkl} and Λ_{ext} are respectively, lattice spacing of (hkl) reflection order and primary distinction length [Zachariasen, 2004]. Λ_{ext} increases with increasing reflection order. In order to achieve a high resolving power, it is therefore preferable to use high-order Bragg reflections and to have highly perfect crystals. The stringent requirement narrows the choice of crystals to silicon.

We reproduce here the steps to experimentally measure the IXS spectrum from a powder sample to obtain the phonon density of states, (PDOS). The first step is to choose the highest possible Q, or range of Q-values, to enhance the signal since the inelastic scattering intensity is proportional to the Q^2. At the HERIX beamline at APS the highest Q for the analyzer is 72 nm^{-1}, for analyzer #9, and the measurable Q for analyzer #8 to analyzer #1 decreases gradually by 1.96 nm^{-1} per analyzer. Care must be taken to choose the proper Q-values or sampling for each analyzer to avoid Bragg peaks. Next, a Poly(methyl methacrylate) or PMMA sample is measured at room temperature at 10 nm^{-1} to determine the resolution function and efficiency of each analyzer. The analyzer efficiency is considered later when summing up the IXS signal from each individual analyzer. For the PDOS experiment, the samples are in powder form to ensure an orientational average. An important aspect of the experiment is to find the optimum thickness for the sample to ensure approximately one absorption length, which can be estimated using the calculator at http://11bm.xray.aps.anl.gov/absorb/absorb.php. For nanoparticle samples containing ligands, it is impossible to have an accurate value for the packing density. Therefore in reality a "trial and error" approach is adopted where samples with a spectrum of thicknesses were prepared beforehand, or at the beamline, allowing us to pick up the one with the "best" μt. However, this is time-consuming and requires large quantities of sample which is not often possible to prepare. Alternatively, we find a work-around that would help easily find the optimum thickness for the IXS experiment. In our method, the powder samples are encapsulated in a kapton capillary and

prepared thick. Since the tube is aligned horizontally and loosely packed, the front end of the sample results in a series of thicknesses. Taking advantage of μm beam size, by scanning the sample position horizontally and vertically, one would always be able to find a μt that is very close to 1. However, we also noticed that this approach is only valid for room temperature measurement or for samples in a tube. In contrast for temperature-dependent experiments where a copper washer is used instead this approach does not work.

2.3.4 Procedure to obtain phonon density of states

The experimental IXS scattering signal has contributions from various sources including elastic scattering, one-phonon scattering, multiphonon scattering and background. To obtain the phonon density of states, one needs first to deconvolute the resolution function and then carefully subtract the background, central elastic peak and multiphonon scattering. The resulting signal is only from single phonon scattering. One then obtains the PDOS by multiplying the signal with a phonon occupancy factor $E\,[1-\exp(-E/kT)]$ where k, E corresponds to the Boltzmann constant and phonon energy, respectively.

Bosak *et al.*, proposed a convenient way to extract PDOS from HERIX for polycrystalline materials [Bosak and Krisch, 2005] where the multi-phonon contribution is eliminated simultaneously with the deconvolution of instrumental function. Here I will briefly explain the steps one by one using the data on smallest CdSe quantum dot ($CdSe_{350nm}$) measured recently at the HERIX beamline. Fig. 2.13(a) shows the raw IXS data collected by seven crystal analyzers as a function of energy transfer from -10 meV to 40 meV. Due to slight misalignments of the analyzer crystals with respect to each other, the strong elastic peak is not aligned at the nominal 0 meV for each analyzer. To correct for this, a Pseudo-Voigt (PV) function was fitted to determine the peak position and shift it to zero point. The thus-corrected IXS data are shown in Fig. 2.13(b). Subsequently as shown by black curve in Fig. 2.13(c) the scattering signals from each analyzer are summed up where the intensity of each analyzer was divided by individual analyzer efficiency. The top portion of the center elastic peak was fitted with a PV function to create a resolution function (green curve in

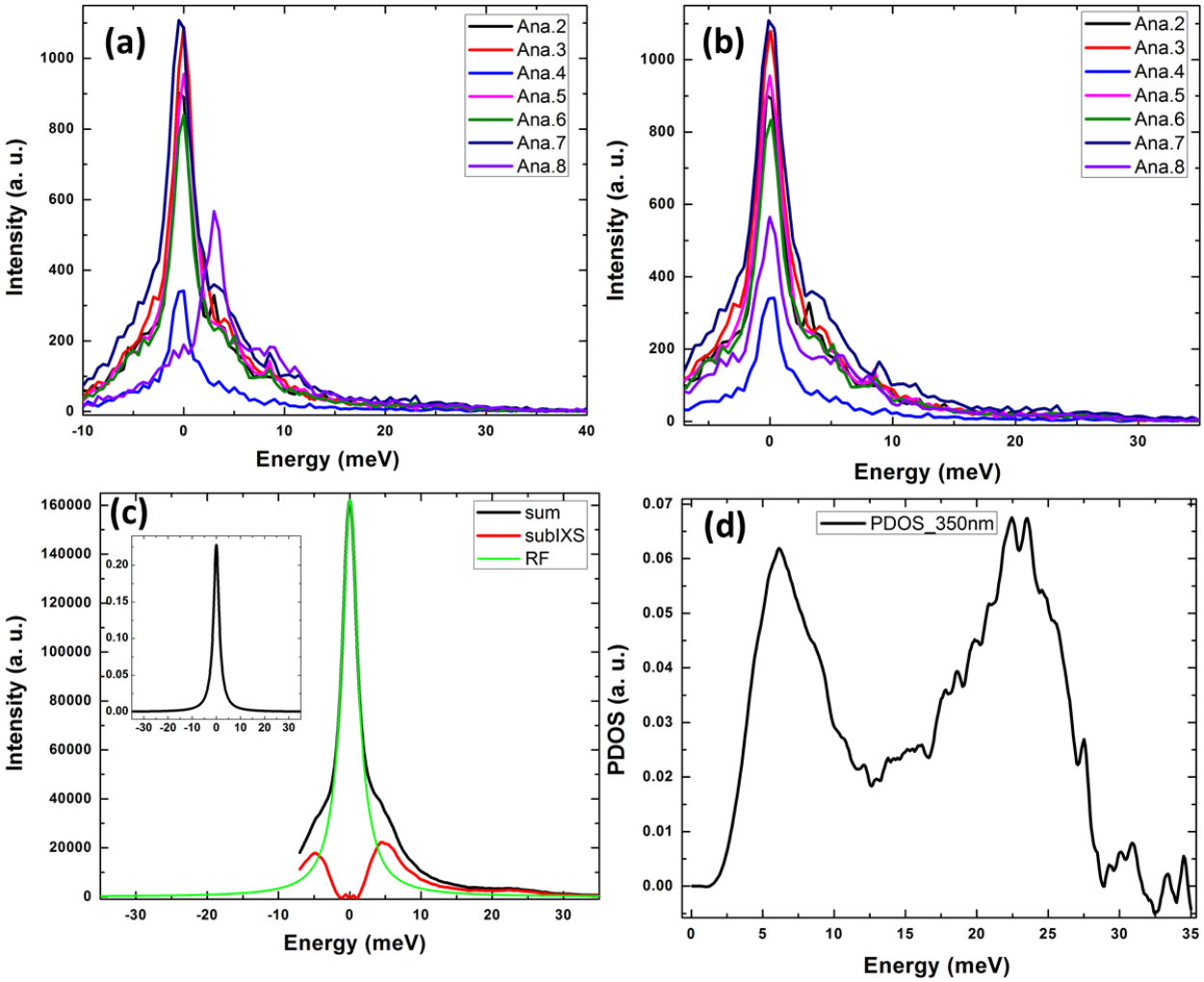

Figure 2.13: (a)Raw scattering signals from individual analyzers. The elastic peaks are not at zero positions due to energy drift. (b) Energy drift corrected IXS spectrum for each analyzer. (c) Black: the summed IXS curve from all analyzers corrected by analyzer efficiency. Green: the resolution function created to subtract central elastic line. Red: inelastic x-ray scattering signal. Inset: the normalized resolution function. (d) The resulting PDOS for $CdSe_{350nm}$ sample.

Fig. 2.13(c)), which was used to subtract central elastic peak. The elastic-peak subtracted IXS spectrum is shown in red in Fig. 2.13(c) whereas the normalized resolution function, $P(E)$ is shown in the inset of Fig. 2.13(c).

To extract the PDOS we follow the recipe proposed by Bosak *et al.*. Through Equations 2.21 and 2.22, one may obtain a scaling factor I_0 and Lamb-Mössbauer factor f_{LM}.

$$\int I(E)dE = I_0(1 - f_{LM}) \tag{2.21}$$

$$\int I(E)EdE = I_0E_R. \tag{2.22}$$

The next step is to deconvolute the resolution function and subtract multiphonon scattering at the same time. To this end, the Fourier transform of $P(E)$ and $I(E)$ are introduced, namely, $Q(\tau)$ and $J_0(\tau)$, respectively, as in Equations 2.23 and 2.24,

$$Q(\tau) = \int dE \exp(iE\tau)P(E) \tag{2.23}$$

$$J_0(\tau) = \int dE \exp(iE\tau)I(E). \tag{2.24}$$

A numerical parameter P_{if} is defined as the degree of deconvolution so that $Q_0(\tau) = (Q(\tau) + P_{if})/(1+P_{if})$. After dividing out the resolution function in Fourier space, the $M(\tau)$ in Equation 2.25 corresponds to the Fourier transform of the single-phonon scattering term,

$$M(\tau) = \ln\left(1 + \frac{\int dE \exp(iE\tau)I(E)}{I_0 f_{LM} Q_0(\tau)}\right). \tag{2.25}$$

An inverse Fourier transform of $M(\tau)$ is then taken and multiplied by the phonon occupancy factor, (Equation 2.26), resulting in the PDOS, $g(E)$, according to

$$g(E) = \frac{E}{E_R}[1 - \exp(-E/kT)] \int \frac{d\tau}{2\pi} \exp(-iE\tau)M(\tau). \tag{2.26}$$

The PDOS for the smallest CdSe quantum dot from our experiment, $CdSe_{350nm}$ (see Chapter 6), obtained following this procedure, is shown in Fig. 2.13(d).

Chapter 3

Local structure of emerging two-dimensional nanocrystalline Ti_3C_2 and Nb_4C_3 MXenes

This chapter is based on two published papers [Shi *et al.*, 2014; Ghidiu *et al.*, 2014].

3.1 Introduction

MXenes are a recently discovered large family of two-dimensional (2D) early transition metal carbides and/or nitrides that are extremely promising for applications in electronic device materials, sensors, conductive reinforcement additives to polymers, catalysis, and electrochemical energy storage materials [Naguib *et al.*, 2014; Naguib *et al.*, 2012a; Come *et al.*, 2012; Lukatskaya *et al.*, 2013]. They are produced by selective etching of metals, such as aluminum, from MAX phases [Naguib *et al.*, 2011; Naguib *et al.*, 2012b; Naguib *et al.*, 2014], which are ternary carbides and carbonitrides with a general composition of $M_{n+1}AX_n$, where M is an early transition metal, A is mainly a group IIIA or IVA (i.e. groups 13 or 14) element, X is C and/or N, and $n = 1$, 2, or 3. The A layers can be selectively etched by chemical means without disrupting the

M-X bonds [Naguib *et al.*, 2014] resulting in weakly bonded $M_{n+1}X_n$ layers that may be readily separated by sonication resulting in novel 2D electronic materials. These new materials have been called *MXenes*, to emphasize the loss of the A element from the MAX parent phase and to highlight their 2D nature, similar to graphene. The structures of the MAX phases are known but it has proven difficult to solve the structure of the MXenes because they form as nanomaterials [Naguib *et al.*, 2012b], which are not amenable to traditional crystallography [Billinge and Levin, 2007]. Although the c lattice parameter of MXenes can be determined from a low-angle diffraction peak in a conventional X-ray experiment [Mashtalir *et al.*, 2013a; Naguib *et al.*, 2013; Mashtalir *et al.*, 2013b], no experimental determination of the a lattice parameter has been reported, let alone the arrangement of atoms. Here we present the first MXene structures, which were obtained from atomic pair distribution function (PDF) analysis [Egami and Billinge, 2012] of synchrotron X-ray diffraction data. We also present the structural modification when charged species are intercalated between the planes. Knowledge of structure is a crucial early step to understanding and controlling the properties of these promising materials.

For all known MAX phases, the M atoms are arranged based on hexagonal close packing (hcp) with the X atoms are sitting in their octahedral interstices. These $M_{n+1}X_n$ layers are fused with layers of A atoms in a 2D hexagonal structure with the space group $P6_3/mmc$ [Barsoum, 2013]. In the MXene phase, after removal of the A atoms, the close packed layers are stabilized by the attachment of O, OH and/or F atoms. Today the family of MXenes includes Ti_3C_2, Ti_2C, Nb_2C, V_2C, $(Ti_{0.5}, Nb_{0.5})_2C$, $(V_{0.5}, Cr_{0.5})_3C_2$, Ti_3CN and Ta_4C_3 [Naguib *et al.*, 2012b; Naguib *et al.*, 2013]. However, the quantitative structure of even the first produced and most studied, Ti_3C_2 is not known. Density functional theory (DFT) calculations have been used to predict the structures. The early DFT studies [Tang *et al.*, 2012; Enyashin and Ivanovskii, 2012; Xie and Kent, 2013] found two distinct configurations based on two energetically favorable orientations for OH or F in Ti_3C_2 but these have not been tested experimentally and the undisturbed structure of the MX layer is not even established because of the nanocrystalline nature of the product. The PDF method is a powerful probe of nanostructure, yielding quantitative structural information at the

nanoscale [Billinge and Kanatzidis, 2004; Billinge, 2008; Young and Goodwin, 2011]. It uses high energy X-rays or neutrons together with Fourier analysis of the diffraction data resulting in PDFs that yield information about the local arrangement of atoms by fitting with calculated PDFs from quantitative models [Egami and Billinge, 2012]. Here we successfully used it to determine the structures of pristine $Ti_3C_2T_x$ (where T stands for surface terminating species, such as OH, O or F bonded to Ti atoms), potassium hydroxide (KOH) intercalated $Ti_3C_2T_x$ and sodium acetate (NaAc) intercalated $Ti_3C_2T_x$ [Lukatskaya *et al.*, 2013; Mashtalir *et al.*, 2013b]. Additionally, we quantify small changes in the M-layer of the MXene structure on interacalation which may prove important for the electronic properties.

3.2 Experiment and Method

Our collaborators at Drexel University, Majid Beidaghi, Michael Naguib and Olha Mashtalir prepared the pristine and intercalated MXene $Ti_3C_2T_x$ samples for PDF study. Michael Ghidiu, Michael Naguib and Olha Mashatalir synthesized Nb_4C_3 MXene for PDF experiment. They are PhD students from Profs. Gogotsi and Barsoum group.

$Ti_3C_2T_x$ was synthesized by etching Al from Ti_3AlC_2. The Ti_3AlC_2 powders with particles less than 38 μm were treated with 50% aqueous HF solution at room temperature (RT), for 18 h. The resulting suspensions were washed several times using deionized water and separated from any remaining HF by centrifuging until the pH of the liquid reached around 5. The wet sediment was moved to a wide-mouth jar by ethanol and dried in air for 3 to 4 days. The resulting $Ti_3C_2T_x$ was placed into capped glass vials and stored under ambient conditions for further experiments. To intercalate the powders, 0.15 g of $Ti_3C_2T_x$ was suspended in 5 ml of a 30 wt.% aqueous solution of potassium hydroxide or sodium acetate. The mixtures were stirred for 24 h with a magnetic stirrer at RT. Afterwards, the resulting colloidal solutions were filtered and dried in a desiccator under vacuum (< 10 Torr) at RT.

Polycrystalline samples of Nb_4AlC_3 were prepared by *in situ* hot pressing of commercial powders

of Nb, Al and C at 1700 °C for 1 h under 30 MPa. The resulting powders were predominantly single-phase Nb_4AlC_3 as determined by XRD (Fig. 1a). The Nb_4AlC_3 powder ($< 38\ \mu m$ particle size) was etched in 48 % aqueous HF for 96 h at ambient temperature, followed by washing with distilled water until pH ∼5 was reached. The sediment was mixed in ethanol and allowed to dry by evaporation. A rudimentary yield by mass (mass of MXene products divided by starting mass of MAX) was 77 %. For this system it is important to note that this yield does not reflect molar quantities, since neither the nature of the MXene surface terminations nor possible intercalants are precisely known. The number stated above simply indicates that the yields are robust.

Synchrotron X-ray total scattering experiments were conducted at beamline X17A at the National Synchrotron Light Source (NSLS) at Brookhaven National Laboratory. The incident x-ray has an energy of 67.4194 keV (λ=0.1839 Å). The sample-to-detector distance is 204.099 mm. Nickel was also measured as a standard material to calibrate the sample-detector distance and to determine the Q_{damp} and Q_{broad} parameters which are the parameters that correct the PDF envelope function for the instrument resolution effects [Proffen and Billinge, 1999; Farrow *et al.*, 2007]. The refined values of $Q_{damp} = 0.0416$ Å^{-1} and $Q_{broad} = 0.0172$ Å^{-1} are allowed to vary in the subsequent model fits to PDF data. Structural modeling was carried out using the PDFgui [Farrow *et al.*, 2007] and Diffpy-CMI [Juhs *et al.*, 2015] programs.

The reduced structure factor, $F(Q)$, and the experimental PDF of the pristine $Ti_3C_2T_x$ are displayed in Fig. 3.1(a) and (b), respectively. Both $F(Q)$ and PDF exhibit a coexistence of sharp and broad peaks suggesting a mixture of reasonably well ordered and less well ordered structural aspects. This presents a challenge for a crystallographic analysis because there are not well ordered 3D crystals, but also means that by using a suitable method such as PDF a satisfactory quantitative structural model can be obtained.

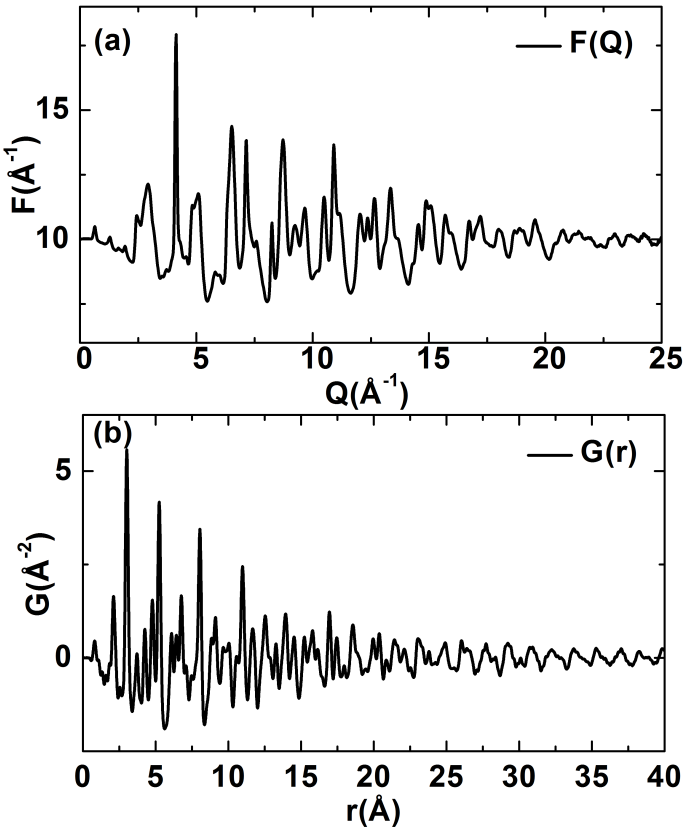

Figure 3.1: (a) The reduced structure factor, $F(Q)$ and (b) the measured PDF of pristine $Ti_3C_2T_x$.

3.3 Results

3.3.1 Ti_3C_2 MXene

The starting point for finding a solution to the structure for $Ti_3C_2T_x$ was to focus on three structural models predicted from a recent density functional theory study from Tang *et. al* [Tang *et al.*, 2012] for bare Ti_3C_2 and surface terminated $Ti_3C_2(OH)_2$ and $Ti_3C_2F_2$. All DFT structures are hexagonal but consist of only one single layer of Ti_3C_2 in the unit cell and are not appropriate for the fully dense unexfoliated MXene materials in our study. In these models, the atoms are sitting in a covalently bonded layer with three Ti and two C atomic layers arranging alternately forming edge-shared Ti_6C octahedra. In bare and fluorine terminated Ti_3C_2 structures, the carbon and titanium atoms are on the special positions: C (1/3, 2/3, z), Ti1 (2/3, 1/3, z) and Ti2(0, 0, 0) with F sitting on (0, 0, z) in $Ti_3C_2F_2$ whereas for the $Ti_3C_2(OH)_2$ structure, the atoms are on non-special positions.

To find how the layers stack we started with the $Ti_3C_2F_2$ structure from Tang *et. al* [Tang *et al.*, 2012] as described above. Mashtalir *et. al* [Mashtalir *et al.*, 2013b] determined the c-axis lattice parameter of pristine $Ti_3C_2T_x$ to be 20.3 Å from the (0002) Bragg peak just below $2\theta = 10$ degrees in an in-house copper K_α measurement. It allows two Ti_3C_2 layers to be fit into one unit cell, but it is not clear how the second layer is inserted with respect to the first. We took a trial and error approach to find it. Simply translating the second layer along the c-axis by $c/2$ resulted in a poor fit to the measured PDF. However, translating by $c/2$ and rotating through 60 degrees resulted in a good fit with an agreement factor $R_w \sim 0.1$ lower than the unrotated layer. In the new layer, the C atoms are sitting at (2/3, 1/3, $0.5 + z$), (1/3, 2/3, $0.5 - z$) and Ti atoms are at (1/3, 2/3, $0.5 + z$), (2/3, 1/3, $0.5 - z$) and (0, 0, 0.5). Once the atomic positions of the Ti_3C_2 sheet were determined, we tried different special positions for terminated F atoms. As suggested based on DFT calculations [Tang *et al.*, 2012] O and/or F atoms may sit at (0, 0, z), (1/3, 2/3, z), or (2/3, 1/3, z). The best agreement to the experimental PDF was obtained for surface functionalities at the (0, 0, z) position with a $R_w \sim 0.05$ lower than the other two cases.

Based on the PDF fits described above we deduce that the pristine $Ti_3C_2T_x$ adopts a space group of $P6_3/mmc$ with a screw axis along the c direction. We therefore carried out a fit using constraints from this space-group. Atomic displacement parameters (ADPs) for C and Ti atoms were constrained to be isotropic in the layer but allowed to be different along the stacking direction. The surface terminated O/F atoms were constrained to have isotropic ADPs. Also a mixture of both hydroxyl and fluoride groups was used with O/F mole ratio determined from an energy dispersive x-ray spectroscopy (EDX) experiment, with the H on the hydroxyl not included in the model because of its weak scattering contribution. EDX data were confirmed by XPS analysis on similar MXene samples, but since the oxygen and fluorine contents somewhat vary from sample to sample, we report EDX results for the samples that were analyzed in this work.

The optimum fit for pristine $Ti_3C_2T_x$ is displayed in Fig. 3.2 (a) and the refined structural parameters are listed in Table 3.1.

Table 3.1: Structure of the pristine and intercalated $Ti_3C_2T_x$. The space-group is $P6_3/mmc$ and the atoms are on the following special positions: Ti1 (2/3, 1/3, z), Ti2 (0, 0, 0), C(1/3, 2/3, z) and O/F (0, 0, z). Numbers in parentheses are the estimated uncertainties on the last reported digit originating from the counting statistics on the data and represent an estimate of precision. O/F mole ratio was determined from an energy dispersive X-ray spectroscopy (EDX) experiment and fixed in the refinements

-	pristine	Na^+	K^+
R_w	0.266	0.197	0.187
a (Å)	3.0505(5)	3.0399(4)	3.0301(4)
c (Å)	19.86(2)	24.55(1)	24.59(1)
O_{frac}	0.458	0.415	0.730
z(C)	0.0597(7)	0.0515(5)	0.0522(4)
z(F)	0.1794(7)	0.1442(3)	0.1432(3)

z(Ti)	0.1212(2)	0.0997(1)	0.1005(1)
U_{iso}(F) (Å^2)	0.056(8)	0.043(4)	0.06(1)
U_{iso}(O) (Å^2)	0.009(2)	0.0010(4)	0.0039(4)
U_{11}(C) (Å^2)	0.0049(4)	0.0070(5)	0.0064(4)
U_{33}(C) (Å^2)	0.005(3)	0.010(3)	0.009(2)
U_{11}(Ti) (Å^2)	0.0029(1)	0.0035(1)	0.0037(1)
U_{33}(Ti) (Å^2)	0.0136(9)	0.0077(5)	0.0092(6)
Q_{broad} (Å^{-1})	0.066(4)	0.052(4)	0.046(3)
Q_{damp} (Å^{-1})	0.072(2)	0.081(2)	0.077(1)
r(Ti(1)-(O/F) (Å)	2.106(8)	2.067(7)	2.040(05)
r(Ti(1)-C)(Å)	2.143(8)	2.117(7)	2.115(6)
r(Ti(2)-C)(Å)	2.123(8)	2.163(7)	2.170(06)

The structure of $Ti_3C_2T_x$ is shown schematically in Fig. 3.2 (d). The fits indicate that the peaks are in the right positions, suggesting that the overall structure is correct. However, the R_w values are high and there is a lot of unfit signal in the residuals suggesting that this structural model is not complete. The likely reason is unaccounted for disorder in the structure, either of the inter-layer stacking or in the form of defects in the layers themselves due to bending, for example. These effects are common in lamellar materials but are not included in the structural model which assumes a perfectly ordered 3D structure, something we know is not present here. There is some inter-layer order, as evidenced by the improved fit of the 60° rotated model for the stacking over the unrotated one, but if the stacking is not perfect as we suspect, and suggested by the enlarged U_{33} parameters for Ti and C in the refinements, this may result in the misfits seen in the residuals curve. Modeling this disorder correctly requires improvements in the modeling software and investigation of it will be pursued in the future.

We now turn to the intercalated $Ti_3C_2T_x$ [Lukatskaya *et al.*, 2013]. The experimental PDFs of the intercalated $Ti_3C_2T_x$ are plotted on top of that from the pristine sample and displayed in

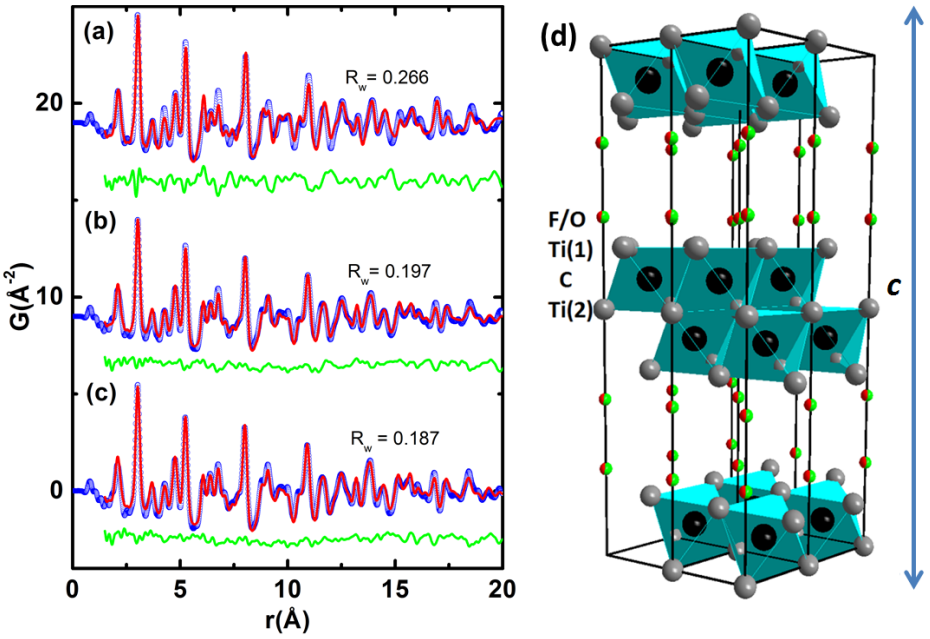

Figure 3.2: The PDF fits of (a) pristine $Ti_3C_2T_x$ (b) Na^+ and (c) K^+ intercalated $Ti_3C_2T_x$: blue circles are the measured data, red curves are the calculated PDFs of the best-fit structural models and the green curves offset below are difference curves. (d) The polyhedral representation of optimized $Ti_3C_2T_x$ structure: Ti, C, O/F atoms are in grey, black, red/green colors. Different Ti atoms are marked with numbers for convenience.

Fig. 3.3. As is evident in the high-r region, the intercalation shifts the PDF peaks to lower-r, which is more obvious for the K^+ insertion. We expect the intercalation to cause a layer expansion, which would cause PDF peaks to shift to higher- rather than lower-r as observed. In fact, the inter-layer spacing in the intercalated compounds does increase, as the change of the refined c-axis lattice parameters in Table 3.1 shows. The observation of a shift of PDF peaks to lower-r in the figure is because the PDF peaks are predominantly intra-layer peaks and the in-plane lattice parameters are contracting on intercalation.

To investigate whether there are any structural changes beyond a simple contraction we apply a simple stretching transformation to the experimental PDFs of the intercalated compounds and compare this with the PDF of the pristine compound. This is done in such a way that $r' = Sr$, where r' is the stretched r-coordinates and S is a stretching factor. A least-squares fit is carried out to find the value of S that gives the best agreement between the intercalated and pristine PDFs. If there is a simple lattice contraction on intercalation, the residual curve between the stretched-intercalated and pristine PDFs will have no features when these two curves are compared. If there are additional structural modifications, these will result in a residual signal in the difference curve even after the stretching transformation. The result is shown in Fig. 3.3(c) and (d). Interestingly, there are small features in the residual at low-r, even as the intermediate and higher-r regions become well accounted for by the stretching transformation. The stretch that fixes the high-r region over-compensates for small differences at low-r suggesting that the near-neighbor bonds are not much perturbed by the intercalation, but there is a larger contraction over a wider range. It is not clear what produces this effect. It might be explained if doped charge from the intercalant ions is trapped in localized defect states rather than in the chemical bonds of the Ti-C network itself. The localized charges produce an electric field which results in an overall contraction of the lattice but taking advantage of weaker bond-bending relaxations rather than shortening stiff covalent bonds themselves. Similar effects have been seen in covalent alloys [Petkov *et al.*, 1999b; Jeong *et al.*, 2001].

Despite these issues, PDF fits were carried out on the K^+ and Na^+ intercalated $Ti_3C_2T_x$ samples

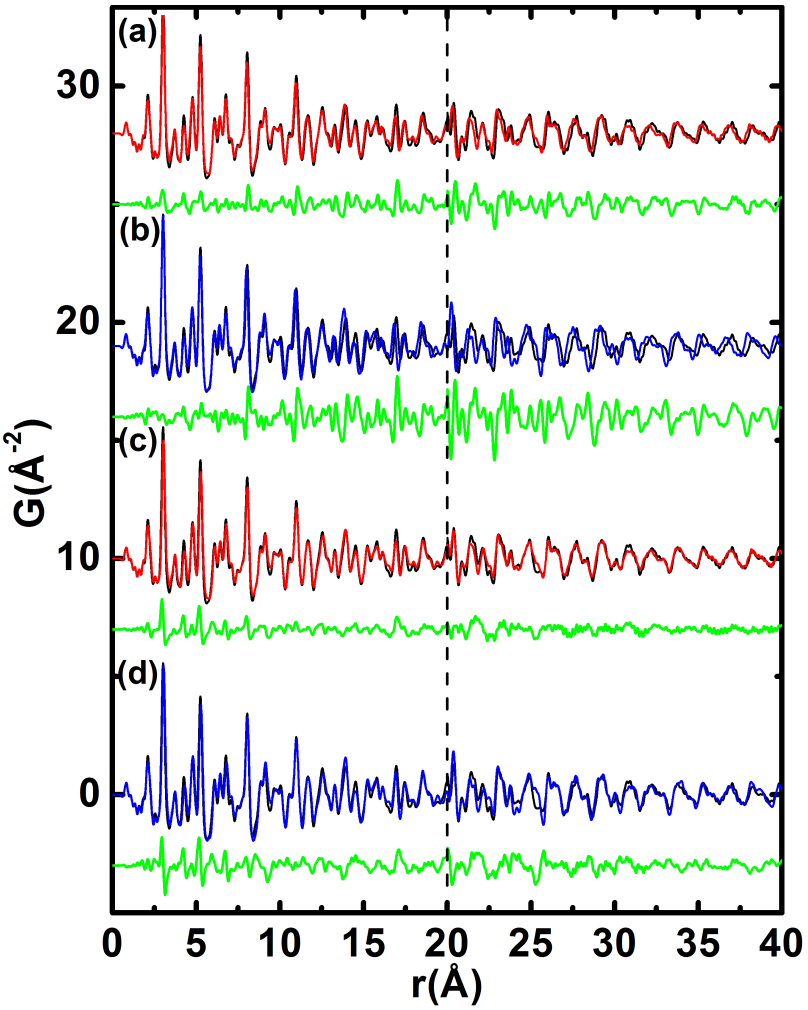

Figure 3.3: The comparison between experimental PDFs of pristine and intercalated $Ti_3C_2T_x$ is made with black, red and blue curves corresponding to pristine, Na^+ and K^+ intercalated samples, respectively. The green lines offset below are the differences. Data in the high-r region from 20 Å to 40 Å are magnified 2 times for clarity. In (a) and (b), the stretching transformation is not applied to the intercalated samples and the difference curve is dominated by the effects of the change in lattice parameter. In (c) and (d) the measured PDFs of the intercalated $Ti_3C_2T_x$ have had a stretching algorithm applied to minimize effects of lattice parameter variation in order to search in the difference curve for a clear signal coming from the intercalants themselves.

with the same structure determined for pristine $Ti_3C_2T_x$. The fits are shown in Fig. 3.2(b) and (c) and the refined parameters are in Table 3.1. No additional features originating from the intercalant ions were observed, indicating that these ions are disordered and do not sit at well defined locations. They were, therefore not included in the model. Their presence in the actual structure is indicated by the presence of a long-wavelength dip in the residual function of the fits to the intercalated data (Fig. 3.2(b), (c)). This results from missing atomic density in the model due to the absence of the Na^+/K^+ ions in the model. Nonetheless, the quality of the fits are good (surprisingly they are better than the unintercalated fits) suggesting that there is not a significant modification of the MX structure on intercalation. The fits to the intercalated compounds allow us to analyze the structure in a quantitative way, for example, to explore the bond valence sum (BVS) [Brown and Altermatt, 1985] of Ti in the intercalated and non-intercalated structures. The valence of a bond, V_{ij}, is correlated with the bond length, R_{ij} through the equation $V_{ij} = \sum exp[(R_0 - R_{ij})/B]$ where R_0 is the bond length of unit valence and can be found in the table given by Brown and Altermatt [Brown and Altermatt, 1985] and B is an empirical parameter with a typical value of 0.37. The atomic valence is estimated by summing the bond valences of all the bonds associated with an atom. Since the R_0 value for a Ti-C pair has not been tabulated, we determined it using the same equation by assuming the C atom in the pristine MXene has a total valence of 4+. In this way, we obtained an averaged $R_0 = 1.983(6)$ Å that was fixed in the subsequent BVS analysis. The top and bottom Ti atoms of a Ti_3C_2 layer (e.g.Ti(1)) are bonded to three C atoms and three O/F atoms. The contribution from O/F atoms to the BVS of terminated Ti atom is weighted by their mole ratio. R_0 values of 1.791 Å and 1.723 Å for Ti-O and Ti-F bonds, respectively, are used. The calculated BVS results are summarized in Table 3.2. In a pristine MXene, the bond valence sums for Ti atoms on the surface and inside the layer are calculated to be ∼3 and ∼4, respectively. Upon intercalation of either Na^+ or K^+, the BVS of the Ti atoms changes so that the charge differential between the surface and "bulk" Ti ions becomes less, though the average valence on the Ti does not change much. This is further evidence that the doped charge may be confined to defect states in the MX layer but not in the Ti-C bonds, though this needs to be checked by other methods.

Table 3.2: Summary of bond valence sum for Ti and C atoms in pristine and intercalated $Ti_3C_2T_x$.

	pristine	Na^+	K^+
Ti(1)	3.11(6)	3.37(6)	3.56(5)
Ti(2)	4.1(1)	3.69(9)	3.62(8)

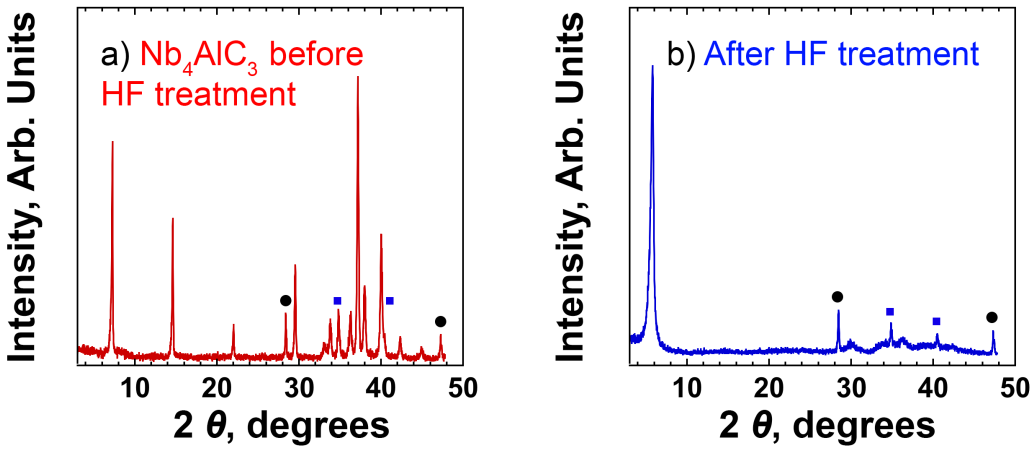

Figure 3.4: XRD diffraction patterns for Nb_4AlC_3 before (a) and after HF treatment (b). The black circles represent crystalline silicon added as an internal standard; the blue squares represent NbC present as a phase impurity in the original Nb_4AlC_3 sample.

3.3.2 Nb_4C_3 MXene

We now turn to Nb_4C_3 MXene. When the XRD pattern of the dried powder after etching (Fig. 3.4(a)) is compared to its precursor, Nb_4AlC_3 (Fig. 3.4(a)), the latter's peaks disappeared and were replaced by a broadened (0002) peak at a 2θ of 5.77°, corresponding to a c-lattice parameter (c-LP) of 3.059 nm. The original Nb_4AlC_3 (0002) peak occurs at a 2θ of 7.23° (2.242 nm). This more than 0.6 nm expansion along the [0001] was observed similarly for Nb_2CT_x and attributed to the intercalation of water layers or ions between the MXene sheets [Naguib *et al.*, 2013].

The structure of crystalline Nb_4AlC_3 has been previously reported [Hu *et al.*, 2007]. It has a hexagonal structure with $a = b = 3.1296$ Å, $c = 24.1208$ Å (Space group $P6_3/mmc$, No. 194). The

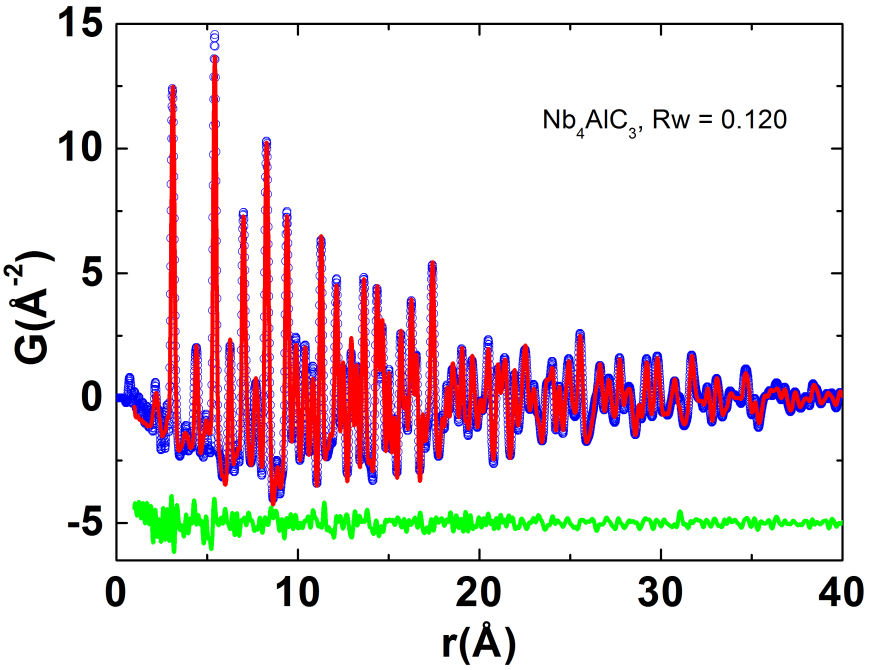

Figure 3.5: PDF fit of MAX parent Nb_4AlC_3. Blue circles, red curves correspond to observed, simulated PDF data, respectively, with green difference curves offset below.

atomic positions are Nb1 at *4f* (1/3, 2/3, z), Nb2 at *4e* (0, 0, z), Al at *2c* (1/3, 2/3, 1/4), C1 at *2a* (0, 0, 0) and C2 at *4f* (2/3, 1/3, z), respectively. We used this structural model and fitted with PDF data of MAX parent. The PDF fit is shown in Fig. 3.5 and the refined parameters are summarized in Table 3.3.

Table 3.3: Structures of the Nb_4AlC_3 and Nb_4C_3 MXene. The space-group is $P6_3/mmc$. For Nb_4AlC_3 the atoms are on the following special positions: Nb1 at $4f$ (1/3, 2/3, z), Nb2 at $4e$ (0, 0, z), Al at $2c$ (1/3, 2/3, 1/4), C1 at $2a$ (0, 0, 0) and C2 at $4f$ (2/3, 1/3, z). For Nb_4C_3 MXene, terminating O/F atoms are on (0, 0, z) with O/F mole ratio to be 3:1 that was determined from an EDX experiment. Water molecules are introduced to sit between the layers. The total content of water is constrained by the EDX result. As constrained by the space group the water molecules could sit at $2b$ (0, 0, 1/4), $2c$ (1/3, 2/3, 1/4), $2d$ (2/3, 1/3, 1/4), $6h$ (x, $2x$, 1/4) or $12j$ (x, y, 1/4) positions.

-	Nb_4AlC_3	$Nb_4C_3T_x$
R_w	0.120	0.281
a (Å)	3.1296	3.1331
c (Å)	24.1238	31.0801
z(C)	0.1090	0.0806
z(O/F)	-	0.1865
z(Nb1)	0.0548	0.0444
z(Nb2)	0.1577	0.1221
x(O)(6h)	-	0.0900
x(O)(12j)	-	0.3274
y(O)(12j)	-	0.9195
O_{occ}(2b)	-	0.0108
O_{occ}(2c)	-	0.0027
O_{occ}(2d)	-	0.0008
O_{occ}(6h)	-	0.2261
O_{occ}(12j)	-	0.2679
U_{iso}(O/water) (Å^2)	-	0.0036

U_{iso}(F) (Å^2)	-	0.0132
U_{iso}(O) (Å^2)	-	0.0800
U_{11}(C) (Å^2)	0.0132	0.0208
U_{33}(C) (Å^2)	0.0766	0.0003
U_{11}(Al) (Å^2)	0.0370	-
U_{33}(Al) (Å^2)	0.0140	-
U_{11}(Nb) (Å^2)	0.0043	0.0074
U_{33}(Nb) (Å^2)	0.0023	0.0029
δ_2 (Å^2)	2.5854	4.0401
Q_{damp} (Å^{-1})	0.0456	0.0826
Q_{broad} (Å^{-1})	0.0275	0.0449

To gain further insight into the structure of $Nb_4C_3T_x$, atomic pair distribution function analysis was carried out. Structural modelling was carried out using the PDFgui [Farrow *et al.*, 2007] and DiffPy-CMI [Juhs *et al.*, 2015] programs. The experimental PDF of $Nb_4C_3T_x$ is shown in Fig. 3.6. The sharp peaks observed over the entire range plotted suggest a well-ordered local structure. For the structural model, the space group $P6_3/mmc$ was used. The c-LP (3.1 nm) allows for two Nb_4C_3 slabs per unit cell. The surface of the Nb_4C_3 slabs is terminated with O and F atoms as evidenced by the EDX results. Among three possible positions, i.e. (0, 0, z), (1/3, 2/3, z) and (2/3, 1/3, z) for the terminating groups, as constrained by the space group, a better fit was obtained when the O/F atoms were placed on (0, 0, z), yielding a ∼1.5% lower agreement factor R_w than the other two alternatives. We further introduced water molecules between the layers sitting at Wyckoff positions 2b (0, 0, 1/4), 2c (1/3, 2/3, 1/4), 2d (2/3, 1/3, 1/4), 6h (x, 2x, 1/4) or 12j (x, y, 1/4). The total amount of water is constrained by the oxygen content from EDX. The PDF fit and structural model are displayed in Fig. 3.6. Interestingly, a shoulder peak around ∼3.3 Å(inset of Fig. 3.6(a) and Fig. 3.7) was found for $Nb_4C_3T_x$ but was not captured by the model. Together with the overall poor fit of the undistorted model, this indicates the presence of a structural distortion

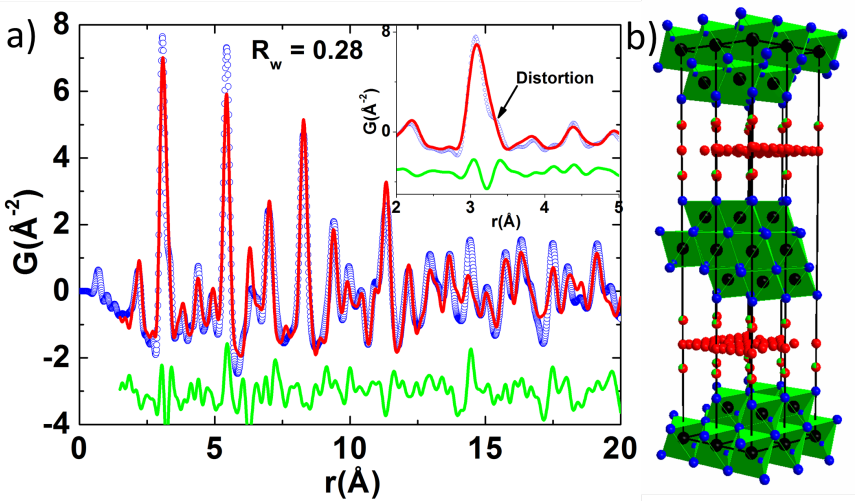

Figure 3.6: (a) PDF fit of $Nb_4C_3T_x$: blue circles are the measured data, the red solid line is the calculated PDF of the best-fit structural model, and the green curve offset below is the difference curve. The inset shows the expanded r-region from 2 Å to 5 Å where a shoulder peak at ~3.3 Å can be seen, indicating a distortion in the Nb_4C_3 slab. (b) The polyhedral representation of the undistorted $Nb_4C_3T_x$ structure. The Nb, C, O/F atoms are in blue, black, red/green colours. The intercalated water molecules are represented by sheets of oxygen atoms.

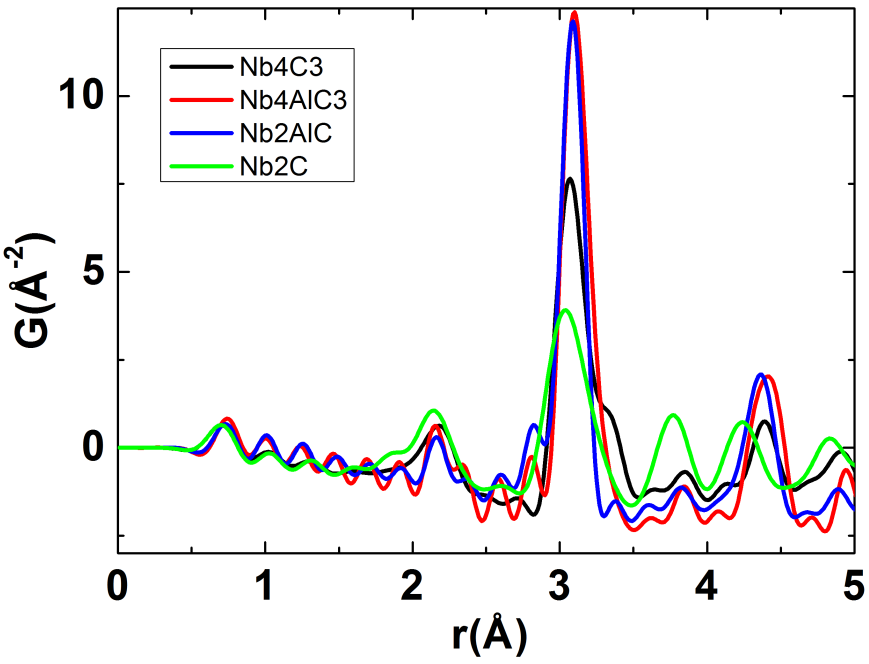

Figure 3.7: Pair distribution functions shown over a low-r region up to 5 Å for Nb_2CT_x and $Nb_4C_3T_x$ MXenes, and their corresponding MAX phases. The shoulder peak at ∼3.3 Å is only present in the $Nb_4C_3T_x$ MXene, and not in Nb_4AlC_3, Nb_2AlC, or Nb_2CT_x.

within the Nb_4C_3 layer. Simple distorted models were tried without success, and more detailed models are being investigated at this time. This shoulder was not seen in the earlier PDF study of $Ti_3C_2T_x$, whose layers are undistorted at the local scale [Shi *et al.*, 2014].

3.4 Conclusion

The structures of nanocrystalline pristine, potassium hydroxide and sodium acetate intercalated new two-dimensional materials Ti_3C_2 MXenes were studied using the x-ray atomic pair distribution function technique. Pristine MXene has a hexagonal structure with $a = b = 3.0505(5)$ Å, $c = 19.86(2)$ Å (S.G. $P6_3/mmc$ No. 194). Both hydroxyl and fluoride terminating species are present. The intercalation of K^+ or Na^+ ions expands the Ti_3C_2 layers perpendicular to the planes but shrinks the in-plane a and b lattice parameters. The atomic structure of Nb_4C_3 MXene has been also determined using PDF technique. In contrast to Ti_3C_2 MXene, there are significant amount of water molecules residing between the layers. Knowing the precise atomic structures would be foundational first step to establish structure-performance correlation in these promising energy storage materials.

Chapter 4

Structure of zirconium phenyl-phosphonate ion exchangers

4.1 Introduction

To satisfy the ever-increasing demand for energy a focus of much current scientific research is to find better performing materials for energy conversion. The zirconium based phosphate/phosphonate unconventional metal organic frameworks (UMOFs) [Dines *et al.*, 1983; Alberti *et al.*, 1993; Mal *et al.*, 2005; Wang *et al.*, 2003; Subbiah *et al.*, 2005; Gagnon *et al.*, 2012; Vivani *et al.*, 2008; Clearfield, 2008] show great promise in this regard. They exhibit strong affinity towards +3 ions while discriminating against ions with lower valences (e.g. +1/+2). Therefore these hybrid materials are good candidates for separating lanthanide ions (L^{3+}) from actinide (A^{3+}) ions, for example, in spent nuclear fuel rods, by first oxidizing the actinide ions to AO_2^+ then applying these UMOFs to take up L^{3+} that can be recycled using techniques such as chromatography. In order to understand their selectivity for +3 ions, it is necessary to know the atomic structure of the material. Unfortunately the nanocrystalline nature of these materials makes the structural determination from a laboratory x-ray diffractometer impossible, as evidenced by the x-ray diffraction patterns from these materials shown in Fig. 4.1(b) and (c). On the other hand, the atomic pair distribution

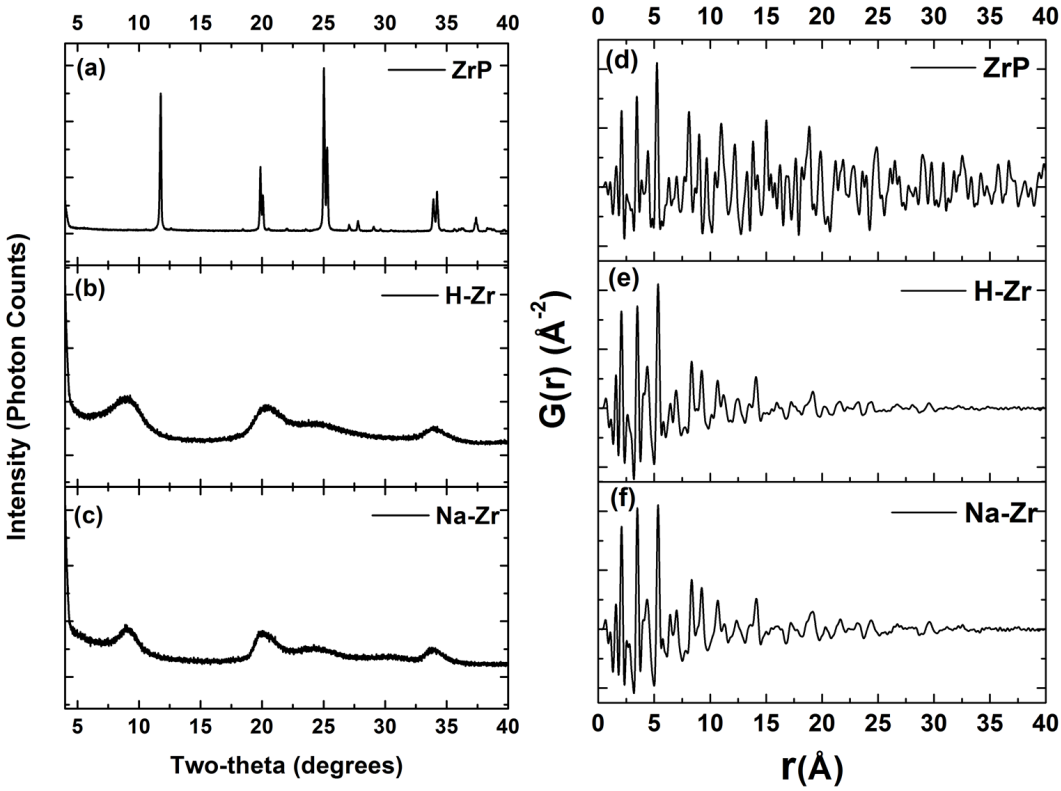

Figure 4.1: (a)-(c) are laboratory XRD patterns for bulk, H-Zr-hybrid and Na-Zr-hybrid, respectively. Their corresponding PDFs are plotted up to 40 Å and shown in (d)-(f), respectively.

function (PDF) technique, which treats the diffuse scattering and Bragg scattering signals on the equal footing, is a powerful tool for probing the local structure of nanomaterials [Shi *et al.*, 2014; Juhás *et al.*, 2006; Billinge and Levin, 2007; Billinge and Kanatzidis, 2004]. Here we used the PDF method and for the first time determined the structures of two zirconium based UMOFs, H-Zr-hybrid and Na-Zr-hybrid. They both have two-dimensional layered structures with weak inter-layer correlations. As a consequence, their PDFs can be well modelled by a single slab of atoms cut from bulk phenylphosphate [Poojary *et al.*, 1993]. To try and determine the coordination environment of the +3 ions after ion exchange, we loaded the samples with Tb (17 wt%) and carried out a difference PDF (d-PDF) measurement [Li *et al.*, 2011b; Chapman *et al.*, 2006; Harrington *et al.*, 2010; Chapman *et al.*, 2005; Chupas *et al.*, 2007; Petkov *et al.*, 2002a] on Na-Zr-hybrid with and without Tb^{3+} loaded. The Tb was found to reside between the layers and to have a well defined coordination environment of oxygen, but no evidence of Tb-Tb correlations in the layer were found, indicating that intercalated Tb is disordered in the layer and does not cluster, possibly in part due to the low Tb concentration.

4.2 Experiment

Our collaborator at Texas A&M University, Rita Silbernagel from Prof. Abraham Clearfield group prepared the bulk and nanoparticulate ZrPP samples for current PDF study.

The chemical compositions of two zirconium based hybrid samples are summarized in Table. 4.1. They both have phosphate (PO_4) and phenylbiphosphonate ($PO_3C_6H_4PO_3$) functional groups.

Synchrotron x-ray total scattering experiments were conducted at beamline X17A at the National Synchrotron Light Source (NSLS) at Brookhaven National Laboratory. The incident x-ray had an energy of 66.6580 keV (λ=0.1860 Å). The sample-to-detector distance was 203.908 mm. Nickel was also measured as a standard material to calibrate the sample-detector distance and to determine the Q_{damp} and Q_{broad} parameters which are the parameters that correct the PDF envelope function for the instrument resolution effects [Proffen and Billinge, 1999; Farrow *et al.*, 2007].

Table 4.1: Summary of hybrid ZrP nanoparticles and control sample. The chemical compositions are determined from combined elemental analysis (EA), thermal gravimetric analysis (TGA) and electron microscopy.

Samples	Chemical formula
α-ZrP	$Zr(HPO_4)_2.H_2O$
H-Zr	$Zr(O_3PC_6H_4PO_3)_{0.34}(O_3POH)_1(OH)_{1.76}{\cdot}1.63H_2O$
Na-Zr	$Zr(O_3PC_6H_4PO_3)_{0.38}(O_3PONa)_{0.89}(O_3POH)_{0.05}(OH)_2{\cdot}1.45H_2O$

The refined values of $Q_{damp} = 0.0421$ Å^{-1} and $Q_{broad} = 0.0201$ Å^{-1} were fixed in the subsequent model fits to PDF data. Structural modeling was carried out using the PDFgui [Farrow *et al.*, 2007] and Diffpy-CMI [Juhs *et al.*, 2015] programs.

In order to detect the position of Tb ions, a difference PDF approach was adopted where PDFs of Na-Zr sample with and without Tb loading were measured, respectively. The synchrotron x-ray PDF experiment was carried out at beamline ID-28 at National Synchrotron Light Source II (NSLS II) at Brookhaven National Laboratory. The experimental setup was similar to those described in the previous paragraph but with an incident x-ray energy of 65.1294 keV ($\lambda = 0.1904$ Å) and a sample-to-detector distance of 300.510 mm which was calibrated by a nickel standard. We scaled and subtracted PDF measured for Na-Zr without Tb ion from the one containing Tb by finding a proper constant which minimizes the difference between the two PDFs in a r-range up to 40 Å.

4.3 Structure of hybrids

The lab x-ray diffraction pattern using a copper K_α radiation for bulk zirconium phosphate and H-Zr, Na-Zr hybrid materials are shown in Fig. 4.1 (a),(b) and (c), respectively. The bulk crystalline zirconium phosphate has sharp Bragg peaks while their nanocrystalline counterparts have only broad and diffuse nature, indicating their nanocrystalline nature. The low information content of

the data is not sufficient to constrain a unique structure solution. Nonetheless from the position of the first diffraction peak we can estimate an average inter-layer spacing to be ∼9.81 Å, although the breadth of that peak indicates that this is not completely uniform, or alternatively that there are only a few layers stacked in each particle.

For a comparison the corresponding PDFs are shown in Fig. 4.1(d)-(f). The PDF of the crystalline ZrP control sample has sharp peaks up to 40 Å where we cut off the plot. In contrast to the laboratory XRD result, the PDFs of the hybrid samples also exhibit sharp correlation peaks at low-r, but they diminish in amplitude with increasing-r, disappearing by 40 Å, indicating a well defined local structure, but an absence of long-range order consistent with the lab XRD data. The PDF provides rich structural information that makes structure determination possible. The range of structural coherence for these hybrid materials are estimated to be ∼40 Å as we see the PDF signals gradually die off at this correlation length. It is interesting to see that the PDFs of both hybrid samples are very similar, indicating a shared structure between them.

The structure of bulk zirconium phosphate (α-ZrP) has been solved and reported by Clearfield *et al.* [Clearfield and Smith, 1969]. α-ZrP has a layered structure consisting of corner-shared ZrO_6 octahedra and PO_4 tetrahedra with water molecules intercalated between the layers. It has a monoclinic structure (space group $P2_1/c$) with Zr, P and O atoms sitting at non-special (x, y, z) positions. We adopt the same structure model as a starting point for PDF modelling and the fit is shown in top panel of Fig. 4.2. The fits put the peaks in the right position, suggesting the current model captures the main structural features. The agreement factor R_w is ∼22% which is a little high for a PDF fit to bulk crystalline data.

To search for the structures for the hybrid materials, we sought different possible starting models from the literature. Four representative structure models reported in the literature were chosen as trial candidates. Since they are layered structures in nature, only a single slab of atoms is schematically plotted in Fig. 4.3. The first model is inherited from α-ZrP as shown in Fig. 4.3(a). A similar structure to α-phase as reported for zirconium phenyl-phosphonate [Poojary *et al.*, 1993] is shown in Fig. 4.3(d). Its inorganic layer has same motifs as found in α-phase. The difference is

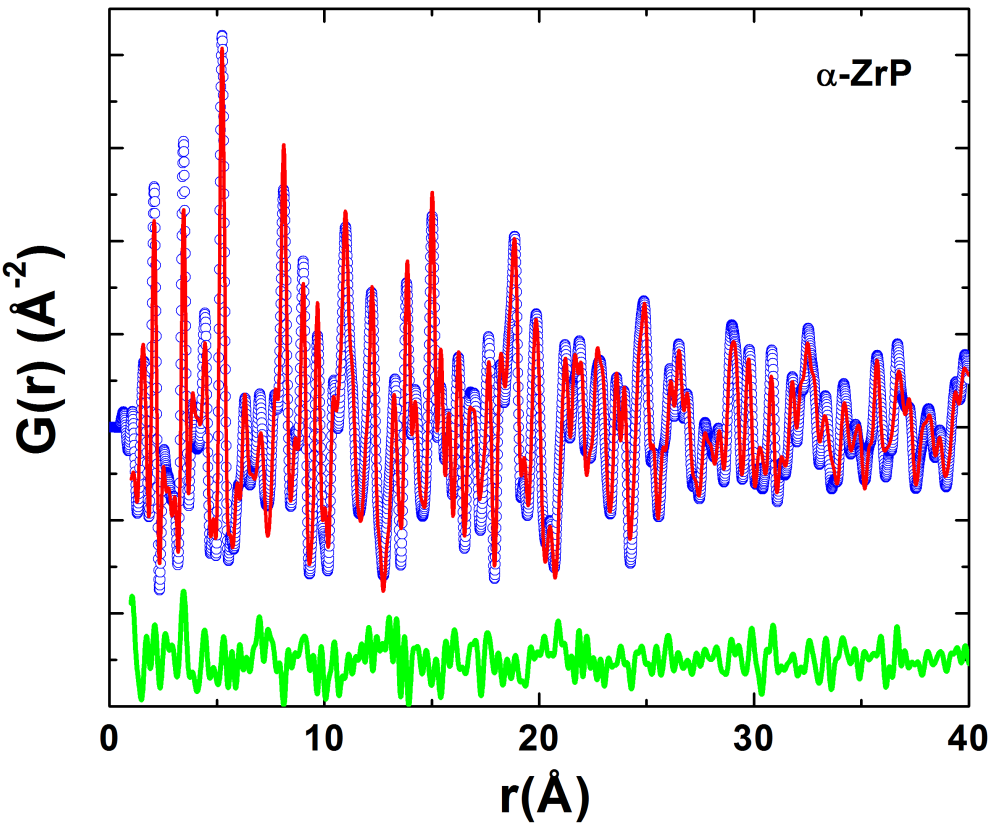

Figure 4.2: PDF fit to bulk zirconium phosphate sample in a r-range up to 40 Å. Blue circles, red solid curves are measured and simulated PDFs, respectively, with green difference curve offset below.

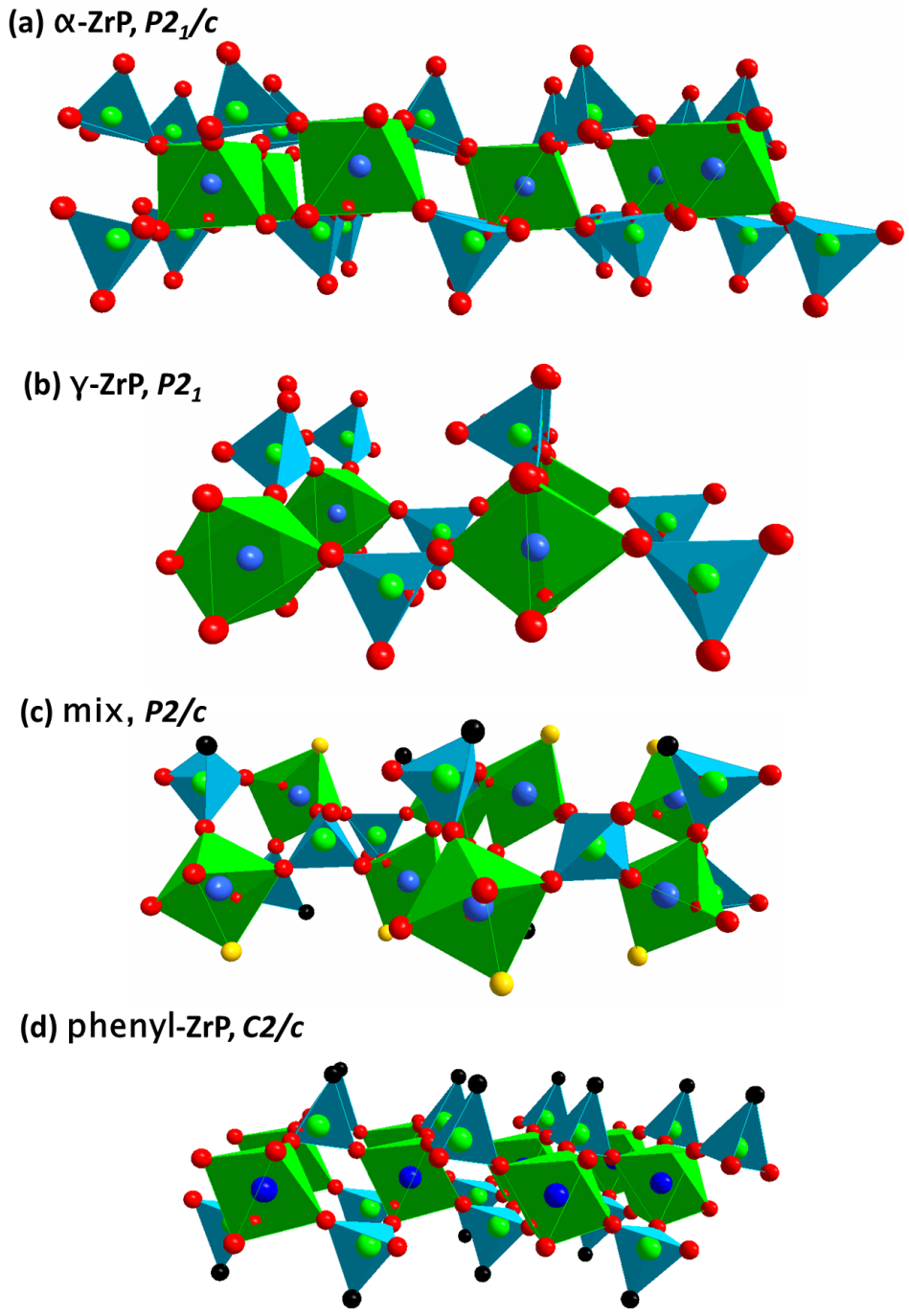

Figure 4.3: Single layer structure model for (a)α-ZrP (b) γ-ZrP (c) mixed zirconium phosphate/phosphonate (d)zirconium phenylphosphonate . Zr, P, O, C and F atoms are in blue, green, red, black and yellow respectively. The green and blue shaded areas represent ZrO_6 octahedra and PO_4 tetrahedra, respectively.

that zirconium atoms in phenyl phase are in the same atomic plane whereas they sit slightly above and below the plane in the α-phase. Three coplanar Zr atoms form an equilateral triangle and the P atoms are located at the center of these triangles above and below the plane [Poojary *et al.*, 1993]. The phenyl phase has a monoclinic structure with space group $C2/c$. Zr atoms sit at (3/4, 1/4, 1/2) while P, O, C atoms are at (x, y, z) positions. There are other reports of ZrP structures where the inorganic layers, i.e. the arrangements of ZrO_6 octahedra and PO_4 tetrahedra are different from either the α or phenyl phases. Two such structures are γ-ZrP [Poojary *et al.*, 1995] and mixed phosphate/phosphonate [Byrd *et al.*, 1996; Poojary *et al.*, 1994] and their structural models are plotted in Fig. 4.3(b) and (c), respectively. The former has a space group of $P2_1$ while the latter of $P2/c$. In both models the atoms sit at general (x, y, z) positions.

We move on to fit PDFs of hybrid ZrP samples with these four structural candidates, i. e., α, γ, mixed and phenyl phases, respectively. The PDF of hybrid nanoparticle can be calculated theoretically from atomic models by multiplying the bulk PDF, $G_{bulk}(r)$, by a spherical characteristic function $\gamma(r)$ as described in Chapter 2. [Gilbert, 2008; Farrow and Billinge, 2009; Masadeh *et al.*, 2007; Shi *et al.*, 2013; Farrow *et al.*, 2014], As an initial test, we did PDF modelling on H-Zr-hybrid in a r-range of 1-40 Å and the fit results are displayed in Fig. 4.4. The agreement between calculated and measured PDFs are good up to ∼7 Å, which indicates the basic motifs, i.e. ZrO_6 octahedra and PO_4 tetrahedra and their arrangement in a local environment up to ∼7 Å is similar. However, this agreement becomes worse as r increases which can be clearly seen at r larger than ∼15 Å. Among all models, the "mixed" model gives the worst fit when compared with others. The mismatch starts right after ∼7 Å, indicating the stacking of octahedra and tetrahedra units are not correct. Among α, γ and phenyl structures, phenyl model gives the overall best agreement up to ∼15 Å. In addition, we prefer phenyl structure as it has a higher symmetry with fewer positional parameters (15 for the slab structure) than α and γ phases which each contains 33 atomic positional variables. Taking into account both well explained local structure and poorly described long-range ordering in phenyl model, it is reasonable to assume that its structure is basically correct but the spherical morphology is not which causes the mismatch at high r. Considering the layered nature of hybrid materials, it

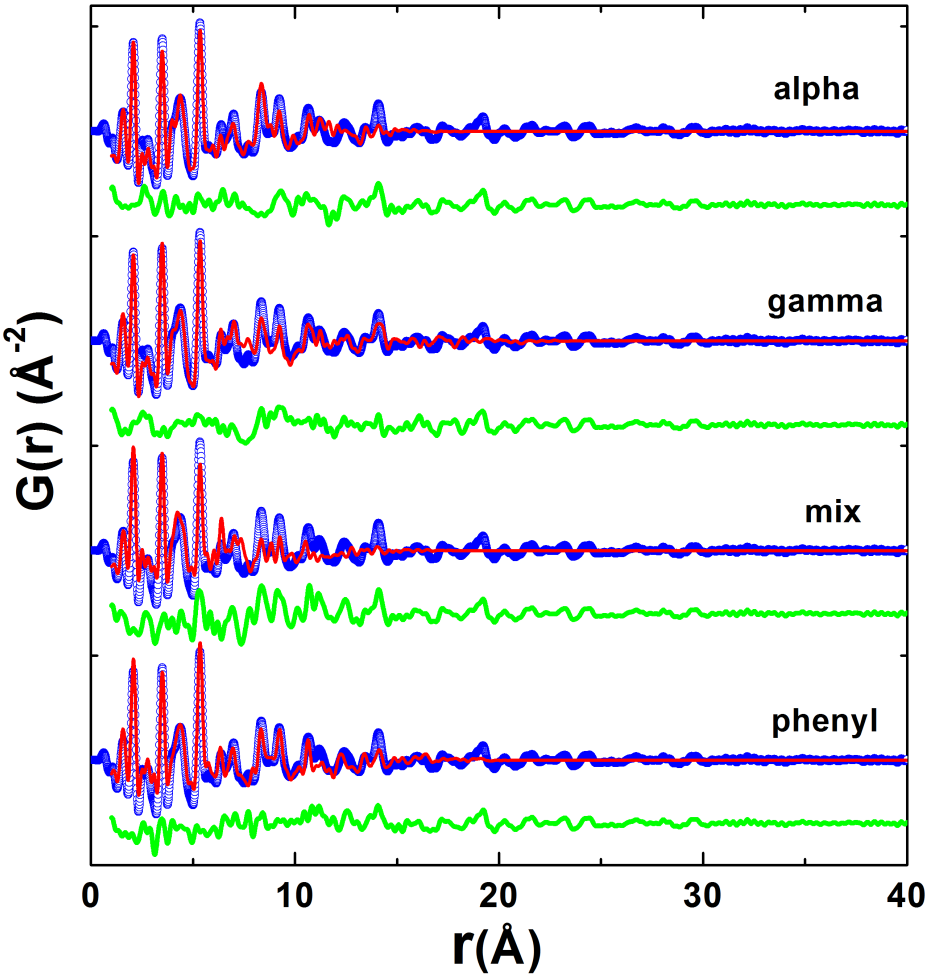

Figure 4.4: PDF fits to H-Zr-hybrid sample in a r-range up to 40Å using four structural candidates shown in Fig. 4.3. Blue circles, red solid curves are measured and simulated PDFs, respectively, with green difference curve offset below.

has been reported at nanometer scale the layers tend not to stack in a good registry but instead stack in an disordered fashion, which is known as "turbostratic" disorder [Ghidiu *et al.*, 2014; Petkov *et al.*, 2002b; Petkov *et al.*, 1999a; Naguib *et al.*, 2013]. In such situations a single-slab model may be sufficient to explain the data [Naguib *et al.*, 2013], even though we know from the low angle diffraction peak in the XRD data that multiple layers are stacked in the actual material. Consequently, we build up a model by cutting a single layer of atoms from bulk phenylphosphonate lattice. The PDF of the single slab created can be readily calculated as the Fourier transform of scattering intensity which is based on Debye scattering equation [Debye, 1915].

The PDF modeling with a single slab model is displayed in Fig. 4.5(a), (b) with a ball and stick model shown at the bottom (Fig. 4.5(c)). The simulated curves well match the experimental ones even at a r-range up to 40 Å, confirming our inference. The refined structural parameters are summarized in Table. 4.2.

Table 4.2: Summary of PDF fit results for Zr hybrid materials using a single slab modelling. The space group is $C2/c$ (No. 15) with Zr at (3/4, 1/4, 1/2) and P, O, C atoms sitting at (x, y, z), respectively. Previous structural report for bulk zirconium phenylphosphonate (ZrPP) [Poojary *et al.*, 1993] is also listed as a reference.

-	H-Zr	Na-Zr	ZrPP
a (Å)	9.1336	9.1291	9.0985
b (Å)	5.3932	5.3858	5.4154
c (Å)	30.0000	29.8580	30.2350
β (°)	101.96	100.93	101.33
x(P)	0.9490	0.9436	0.9380
y(P)	0.7434	0.7464	0.7290
z(P)	0.5585	0.5566	0.5567
x(O1)	0.0700	0.0732	0.0650

y(O1)	0.7124	0.7368	0.7200
z(O1)	0.5290	0.5341	0.5298
x(O2)	0.8336	0.8332	0.8380
y(O2)	0.4972	0.5114	0.5090
z(O2)	0.5530	0.5507	0.5471
x(O3)	0.8609	0.8564	0.8470
y(O3)	0	0.0030	0.0310
z(O3)	0.5490	0.5503	0.5436
x(O4/C)	0.0299	0.0278	0.0290
y(O4/C)	0.7192	0.7047	0.7340
z(O4/C)	0.6060	0.6217	0.6159
C_{occ}	0.4295	0.4218	-
U_{iso} (Zr) (Å^2)	0.0043	0.0065	0.0080
U_{iso} (P) (Å^2)	0.0036	0.0026	0.0110
U_{iso} (O) (Å^2)	0.0037	0.0103	0.0180
U_{iso} (C) (Å^2)	0.0043	0.0065	0.1530
r(Zr-O) (Å)	2.0233×2	2.0664×2	2.0510×2
	2.0941×2	2.1011×2	2.0710×2
	2.0947×2	2.1013×2	2.0910×2
r(P-O/C) (Å)	1.4688	1.9629	1.8210
r(P-O) (Å)	1.5614	1.4681	1.4910
	1.5965	1.5881	1.5410
	1.6820	1.6067	1.5510

The slab has a dimension of ∼35 Å×35 Å. Combining laboratory XRD that yields information about inter-layer spacing and current PDF that gives intra-layer structural details, we are now able to build a full three dimensional structure model for these hybrid materials which is schematically

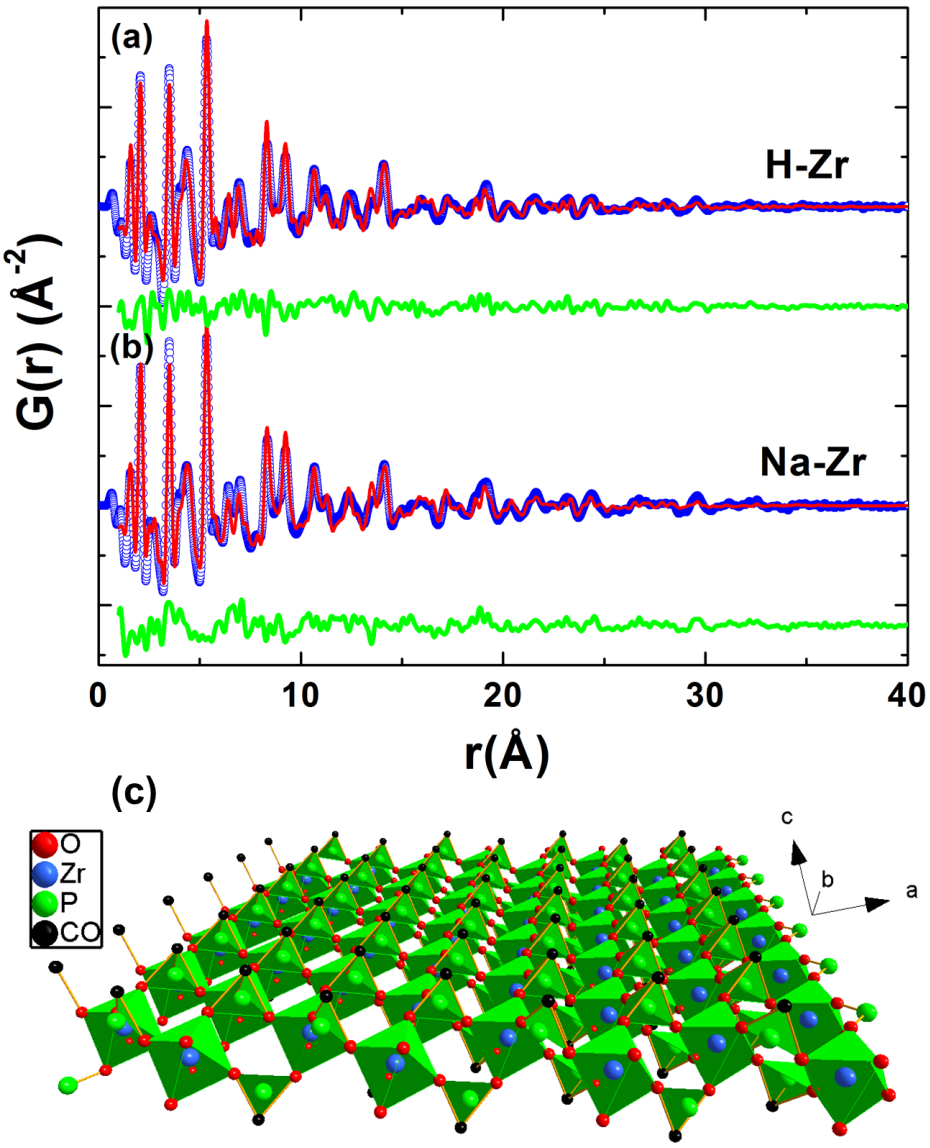

Figure 4.5: (a), (b) are PDF fits of H-Zr-hybrid and Na-Zr-hybrid, respectively. The blue circles, red solid lines are experimental, calculated PDFs, respectively, with green difference curves offset below. (c) The polyhedral representation of a single nanocrystalline slab for hybrid materials. Zr, P, O and C atoms are in blue, green, red and black, respectively.

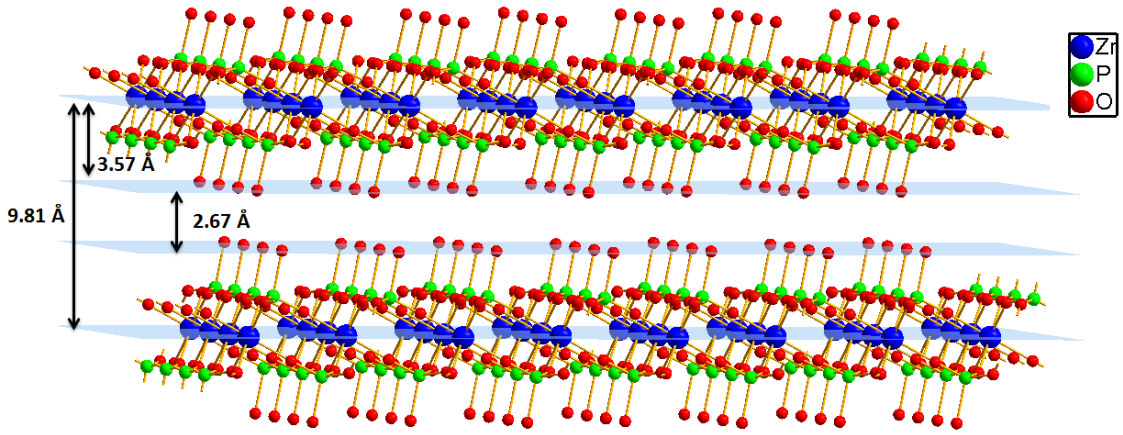

Figure 4.6: The structure model for Na-Zr-hybrid sample. The distances between atomic planes are labelled. The Tb environment is circled by dashed line. Zr, P, and O atoms are in blue, green and red, respectively.

drawn in Fig. 4.6. The slab has a lateral dimension of ∼35 Å with a thickness of ∼6.22 Å for H-Zr-hybrid and ∼7.14 Å for Na-Zr-hybrid, respectively. The inter-layer distance is ∼9.81 Å. Current model is in general consistent with previously proposed schematic structure models [Gagnon *et al.*, 2012; Clearfield, 2008]. However from PDF data we can gain more insights on the structure. We now know (i) the dimensions of nanocrystalline slabs (ii) the precise atomic arrangement in the slabs (iii) the layers are stacked in a disordered fashion.

4.4 Local structural environment of Tb ions

Since we have a full 3D structure model for these hybrid materials, we are in a good position to investigate their high selectivity for +3 ions. As an initial attempt, we try to locate terbium ion, one of +3 lanthanide ions, in Na-Zr-hybrid. This was done by a difference PDF approach where PDFs of Na-Zr-hybrid with and without Tb ion were collected and subtracted from each other (with Tb minus no Tb). In this way what is left in the difference PDF yields local structural environment for Tb ion. The PDFs of Na-Zr-hybrid without Tb ion and with 17 wt% Tb ion were measured

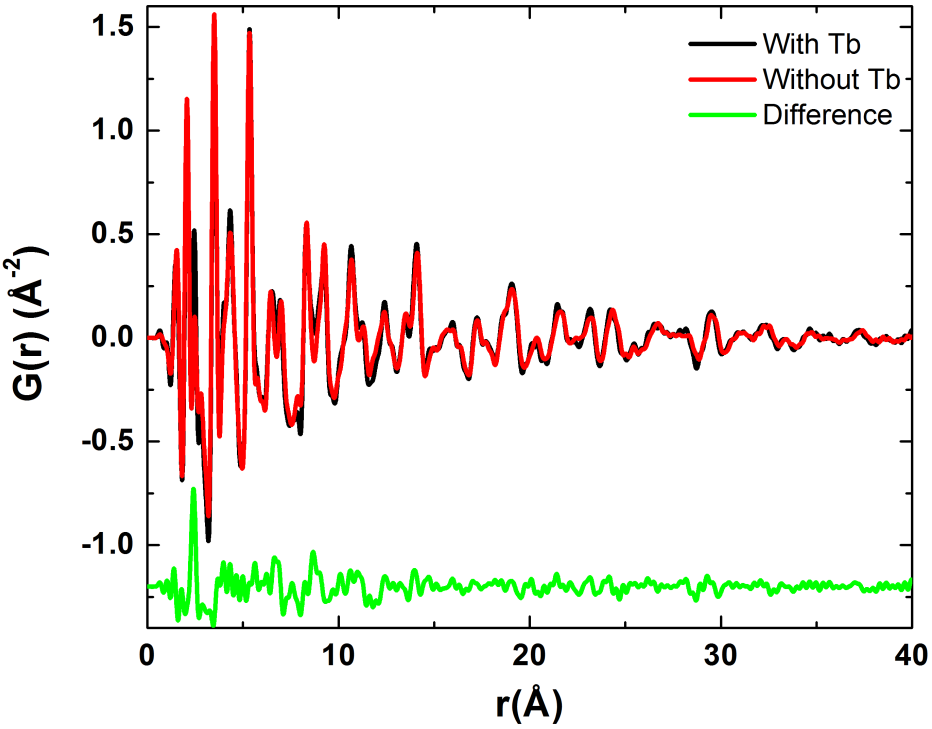

Figure 4.7: The PDFs of Na-Zr-hybrid with Tb ion (red) and without Tb ion (blue) with green difference curve offset below.

and their PDFs together with difference PDF are shown in Fig. 4.7 in a r-range up to 40 Å. We see a strong peak at 2.41 Å in the difference PDF curve sitting well above the noise level which is assigned as Tb-O bond. The fact we didn't see any other strong peak at higher-r region suggests the correlation of Tb with other species is weak and Tb ion is disordered between the layers. The key to a solution is to determine the ion exchange capacity. Together with elemental analysis one should be able to determine the localization of Tb^{3+} ion. This will be included into a follow-up study.

4.5 Conclusion

The three dimensional atomic structures of two zirconium based phosphate/phosphonate (ZrP) unconventional metal organic frameworks, i.e. H-Zr-hybrid and Na-Zr-hybrid, have been success-

fully determined using combined laboratory x-ray diffraction (XRD) and atomic pair distribution function (PDF) analysis. Both hybrid materials have layered structures with an inter-layer spacing of $\sim$ 9.81 Å which is determined from the low 2θ reflection peak in laboratory XRD, whereas the precise intra-layer structural details have been obtained from PDF data. For both materials their intra-layer structures were shown to to be well explained by a single nanocrystalline slab of a known bulk phenylphosphate structure [Poojary *et al.*, 1993] with a lateral dimension of $\sim$35 Å. To understand the high selectivity of +3 ions from these hybrid materials, the difference PDF measurement has been carried out on Na-Zr-hybrid with and without Tb^{3+} loading. Our result indicates that the Tb^{3+} ions sit between the layers in a disordered fashion.

Chapter 5

Bond stiffness in size dependent carbon supported platinum nanoparticles

This chapter is based on published paper [Shi *et al.*, 2013].

5.1 Introduction

Metallic nanoparticles are of interest scientifically and in novel technological applications [Bell, 2003; El-Sayed *et al.*, 2006; Roduner, 2006b; Valden *et al.*, 1998; Fu *et al.*, 2003; Pourbaix, 1974]. They can be used as catalysts in refining petroleum, hydrogenation of carbon monoxide/fats, and so on [Bell, 2003; Valden *et al.*, 1998; Pourbaix, 1974]. However some of these catalysts are not stable, for example, platinum nanparticles that serve as catalysts in solid oxide fuel cell sometimes do not function optimally [Pourbaix, 1974]. A difficulty for understanding the performance arises from both the structural complexity of heterogeneous catalyst and the sensitivity of kinetic response to the surrounding environment [Bell, 2003; Valden *et al.*, 1998; Pourbaix, 1974]. Therefore an investigation of the structure and bond stiffness of small catalyst nanoparticles is needed to further

the understanding of this important class of materials.

It is a challenge to measure the bond stiffness as a function of nanoparticle size for small nanoparticles. A common way to determine bond stiffness in bulk materials is to consider the temperature dependence of the atomic displacement parameter (ADP) measured from diffraction and fit it with a Debye [Debye, 1912] or Einstein model [Einstein, 1911]. The stiffness is directly related to the resulting Debye (θ_D) or Einstein (θ_E) temperatures. Small nanoparticles are not well studied by conventional diffraction methods, complicating this issue [Billinge and Levin, 2007]. However, the peak width in an atomic pair distribution function (PDF)[Billinge *et al.*, 1991; Jeong *et al.*, 1999] or extended X-ray absorption fine-structure spectroscopy (EXAFS) measurement [Balerna and Mobilio, 1986; Araujo *et al.*, 2006; Gilbert *et al.*, 2004; Kang *et al.*, 2006; Giulian *et al.*, 2009; Frenkel *et al.*, 2001; Sanchez *et al.*, 2009; Cuenya *et al.*, 2011; Frenkel *et al.*, 2012] yields the amplitude of atomic motion even for small particles allowing (θ_D) or (θ_E) to be determined from its temperature dependence. An additional complication is that, for small nanoparticles, there is not a direct relationship between Debye temperature and bond stiffness due to the increased fraction of undercoordinated surface atoms. These underconstrained atoms execute larger amplitude thermal motions, and have a lower Debye temperature, even when the bond stiffness of each bond has not changed, resulting in a size dependence to (θ_D) that does not originate from bond softening.

A number of EXAFS studies have been carried out to study the Debye (θ_D) or Einstein (θ_E) temperature of nanoparticles [Balerna and Mobilio, 1986; Araujo *et al.*, 2006; Gilbert *et al.*, 2004; Kang *et al.*, 2006; Giulian *et al.*, 2009; Frenkel *et al.*, 2001; Sanchez *et al.*, 2009; Cuenya *et al.*, 2011; Frenkel *et al.*, 2012]. Few studies consider the effects of the surface [Gilbert *et al.*, 2004; Frenkel *et al.*, 2001; Sanchez *et al.*, 2009; Cuenya *et al.*, 2011; Frenkel *et al.*, 2012], but to treat the effect properly requires detailed knowledge of the size and shape of the nanoparticles which is not easy to determine from EXAFS. Additionally, only the width of the nearest neighbor peak is measured in EXAFS requiring use of a correlated Debye model to account for the correlated motion of near neighbors [Jeong *et al.*, 2003]. In these respects the use of the PDF to measure (θ_D) derives some advantages since it contains structural information from all neighbors. Here we report the first PDF

study of Debye temperature vs. nanoparticle size on five samples of Pt nanoparticles supported on carbon. Our nanoparticle samples, with sizes from 1.78(2) nm to 11.2(2) nm, were studied with more than 200 temperature points between 80 K and 400 K. We report a protocol for extracting Debye/Einstein temperatures from experimental PDFs using the PDFgui program [Farrow *et al.*, 2007]. We see a monotonic decrease in (θ_D) with diameter, D. This trend is well explained by the effect of increased surface area except in the case of the 1.78(2) nm diameter nanoparticle where the measured Debye temperature is significantly depressed from that predicted. This is evidence for a softening in the bonding strength of the nanoparticles below a diameter of 2 nm though other origins cannot be ruled out.

5.2 Experiment and data analysis

5.2.1 Experiment

Our collaborator at Georgia Institute of Technology, Erin L. Redmond from Prof. Thomas Fuller group prepared the platinum nanoparticles for bond stiffness study.

Four carbon supported platinum samples were provided by Tanaka Kikinzoku Group and platinum black was purchased from Sigma Aldrich. Based on the Pt weight percentages (wt%), they were denoted as Pt 100 (Pt black), Pt 70, Pt 60, Pt 50 and Pt 30 respectively. Synchrotron X-ray total scattering experiments were conducted at beamline X17A at 11-ID-B at the Advanced Photon Source at Argonne National Laboratory. The incident x-ray has an energy of 58.26 keV (λ=0.2128 Å). The samples were measured in a flowing nitrogen cryocooler at temperatures between 80 K and 400 K (step=1.4 K). The data were truncated at Q_{max}= 23.0 Å^{-1} which avoids large termination effects while minimizing the statistical noise level, due to the increasing signal to noise ratio with the increasing Q value.

5.2.2 Particle sizes from PDF and TEM

In order to determine nanoparticle sizes we first assume they are of spherical shape and then we consider PDFs of nanoparticles as the attenuated bulk PDF $G_{Bulk}(r)$ by an envelope function $\gamma_0(r)$ as follows [Gilbert, 2008; Farrow and Billinge, 2009; Masadeh *et al.*, 2007]: In the PDFgui program, particle size can be extracted by refining the spdiameter parameter. One may refer to PDFgui document for further details [Farrow *et al.*, 2007]. PDFgui reports uncertainties on refined parameters. When correct uncertainties are propagated with the data these reported uncertainties correctly reflect the level of precision of the refined parameters. However, in many cases, including in our case, the data uncertainties are not known. The uncertainties on *G(r)* can be estimated after an initial fit of the model by Nyquist data sampling and are found as:

$$dG(r) = \sqrt{\frac{\sum_{n=1}^{N}(G_{model}(r_n) - G_{obs}(r_n))^2}{N - P}}. \tag{5.1}$$

where N is the number of data points on a Nyquist grid, P is the number of refined parameters [Jensen *et al.*, 2012]. Using these *dG(r)* one may find reliable uncertainties on the refined parameters. The average sizes from PDF for Pt 100 to Pt 30 are determined to be, respectively, 11.2(2), 3.72(2), 3.06(2), 2.47(2) and 1.78(2) nm. Nanoparticle sizes for Pt 30-Pt 70, obtained from PDF and TEM, respectively, are compared in Fig. 5.1. One may see a good agreement of average sizes between both techniques.

5.2.3 Determination of atomic displacement parameter (ADP) and mean square relative displacement (MSRD) using PDFgui

The PDFgui program [Farrow *et al.*, 2007] was used for real space modeling with fit range 1.5 Å-40 Å and the structural model was that of FCC bulk platinum (space group $Fm\overline{3}m$). We adopted a particular protocol to ensure stable refinements yielding physical parameters over the whole temperature range. The value for Q_{damp}, which models the resolution function of the instrument, was determined from a crystalline nickel calibration standard. However, a second experimental parameter, Q_{broad}, that broadens peaks with increasing r [Egami and Billinge, 2012], yielded significantly

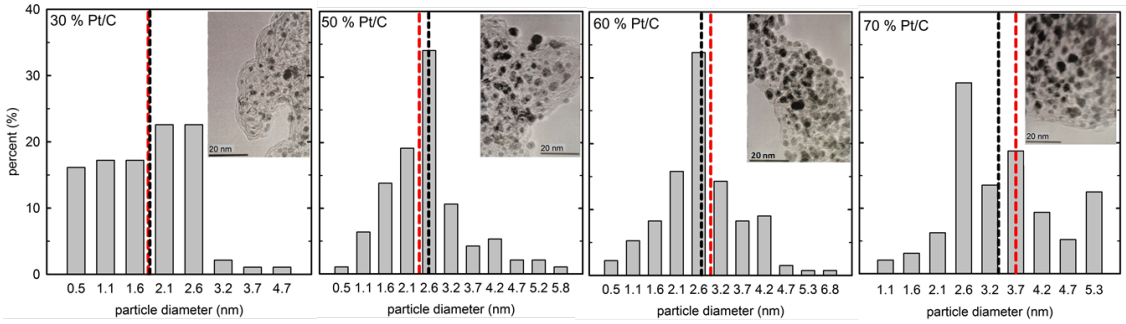

Figure 5.1: TEM images (insets) of Pt on carbon black and the distribution of Pt cluster diameters obtained from the images. From left to right are Pt 30, Pt 50, Pt 60 and Pt 70 respectively. Vertical dashed lines correspond to the average particle sizes obtained from the PDF (red) and TEM (black).

different values between the nanoparticles and the bulk calibration material suggesting there was a sample-dependent component to that broadening parameter. We therefore refined a value for Q_{broad} to the nanoparticle data at room temperature, but fixed it to this value for all other temperatures. This removed parameter correlations with the atomic displacement parameter (ADP) and spdiameter (nanoparticle size) parameters at high temperature. Finally, all the datasets were re-refined with Q_{damp}, spdiameter, and Q_{broad} fixed and the scale factor, ADP, lattice parameters and δ_2 (which accounts for motional correlations) parameters refined. The meaning of the non-structural parameters can be found in the PDFgui documentation [Farrow *et al.*, 2007]. The fits over this wide range of r yield the ADP such as would be obtained from a crystallographic refinement with no motional correlations in a bulk measurement [Egami and Billinge, 2012]. For comparison with EXAFS results that fit the nearest neighbor peak, the PDF nearest neighbor peak can also be fit directly. To do this we used a similar fitting process as described above but limited to the range 2.2-3.3 Å, which includes only the nearest neighbor peak, and setting the δ_2 and Q_{broad} parameter to zero to obtain the square-width of the atomic pair distribution (MSRD) as twice the refined ADP.

5.2.4 Debye/Einstein temperature determination

The temperature dependence of these ADPs was fit with a Debye model [Billinge *et al.*, 1991]:

$$\overline{u^2} = \left(\frac{3\hbar^2 T}{M k_B \theta_D^2}\right)\left[\varphi\left(\frac{\theta_D}{T}\right) + \frac{1}{4}\frac{\theta_D}{T}\right] + A, \tag{5.2}$$

where

$$\varphi\left(\frac{\theta_D}{T}\right) = \frac{T}{\theta_D}\int_0^{\theta_D/T}\left[\frac{x}{\exp(x)-1}\right]dx. \tag{5.3}$$

Here $\hbar$ is Dirac constant, M is the mass of the vibrating species in atomic mass units, k_B is Boltzmanns constant, θ_D is the Debye temperature and A is an offset that accounts for any static disorder in the system. In the EXAFS literature [Frenkel and Rehr, 1993], an Einstein model is often fit to the mean square relative displacement (MSRD) of the nearest neighbor peak,

$$\sigma^2 = \hbar^2/2\mu k_B \theta_E \coth\left(\frac{\theta_E}{2T}\right) + \sigma^2_{static}. \tag{5.4}$$

Here, μ is the reduced mass of the pair of atoms contributing to the peak (in this case it is half of the mass of Pt). The second term is an offset serving the same purpose as A in Equation. 5.2, but it will be different since it is the static disorder manifest in the nearest neighbor bond length distribution.

5.3 Results and discussion

5.3.1 PDFs for all samples measured at 80 K

Representative PDFs for different Pt/C samples measured at 80 K are shown in Fig. 5.2. The PDF peaks diminish in amplitude with increasing r due to the finite size effects. For the lower Pt loadings this decrease happens more rapidly indicating their reduced sizes. We adopt the structural model of FCC bulk platinum during PDF fitting using PDFgui and as suggested by the difference plots, the standard FCC model (space group $Fm\overline{3}m$) fits well to the nanoparticle samples. Overall the fits are of high quality suggesting that the structure of these nanoparticles is well explained by the bulk FCC model, although there are larger residuals for the smallest nanoparticles. This difference

may be due to an additional structural component in small nanoparticles such as contamination that becomes more prominent in samples at small sizes and the residual signal of the scattering from the carbon support.

5.3.2 Bond stiffness of Pt nanoparticles

The ADP determined from a fit over wide r-range, and the MSRD of the nearest neighbor peak, were further fit with a Debye (Fig. 5.3(a)) and Einstein model (Fig. 5.3(b)), respectively. The fit results are summarized in Table 5.1. Fig. 5.3(a), (b) show the temperature dependence of the ADPs and MSRDs, respectively, measured from the PDFgui fits for the different sized nanoparticles. As the nanoparticles get smaller the curves in both figures shift to higher values indicating more disorder. They also systematically steepen as is confirmed by the Debye/Einstein model fits that show a monotonic decrease in θ_D and θ_E with decreasing size. The Debye curves and Einstein curves fit well suggesting that these two parameter models are sufficient for fitting the data. The quantitative fitting results are presented in Table 5.1 where we see a monotonic decrease of θ_D and θ_E and an increase in the static offset, with decreasing nanoparticle size.

In bulk materials a decrease in Debye temperature directly implies a softening of the atomic bonding. However, to deduce this in nanoparticles we first have to account for the effects of the surface. The surface atoms have larger thermal motions because they are bonded to fewer neighbors and their motion is less constrained. For example, a Pt atom in the bulk has 12 neighbors and therefore 12 bonds provide a restoring force when the atom displaces. The surface Pt atoms have fewer neighbors and even in the case where the bond-strength of each bond doesnt change from bulk to surface, they will exhibit a lower θ_D. The ADP we measure from the PDF contains contributions from both the surface and bulk atoms. As a rough first approximation we may consider our measured $\theta_D(D)$ to be the properly weighted average of the surface θ_D^S and bulk θ_D^B Debye temperatures,

$$\overline{\theta_D}(D) = \theta_D^B - R_S(\theta_D^B - \theta_D^S), \tag{5.5}$$

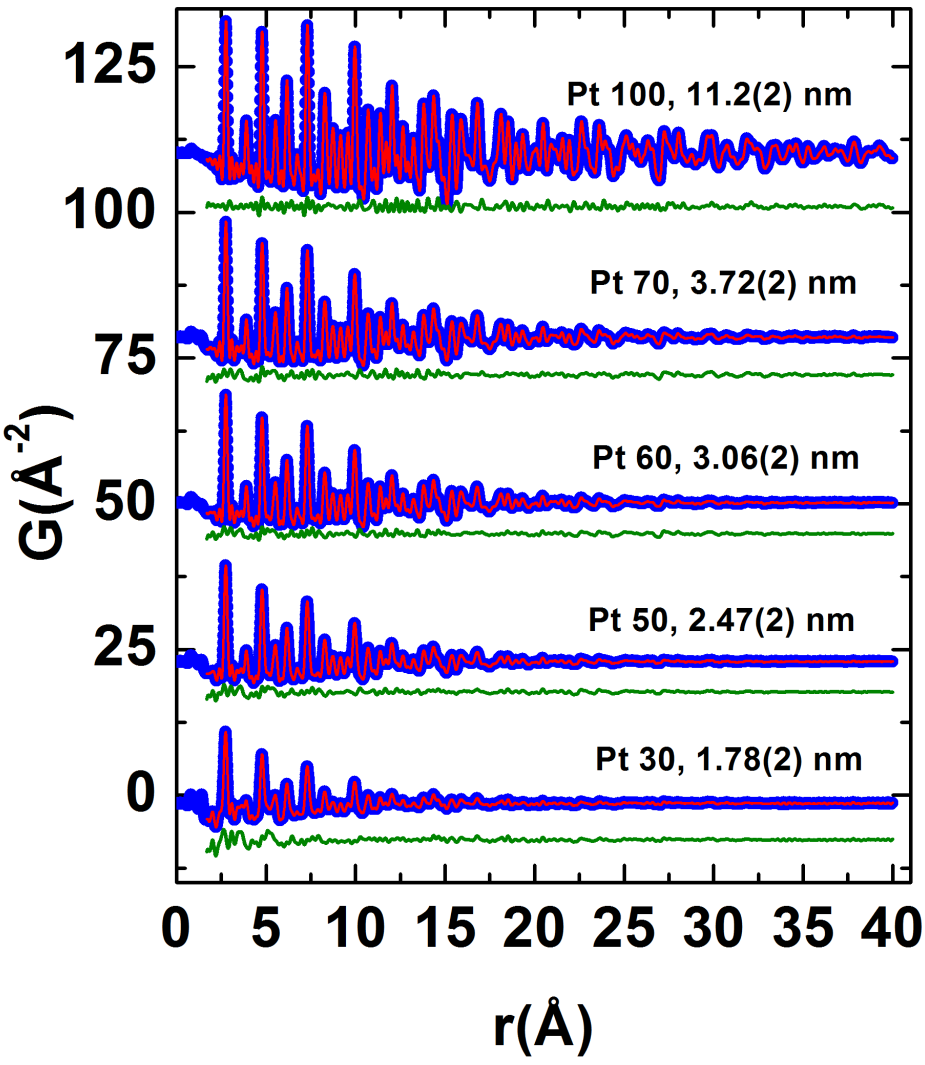

Figure 5.2: Experimental (blue) and corresponding simulated PDFs (red) with difference curve (green) offset below, for all Pt samples measured at 80K. From top to bottom are Pt 100, Pt 70, Pt 60, Pt 50 and Pt 30 respectively.

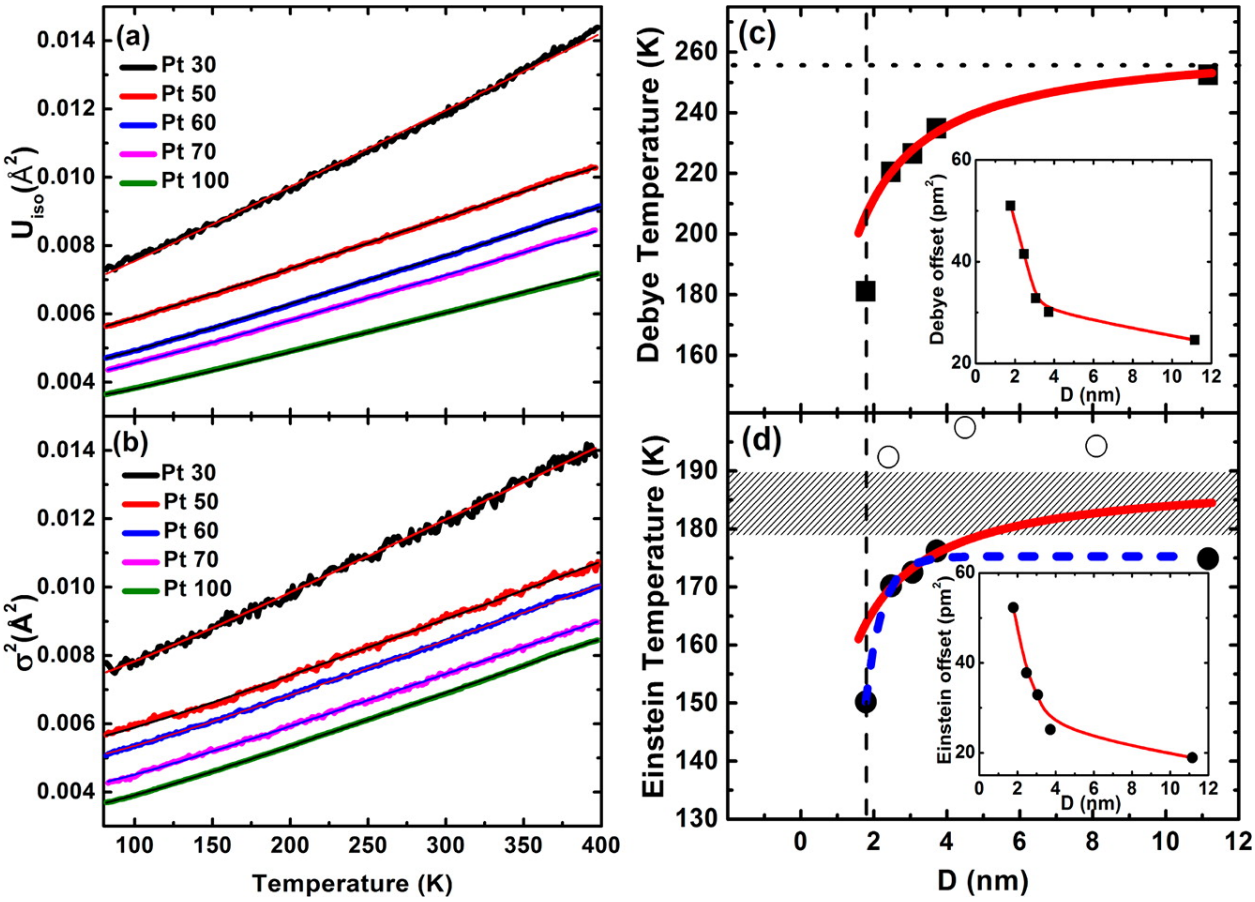

Figure 5.3: (a) ADPs as a function of temperature (symbols) (80 K-400 K) and their fits with Debye model (solid lines). (b) MSRDs as a function of temperature (symbols) and their fits with Einstein model (solid lines). From top to bottom are Pt 30, Pt 50, Pt 60, Pt 70 and Pt 100 respectively. (c) Red solid curve is the fit to the Debye tempertures (black squares) of Pt 50-Pt 100 using Equation 5.2 with fixed θ_D^B= 263.5 K. The horizontal dotted line corresponds to reported bulk θ_D (253 K) [Frenkel *et al.*, 2001]. The vertical dashed line is a guide to the eye. Inset is the static offset from Debye fit as a function of nanoparticle size. (d) Solid red line is the fit to Einstein temperatures (black dots) of Pt 50-Pt 70 with fixed dr=0.521 r_{nn} using Equation 5.4. Blue dashed line is a power law fit to all Einstein temperatures using $\theta_E(D)$ =$\theta_E(\infty)$-cD^x where $\theta_E(\infty)$ =175.5(11) K, c=383(200), x=-4.7(9), R^2=0.9839. The grey shaded area suggests the range of θ_E values of bulk Pt from the literature [Kang *et al.*, 2006; Giulian *et al.*, 2009; Frenkel *et al.*, 2001; Sanchez *et al.*, 2009]. Open circles are reported values of Pt/C from [Frenkel *et al.*, 2001]. The vertical dashed line is a guide to the eye. Inset is the static offset from Einstein fit as a function of nanoparticle size.

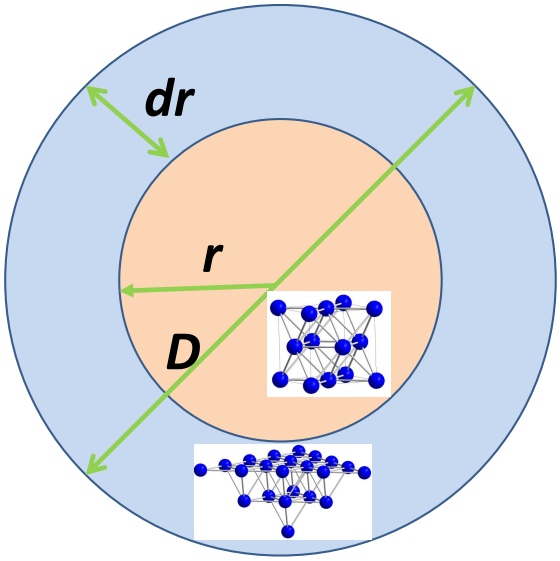

Figure 5.4: An illustration of surface and bulk core-shell in a spherical nanoparticle with D, r, dr the particle diameter, the radius of bulk sphere and the thickness of surface layer, respectively.

where the surface-to-volume ratio, R_S is

$$R_S = 1 - \left(1 - \frac{2dr}{D}\right)^3. \tag{5.6}$$

As illustrated in Fig. 5.4, if we assume the nanoparticles are spherical and the surface atoms are those atoms that reside within an annulus dr of the surface, where dr is some length close to that of a nearest neighbor bond in the material, we can define surface-to-volume ratio R_S as the ratio of the volume of the annulus to the total volume of the nanoparticle,

$$R_S = \frac{[\frac{4}{3}\pi(\frac{D}{2})^3 - \frac{4}{3}\pi(\frac{D}{2} - dr)^3]}{\frac{4}{3}\pi(\frac{D}{2})^3}, = 1 - (1 - \frac{2dr}{D})^3, \tag{5.7}$$

where the nanoparticle diameter $D = 2(r + dr)$. Since we assume that our measured $\theta_D(D)$ are the weighted averages of θ_D^B and θ_D^S , which with this definition of R_S is given by,

$$\overline{\theta_D}(D) = \theta_D^B(1 - R_S) + \theta_D^S R_S. \tag{5.8}$$

By rearranging it we get

$$\overline{\theta_D}(D) = \theta_D^B - R_S(\theta_D^B - \theta_D^S). \tag{5.9}$$

Table 5.1: Values of average nanoparticle diameter D, Debye, θ_D, and Einstein, θ_E, temperatures refined from the fits, and their corresponding static disorder parameters, A and σ^2_{static}, respectively. The numbers in parentheses are the standard deviation on the last digit estimated from the counting statistics but not including other sources of error.

Samples	D (nm)	$\overline{\theta_D}(K)$	Static disorder (Å^2)	$\overline{\theta_E}(K)$	σ^2_{static} (Å^2)
Pt 100	11.2(2)	252.4(2)	0.0024(2)	174.8(3)	0.0018(3)
Pt 70	3.72(2)	234.8(4)	0.0030(03)	176.2(2)	0.0025(2)
Pt 60	3.06(2)	226.5(3)	0.0032(3)	172.5(4)	0.0032(2)
Pt 50	2.47(2)	220.5(2)	0.0041(3)	170.2(3)	0.0037(2)
Pt 30	1.78(2)	181.1(7)	0.0051(2)	150.2(8)	0.0052(3)

The quantity dr is the thickness of the surface annulus and will have a value comparable to the nearest neighbor bond-length, r_{nn}. If we set dr=r_{nn}, we get R_S values for Pt 100 to Pt 30 to be 0.141, 0.382, 0.449, 0.532 and 0.672 respectively. For the smallest nanoparticles, up to 67% of the atoms sit at a surface. However, in reality dr is less than r_{nn} and is not known precisely, depending, for example on the crystallographic facet at the surface. Nonetheless, we can plot $\overline{\theta_D}(D)$ using literature values of θ_D^B=253 K [Frenkel *et al.*, 2001] and θ_D^S=111 K [Lyon and Somorjai, 1966] for bulk and surface Debye temperatures, respectively, for different values of dr=0.5r_{nn}, 0.75r_{nn} and r_{nn} , and the results are shown with the measured $\theta_D(D)$ in Fig. 5.5. Although the calculated $\overline{\theta_D}(D)$ show a similar decreasing trend as the experimental Debye temperatures do, none of them match the data, suggesting the reported θ_D^B and θ_D^S need to be adjusted for our case.

We also tried fitting the measured $\theta_D(D)$ with θ_D^B and θ_D^B as variables in Equation 5.5. Since dr is not known accurately we tried this for various dr values from 0.25 r_{nn} to r_{nn} with an interval of 0.25 r_{nn} (if we let dr also vary, the refinements are unstable). The curve could fit the measured $\theta_D(D)$ of the largest four nanoparticles for all dr values, but would not fit the θ_D value of the smallest nanoparticle for any dr: the Pt 30 point is always offset significantly below the fit curves. Since Equation 5.5 is derived for the case of fixed bond-stiffness, the suppression of θ_D for Pt 30 is

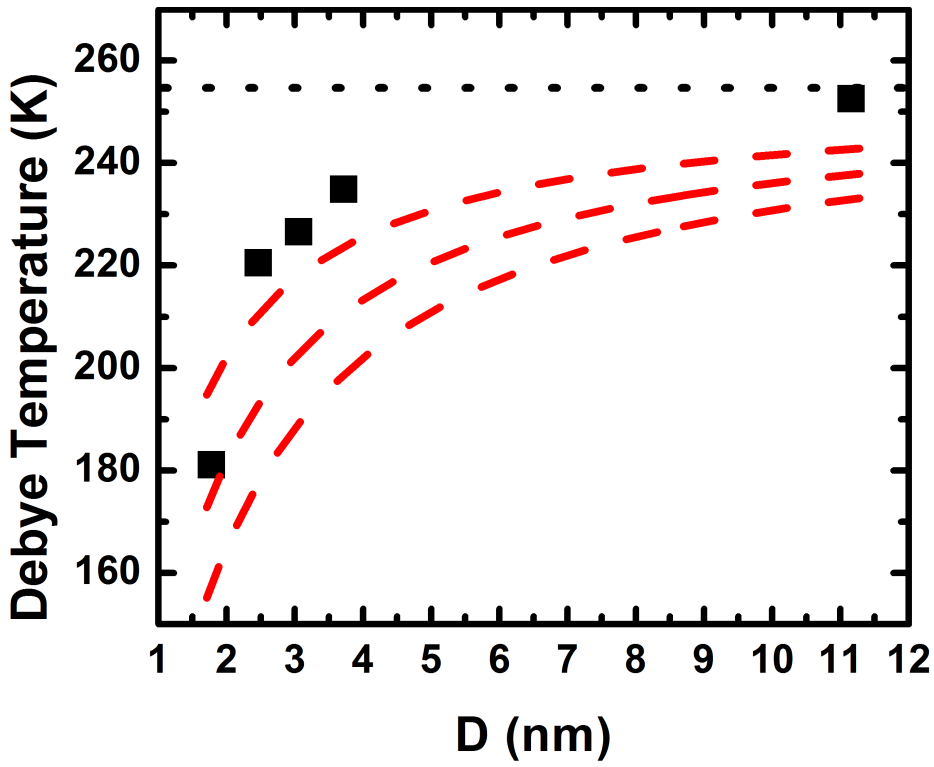

Figure 5.5: Dashed lines are the calculated Debye temperatures from Equation 5.5 using θ_D^B=253 K [Frenkel *et al.*, 2001] and θ_D^S=111 K[Lyon and Somorjai, 1966] for different surface layer thickness dr. From top to bottom are dr=0.5r_{nn}, 0.75r_{nn} and r_{nn} (r_{nn} is the nearest neighbor distance). The horizontal dotted line corresponds to reported bulk θ_D^B=253 K [Frenkel *et al.*, 2001]. Solid square symbols are measured Debye temperatures.

consistent with the bonding being softer in this smallest nanoparticle.

For all dr we obtained a stable θ_D^B around 263.5 K giving us confidence that in the current measurements θ_D^B is 263.5 K. Fixing this parameter and using Equation 5.5 we obtained a good fit (Fig. 5.3(c)) to the four larger nanoparticles yielding physically reasonable values of $\theta_D^B = 124.1(4)$ K and an average $dr = 0.521\ r_{nn}$. However, if the fit includes the smallest Pt 30, the results do not yield physical values. The D dependence of $\theta_D(D)$ for the larger nanoparticles can be well explained due to surface effects and not a change in bond-stiffness. However, the large suppression ($\sim$25 K) of Pt 30 from the fit curve indicates an anomalous bond softening for the 1.78(2) nm nanoparticle. Exactly at which diameter the softening sets in could be tested more accurately if we had more size-controlled samples with different diameters in this region.

The effect is even more apparent in the measurements of the MSRD of the nearest-neighbor bond. The width of this PDF peak gives the relative amplitude of motion of directly bonded pairs of atoms and should be a rather direct measure of the bonding stiffness and less sensitive to static disorder. Similar to the Debye model case, we can define a size dependent $\overline{\theta_E}(D)$ using

$$\overline{\theta_E}(D) = \theta_E^B - R_S(\theta_E^B - \theta_E^S). \tag{5.10}$$

This relationship is shown, with a fixed $dr = 0.521\ r_{nn}$ and values of θ_E^B and θ_E^S obtained by fitting to the measured $\theta_E(D)$ of the Pt 50, Pt 60 and Pt 70 nanoparticles, as the red solid curve in Fig. 5.3(d). It was not possible to get a good fit that included either of the end-members. The curve extends to the shaded area in the figure which indicates the range of θ_E^B in the literature [Kang *et al.*, 2006; Giulian *et al.*, 2009; Frenkel *et al.*, 2001; Sanchez *et al.*, 2009], although it is significantly higher than the θ_E measured from our data. As with the Debye temperature fits, there is a dramatic drop in $\theta_E(D)$ for the smallest nanoparticle. In order to fit the measured θ_E for both the smallest and largest nanoparticles in our sample we carried out an empirical power law fit, shown as the blue dashed line in Fig. 5.3(d), resulting in a a power of $\sim$-4.7(9). This suggests there is a large deviation of θ_E from Equation 5.10 for Pt 30 again consistent with a bond softening in the smallest nanoparticle.

As shown in the insets of Fig. 5.3(c) and Fig. 5.3(d), the static offsets from both the Debye and Einstein fits increase strongly with reduced nanoparticle sizes indicating significantly larger bond-length distributions in smaller nanoparticles. In particular, for the smallest nanoparticle below 2 nm diameter, there is considerable non-thermal contributions to the bond-length distribution.

5.4 Conclusion

In this chapter a reasonable protocol based on the PDFgui program was presented to extract size dependent Debye/Einstein temperatures of carbon supported platinum nanoparticles. The surface effect of the nanoparticles was corrected, as a first approximation, by considering surface-to-volume ratio weighted Debye temperatures. We find evidence for a significant bond softening, and an increase in non-thermal disorder, only for the smallest nanoparticle below 2 nm in diameter. More work is needed to confirm definitely that this effect comes from a bond softening and not some other overlooked effect such as a decrease in surface-atom coordination or an effect related to sample composition or chemistry. Thermodynamic properties of nanoparticles are difficult to measure directly and theoretical works based on either molecular dynamics or first principle calculations are needed for a better understanding. However, as shown in this chapter the PDF technique contains a wealth of information about very small nanoparticles that opens the door to the validation of such studies.

Chapter 6

Lattice dynamics of CdSe bulk and nanoclusters

In this chapter, the lattice dynamics of bulk CdSe and three quantized growth "magic size" CdSe nanoclusters is reported. When studying the lattice dynamics of bulk CdSe, a variety of experimental and theoretical techniques were compared. These include inelastic x-ray scattering (IXS), inelastic neutron scattering (INS), empirical force fields (FF) and density functional theory (DFT). We found that the DFT results are consistent with those of the experimental IXS and INS, while force field models only very approximately reproduce the experimental observations. When we turned to the study of the lattice dynamics of the nanoparticles, we therefore focussed on DFT and IXS. As discussed in Chapter 1.3, INS is not suitable for the cluster samples due to incoherent scattering signals from hydrogen-containing ligands that were used to stabilize the CdSe clusters as well as the large quantities of samples required for neutron experiment.

6.1 Lattice dynamics of bulk CdSe

6.1.1 Introduction

Lattice dynamics governs various thermodynamic properties of materials. To study it, on the experimental side, inelastic neutron scattering (INS) is often the tool of choice. In addition, the high energy resolution inelastic x-ray scattering (HERIX) technique [Chaplot *et al.*, 2010; Dove, 2003; Cardona and Merlin, 2007; Burkel, 2003] developed recently has been also contributing to the ever-increasing numbers of lattice dynamical studies [Budai *et al.*, 2014; Lin *et al.*, 2014b; Gretarsson *et al.*, 2013; Scopigno *et al.*, 2011]. Moreover, the amplitudes of atomic vibrations can also be readily studied by x-ray/neutron crystallography. A temperature dependent scattering experiment allows, in principle, a separation of the contributions to the atomic displacement parameters (ADPs) from thermal and static disorder effects. The scattering pattern is fit with a structure model at each temperature point [Abeykoon *et al.*, 2013; Shi *et al.*, 2013; Wood *et al.*, 2002; Lane *et al.*, 2012]. After fitting the ADP curves with either a Debye model [Debye, 1912] or an Einstein model [Einstein, 1911], the resulting Debye/Einstein temperatures reveal information on the strength of the atomic bonding [Shi *et al.*, 2013; Gilbert *et al.*, 2004; Kang *et al.*, 2006]. Raman spectroscopy is also a quick and efficient experimental laboratory tool that probes the frequency of certain optical phonon modes at thye Brillouin zone center [Chaplot *et al.*, 2010; Dove, 2003]. On the theoretical side, lattice dynamics has been extensively studied by empirical interatomic force field (FF) molecular modeling [Rabani, 2002; Zhou *et al.*, 2013; Benkabou *et al.*, 2000; Lin *et al.*, 2014a; Han and Bester, 2011] or more accurately by *ab initio* density functional theory (DFT) [Stoffel *et al.*, 2010; Corso *et al.*, 1993; Kootstra *et al.*, 2000; Mohr and Thomsen, 2009; Sarasamak *et al.*, 2010; Han and Bester, 2012a; Han and Bester, 2012b]. The phonon eigenfrequencies can be calculated by constructing and diagonalizing the dynamic matrix which is the Fourier transform of force constant matrix (details see Chapter 1.3).

However, despite all these existing tools, to the best of our knowledge, there lacks a thorough test on the accuracy from these methods in the literature for the semiconductors of interest to us.

We want to use these methods to study the lattice dynamics of the "magic size" nanoparticles that we have available from the Owen group[Beecher *et al.*, 2014], but to ensure that we understand the intrinsic accuracy of the different methods we take the initiative to study the lattice dynamics of bulk CdSe using the various lattice dynamics methods. The lattice dynamics of CdSe is relatively well documented in the literature [Rabani, 2002; Zhou *et al.*, 2013; Benkabou *et al.*, 2000; Lin *et al.*, 2014a; Corso *et al.*, 1993; Kootstra *et al.*, 2000; Mohr and Thomsen, 2009; Sarasamak *et al.*, 2010; Schowalter *et al.*, 2009; Widulle *et al.*, 1999; Cline *et al.*, 1967; Bonello and Fernandez, 1993].

To validate various experimental and theoretical tools for studying lattice dynamics, we proposed to test simulated phonon dispersion curve and phonon density of states (PDOS) from force fields and DFT against those from experiments, i.e. IXS for PDOS and INS for the dispersion curves. Three sets of interatomic potentials for CdSe, namely, Rabani [Rabani, 2002], Tersoff [Benkabou *et al.*, 2000] and Stillinger-Weber potentials from Zhou *et al*. [Zhou *et al.*, 2013] were tested.

6.1.2 Experiments and Methods

Our collaborator at Chemistry Department at Columbia University, Alexander Beecher from Prof. Jonathan Owen group prepared the bulk CdSe and nanocluster samples for the lattice dynamics studies. Dr. Yan Li from Brookhaven National Laboratory carried out density functional theory calculation. Drs. Ayman Said and Bogdan Leu from Argonne National Laboratory helped us with the HERIX experiment.

6.1.2.1 Inelastic x-ray scattering experiment

The high energy resolution inelastic x-ray scattering experiments were carried out at room temperature (RT) at Sector 30 at Argonne National Laboratory. The CdSe bulk and nanocluster powder samples were encapsulated in kapton capillary tubes. By scanning x, y positions along the tubes, the optimum one absorption length was achieved for each sample as described in Chapter 2.3.3. The unfocussed incident x-ray with an energy of 23.7245 keV (λ=0.5226 Å) with a beam size of 2.4×0.4 mm

was incident on the samples and eight spherical analyzers recorded the data simultaneously in a momentum transfer range from 54.89 nm^{-1} to 70.57 nm^{-1} (corresponding to a 2θ-range from 26.51° to 33.98°). The energy transfer was chosen from -10 meV to +40 meV. Each sample was measured for 50 minutes and repeated for at least 10 times before summation. A Poly(methyl methacrylate) or PMMA rod was also measured at RT at 10 nm^{-1} to determine the resolution function and efficiency of each analyzer. An empty capillary was also measured for background subtraction. The measured IXS spectra were summed into one spectrum using an "incoherent approximation" where intensity measured by each individual analyzer was divided by the respecive analyzer efficiency before summation. Further data treatment including deconvolution from resolution function and subtraction of multiphonon scattering signal closely follows the literatures [Kohn and Chumakov, 2000; Bosak and Krisch, 2005] and is described in more detail in Chapter 2.3.4.

6.1.2.2 Empirical force fields for CdSe

In the current study we tested three sets of FFs for investigating the lattice dynamics of bulk CdSe. They are Rabani [Rabani, 2002], Tersoff [Benkabou *et al.*, 2000] and Stillinger-Weber potentials using parameters reported in [Zhou *et al.*, 2013]. The Rabani potential has contributions from both Coulomb and Lennard-Jones interactions and its analytical form is described as

$$V_{Rabani} = \sum_i \sum_{j>i} \frac{q_i q_j}{r_{ij}} + 4\varepsilon_{ij} \left\{ \left(\frac{\sigma_{ij}}{r_{ij}} \right)^{12} - \left(\frac{\sigma_{ij}}{r_{ij}} \right)^{6} \right\}. \tag{6.1}$$

The Tersoff potential has the form

$$V_{Tersoff} = \sum_i \sum_{j>i} f_c(r_{ij}) \left[A \exp(-\lambda_1 r_{ij}) - B b_{ij} \exp(-\lambda_2 r_{ij}) \right], \tag{6.2}$$

where

$$f_c(r_{ij}) = \begin{cases} 1, & r < R - D, \\ \frac{1}{2} - \frac{1}{2} \sin\left[\frac{\pi}{2} \frac{r-R}{D} \right] & R - D < r < R + D \\ 0, & r > R + D \end{cases} \tag{6.3}$$

Table 6.1: Parameterization of the Rabani potential.

parameters[1]	q	σ (Å)	ε (meV)
Cd	1.18	1.98	1.4427
Se	-1.18	5.24	1.2840

[1] $\varepsilon_{ij} = (\varepsilon_i \varepsilon_j)^{1/2}$ and $\sigma_{ij} = (\sigma_i + \sigma_j)/2$

and

$$b_{ij} = \left(1 + \beta^n \xi_{ij}^n\right)^{-1/(2n)}, \tag{6.4}$$

$$\xi_{ij} = \sum_{k \neq i,j} f_c(r_{ij}) g(\theta_{ijk}), \tag{6.5}$$

and

$$g(\theta) = 1 + \frac{c^2}{d^2} - \frac{c^2}{d^2 + (h - \cos\theta)^2}. \tag{6.6}$$

The Stillinger-Weber potential takes the form

$$V_2(i,j) = \begin{cases} A\left(\frac{B}{r_{ij}^4} - 1\right) \exp\left(\frac{\rho}{r_{ij} - r_{max}}\right), & r_{ij} < r_{max}, \\ 0, & r_{ij} \geq r_{max}, \end{cases} \tag{6.7}$$

$$V_3(i,j,k) = h(r_{ij}, r_{ik}) + h(r_{ji}, r_{jk}) + h(r_{ki}, r_{kj}) \tag{6.8}$$

where

$$h(r_{ij}, r_{ik}) = \lambda \exp\left(\frac{\eta}{r_{ij} - b} + \frac{\eta}{r_{ik} - b}\right)\left(\cos\theta_{jik} + \frac{1}{3}\right)^2 \tag{6.9}$$

The parameters for these three force fields are summarized in Table 6.1, Table 6.2 and Table 6.3, for Rabani, Tersoff and Stillinger-Weber, respectively.

The lattice parameters, elastic constants and phonon calculations (dispersion curves and density of states) were calculated from these potentials and parameters using the General Utility Lattice Program (GULP) program (version 4.0.3) [Gale, 1997; Gale and Rohl, 2003]. For phonon calculations we used a 60×60×60 k-grid for the Brillouin zone integration.

Table 6.2: Parameterization of the Tersoff potential.

parameters	value
A (eV)	5229
B (eV)	252.5
λ_1 (Å^{-1})	3.1299
λ_2 (Å^{-1})	1.7322
β	1.5724×10^{-6}
n	0.78734
c	100390
d	16.217
h	-0.57058
R (Å)	3.175
D (Å)	0.15

Table 6.3: Parameterization of the Stillinger-Weber potential.

Two-body potentials	A (eV)	ρ (Å)	B (Å^4)	r_{min} (Å)	r_{max} (Å)	-	-
Cd-Se	9.5337	2.0452	19.5270	0.0000	3.9950	-	-
Cd-Cd	9.3607	2.6640	38.6503	0.0000	4.0704	-	-
Se-Se	19.0070	2.7890	46.4206	0.0000	4.3088	-	-
Three-body potentials	k (eV)	θ_0 (°)	ρ_1 (Å)	ρ_2 (Å)	r_{ijmax} (Å)	r_{jkmax} (Å)	r_{ikmax} (Å)
Cd-Se-Se	58.5609	109.4712	2.4542	3.3468	3.9950	3.9950	4.3088
Se-Cd-Cd	41.0966	109.4712	2.4542	3.1967	3.9950	3.9950	4.0704

6.1.2.3 Density functional theory

Density functional theory (DFT) calculations within the local density approximations (LDA) and generalized gradient approximations (GGA) were carried out by Dr. Yan Li at Brookhaven National Laboratory with the projected augmented wave method [Blöchl, 1994] implemented in the Vienna *ab initio* simulation package (VASP) [Kresse and Furthmuller, 1996] package. The lattice parameters and elastic moduli of the primitive unit cells of bulk CdSe were optimized using a kinetic energy cutoff of 520 eV, and the first Brillouin zone were sampled using a $8 \times 8 \times 6$ k-grid for the wurtzite structure. The dynamical matrix was computed via the density functional perturbation theory [Baroni *et al.*, 2001] with a $2 \times 2 \times 2$ supercell and correspondingly reduced q-grid. Phonon dispersion and projected phonon density of states were analyzed using the PHONOPY program [Togo *et al.*, 2008]. Nonanalytic corrections were applied to the dynamical matrix by using the Born effective charge Z^* and dielectric constants ϵ_∞.

As shown in Table 6.4, the computed values of ϵ_∞ are overestimated compared to experiments [Manabe *et al.*, 1967; Madelung *et al.*, 1982] and other *ab inito* calculations [Corso *et al.*, 1993; Kootstra *et al.*, 2000], most likely due to the underestimated band gap from the LDA approximation. We have confirmed that applying a smaller ϵ_∞, i.e. replacing ϵ_∞ with $\epsilon_\infty^{\text{exp}} = 6$ shifts up the TO(Γ) branch and leads to an increase of less than 10 cm^{-1} at $q = \Gamma$ for both ZB and WZ structures whereas other branches are not affected.

Table 6.4: Computed dielectric constants and Born effective charge.

Method	ZB		WZ	
	ϵ_∞	Z^*	$\epsilon_{\infty,z}$	Z_3^*
LDA (this work)	8.3	2.2	7.7	2.2
	6.2[1],7.9[2],9.1[3]		7.2[4]	
PBE (this work)	7.9	2.3	7.5	2.3
	8.6[3]			
Exp.	5.8[5], 6.2[6]			

[1] [Corso *et al.*, 1993]

[2] [Bouamama *et al.*, 2009]

[3] [Schowalter *et al.*, 2009]

[4] [Mohr and Thomsen, 2009]

[5] [Manabe *et al.*, 1967]

[6] [Madelung *et al.*, 1982]

6.1.3 Lattice parameters and elastic properties

The computed lattice parameters and bulk modulus are summarized in Table 6.5, showing excellent agreement with experimental values as well as previous DFT calculations.

Table 6.5: Computed lattice parameters and bulk modulus for bulk CdSe in comparison with experiments and other calculations.

Method		a (Å)	c/a	B (GPa)
DFT	LDA	4.26	1.63	57.5
		4.29[1],4.28[2]	1.63[1,2]	55.6[1],60[2]
	GGA	4.39	1.63	44.5
FF	Rabani	4.38 (4.28)	1.63	44.9
	S-W	4.28	1.63	53.5
	Tersoff	4.26	1.63	57.8
Exp.		4.30[3]	1.63[3]	53.4[4]

[1] [Mohr and Thomsen, 2009]

[2] [Sarasamak *et al.*, 2010]

[3] [Widulle *et al.*, 1999]

[4] [Bonello and Fernandez, 1993]

Computed elastic parameters c_{ij} are listed in Table 6.6, and the Debye temperature was estimated from the average sound velocity v_m as [Anderson, 1963]:

$$\Theta_D = \frac{\hbar}{k}\left[\frac{3n}{4\pi}\left(\frac{N_A\rho}{M}\right)\right]^{\frac{1}{3}} v_m \tag{6.10}$$

$$v_m = \left[\frac{1}{3}\left(\frac{2}{v_s^3}+\frac{1}{v_l^3}\right)\right]^{-\frac{1}{3}} \tag{6.11}$$

where n and M are the number of atoms and the molecular mass per formula unit, respectively. v_s and v_l are the shear and longitudinal sound velocities, which can be derived from the elastic constants by assuming the Voigt and Reuss approximations [Anderson, 1963]. The computed $\Theta_D = 192$ K is in reasonable agreement with experimental value of 181 K for the wurtzite structure

[Cline *et al.*, 1967].

Table 6.6: Computed elastic constants c_{ij} and Debye temperature Θ_D (K) of bulk CdSe.

	Method	c_{11}	c_{12}	c_{13}	c_{33}	c_{44}	c_{66}	Θ_D[1]
DFT	LDA	80.0	49.9	42.6	91.0	16.0	15.0	187
	Ref. [Sarasamak *et al.*, 2010]	80	47	40	92	15	17	192
	GGA (this work)	65.3	37.2	30.6	73.6	14.0	14.0	182
FF	Rabani [Rabani, 2002]	90.7	30.4	13.3	122.0	15.8	30.2	234
	Rabani	65.9	38.0	32.9	64.4	15.2	14.0	180
	SW	71.1	46.3	43.2	74.1	11.1	12.4	163
	Tersoff	71.2	52.9	49.2	74.9	8.2	9.1	142
	Exp. [Cline *et al.*, 1967](RT)	74.9	46.1	39.4	81.7	13.0	14.4	179

[1] [Corso *et al.*, 1993] Computed from c_{ij} via Equations (6.10) and (6.11).

6.1.4 Phonon calculation

To test the robustness of the different models, the simulated phonon dispersion curves for bulk CdSe along Γ-A direction from FFs and DFT were compared with experimental inelastic neutron scattering (INS) results [Widulle *et al.*, 1999] which is shown in Fig. 6.1. In the experimental dispersion curves, there are four backfolded phonon branches. From high to low energy they correspond to longitudinal optical (LO), transverse optical (TO), longitudinal acoustic (LA) and transverse acoustic (TA) branches, respectively. The TO splitting is very small (∼0.07 THz). When comparing with the INS result, the dispersion curves simulated from the FFs are in relatively good agreement with the acoustic phonon branches. As for the optical phonons, Stillinger-Weber and Tersoff potentials significantly overestimate both LO and TO branches whereas the Rabani potential

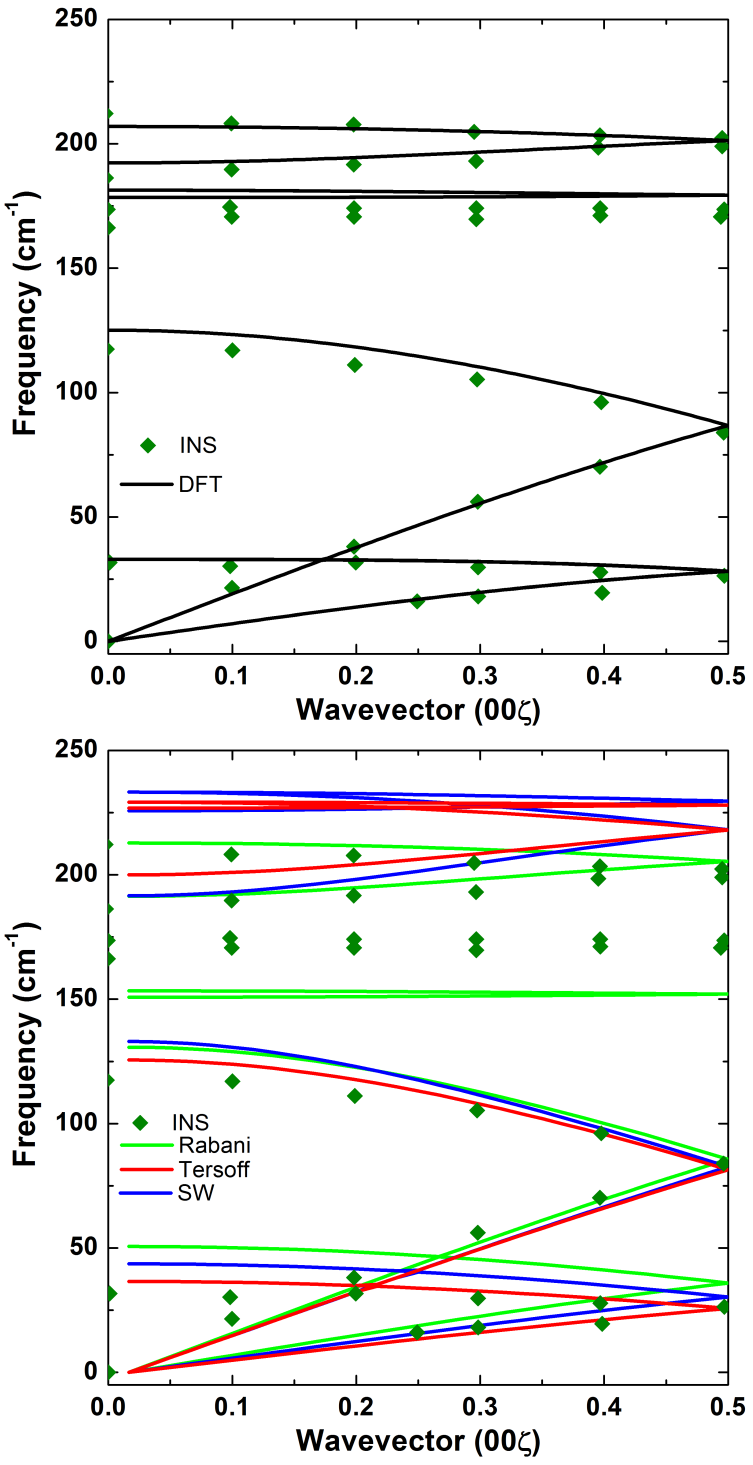

Figure 6.1: Simulated phonon dispersion curves for bulk CdSe along Γ-A direction. (top) A comparison between experimental INS (green symbols)and DFT (black solid curves) (bottom) INS results compared with FFs: Rabani in green, S-W in blue and Tersoff in red. The experimental dispersion is scaled by $\sqrt{\frac{116}{112.4}}$ to account for the use of ^{116}Cd isotope instead of the natural Cd with an atomic weight of 112.4.

overestimates the LO branch but undervalues the TO branch. Of all three sets of empirical FFs, only the Rabani potential reproduces the extremely backfolded TO branch as seen in the INS experiment. In contrast to the FFs calculations, the DFT results (indicated as the black solid curves in Fig. 6.1(top)) are in best agreement with the INS experiment. The LA, TA and LO branches overlap well with those from the INS and the splitting of the TO branch is reproduced, although the DFT curve has ~ 10 cm^{-1} higher phonon energy.

Next we compare the simulated PDOS from the FFs, DFT and experimental one from IXS, which is displayed in Fig. 6.2. The theoretically derived PDOS curves can be well understood from a consideration of the dispersion curves shown in Fig. 6.1, with large densities of states corresponding to the flat regions in the dispersion curves corresponding to the zone edge and back-folded acoustic modes, and the higher frequency optical modes. In agreement with the analysis of the dispersion curves, there is comparable agreement in the region below a frequency of 75 cm^{-1} (except for the Rabani potential) but the different FF models do not reproduce the high PDOS in the region of the optic modes. However, when we compare measured PDOS from IXS, we see that it is in excellent agreement with the DFT calculation. Since we have established that the DFT calculation does a good job of explaining the single crystal INS measurement from the literature, it gives us some confidence that our IXS measurement, and the data reduction steps to generate the PDOS, are resulting in an accurate measurement of this quantity

6.2 Lattice dynamics of size dependent quantized grown CdSe nanoclusters

6.2.1 Introduction

As discussed in length in Chapter 1.3, lattice dynamics of low-dimensional materials is extremely difficult to study both experimentally and theoretically. However, HERIX technique is a good candidate for probing phonons in nanoscaled materials. Another approach for obtaining lattice

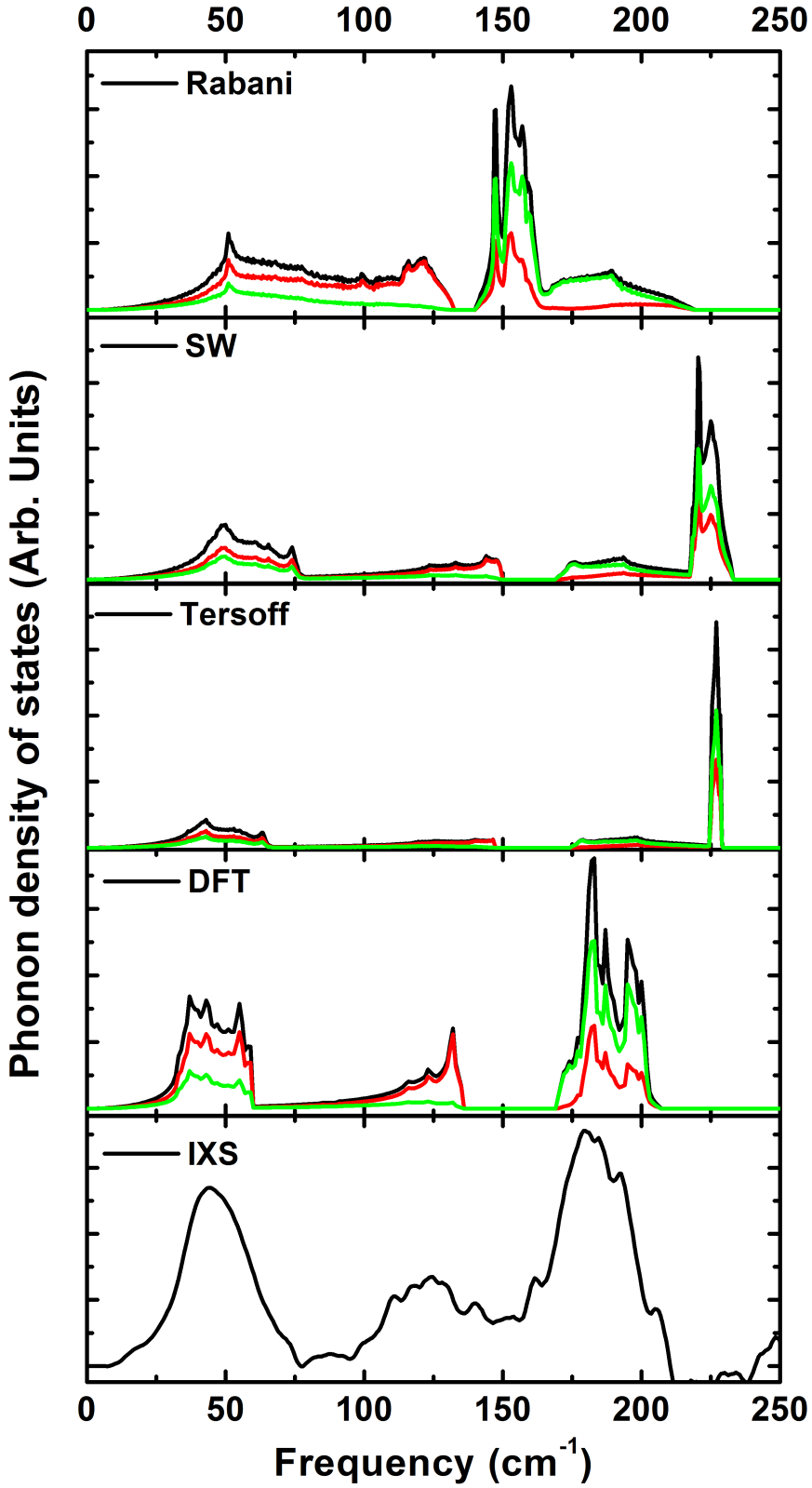

Figure 6.2: PDOS curves for bulk CdSe: from top to bottom are the calculated curves using Rabani potential, Tersoff potential, Stillinger-Weber potential, DFT and the experimental curve

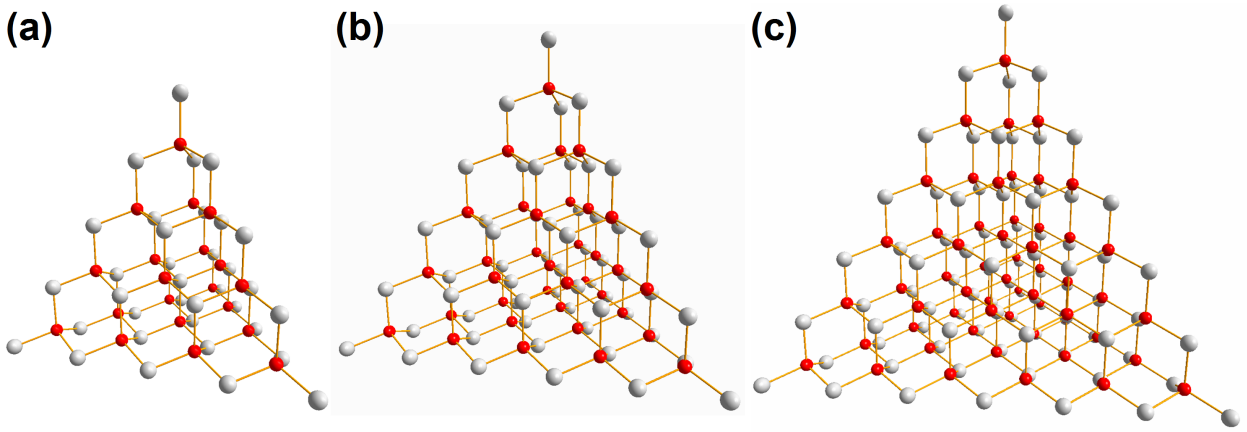

Figure 6.3: The polyhedral representation of three CdSe clusters. (a)-(c) are $CdSe_{(350nm)}$, $CdSe_{(380nm)}$, $CdSe_{(408nm)}$, respectively. Cd in white, Se in red.

dynamical information from nanomaterials is from the temperature dependent atomic pair distribution function (tdPDF) such that one obtains vibrational amplitude of atoms which in turn reveals relevant information on atomic bonding strength in nanostructured materials [Shi *et al.*, 2013]. Here we take the initiative to collect tdPDF data and map out phonon density of states on three sub-2 nm quantized grown CdSe quantum dot clusters [Beecher *et al.*, 2014]. These clusters were monodisperse with pyramidal nanostuctures with cadmium terminated {111} facets (Fig. 6.3). They are named as $CdSe_{(350nm)}$, $CdSe_{(380nm)}$, $CdSe_{(408nm)}$, respectively, for small, medium, large sized clusters where the numbers come from the first electronic transition peak seen in a UV absorption spectrum. Our combined tdPDF and HERIX results suggest that the clusters are disordered and the bonds become stiffer, on average, with decreased sizes, in contrast to the observation of larger ADPs in PDF spectra.

6.2.2 Experiment

Synchrotron X-ray total scattering experiments were conducted at beamline X17A at the National Synchrotron Light Source (NSLS) at Brookhaven National Laboratory. The incident x-ray had an energy of 67.4194 keV (λ=0.1839 Å). The sample-to-detector distance was 212.641 mm for

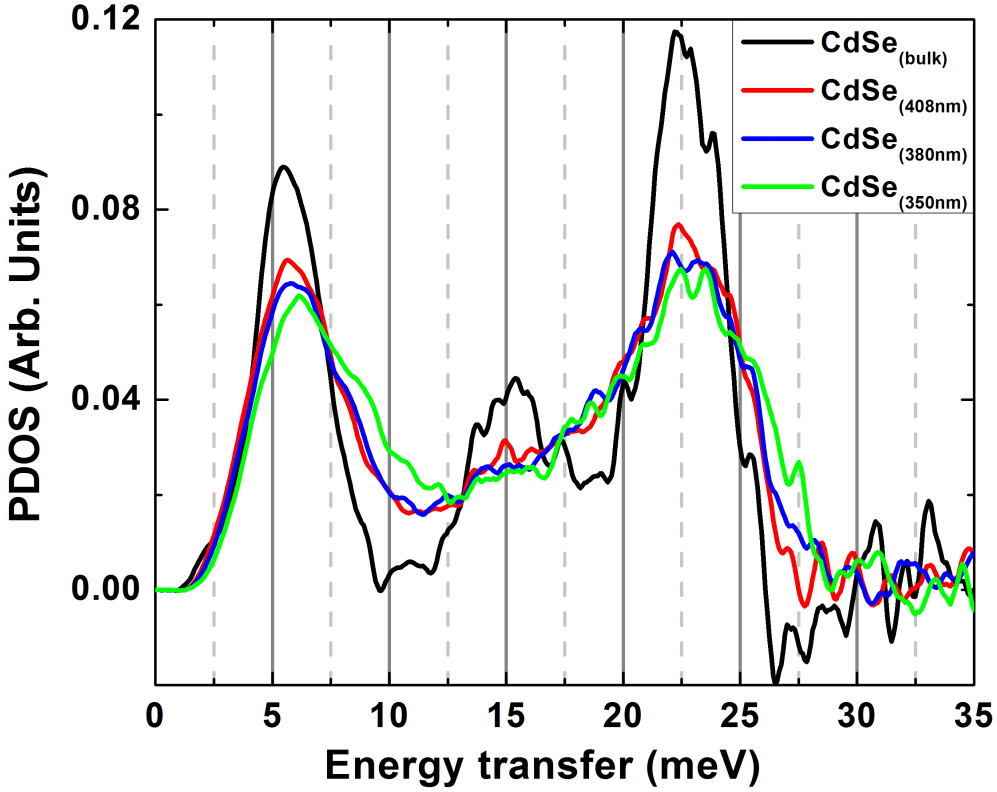

Figure 6.4: The normalized PDOS of CdSe bulk and nanocluster samples from IXS experiment.

$CdSe_{(350nm)}$, $CdSe_{(380nm)}$ and bulk samples while 206.377 mm for $CdSe_{(408nm)}$. Nickel was also measured as a standard material to calibrate the sample-detector distance and to determine the Q_{damp} and Q_{broad} parameters. The refined values are $Q_{damp} = 0.0438$ Å^{-1} and $Q_{broad} = 0.0203$ Å^{-1} for $CdSe_{(408nm)}$ while $Q_{damp} = 0.0416$ Å^{-1} and $Q_{broad} = 0.0196$ Å^{-1} for the rest samples. These values are then fixed in the subsequent model fits. The PDFs of clusters were simulated using a Debye function analysis. Our home-written Diffpy-CMI program [Juhs *et al.*, 2015] has this functionality. The details of HERIX experiment have been described in bulk CdSe section.

6.2.3 Results and discussion

The experimental phonon density of states of CdSe nanoclusters together with bulk reference are shown in Fig. 6.4. The PDOS of the nanoclusters are similar to each other, and share characteristics

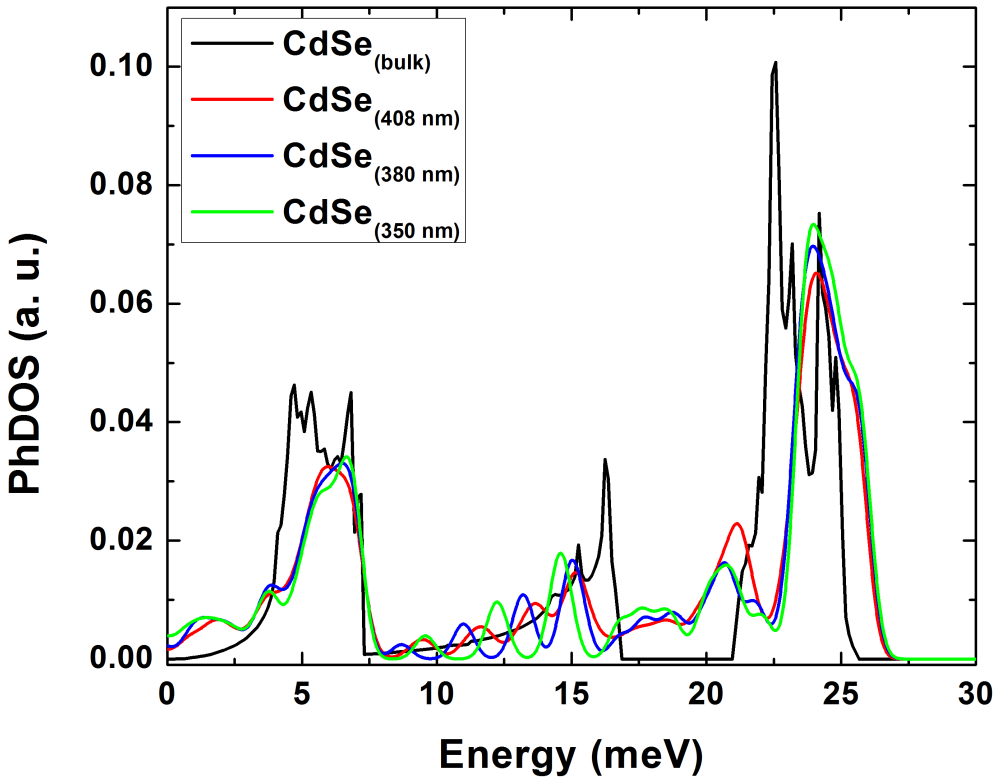

Figure 6.5: The simulated PDOS for CdSe clusters using DFT. A smearing function with $\sigma = 3\ cm^{-1}$ was applied to the curves.

of the bulk PDOS, but are different from that of bulk counterpart in important details. In the PDOS of the cluster samples, the peaks are broadened and the valleys are less deep, where the center longitudinal acoustic peak at ∼15 meV in bulk CdSe is suppressed in all clusters. In addition, there is an overall blue shift with reduced size which can be clearly seen in the shift of the PDOS peak at $\sim$ 6 meV to higher frequencies. The same trend can be also seen in the energy range of $9 \sim 13$ meV and $26 \sim 28$ meV where the cluster phonon modes tend to fill in the gap.

The simulated PDOS curves using DFT are shown in Fig. 6.5. The cluster DOS curves have lower intensities at both acoustic and optical phonon regions which is similar to measured ones. Also when compared with bulk DOS curve, there are a series of sharp discrete peaks in clusters (best seen in the 10 meV to 15 meV region) which is due to finite number of vibration modes in the clusters. Arguably we may see the same features in measured DOS although the poor experimental energy

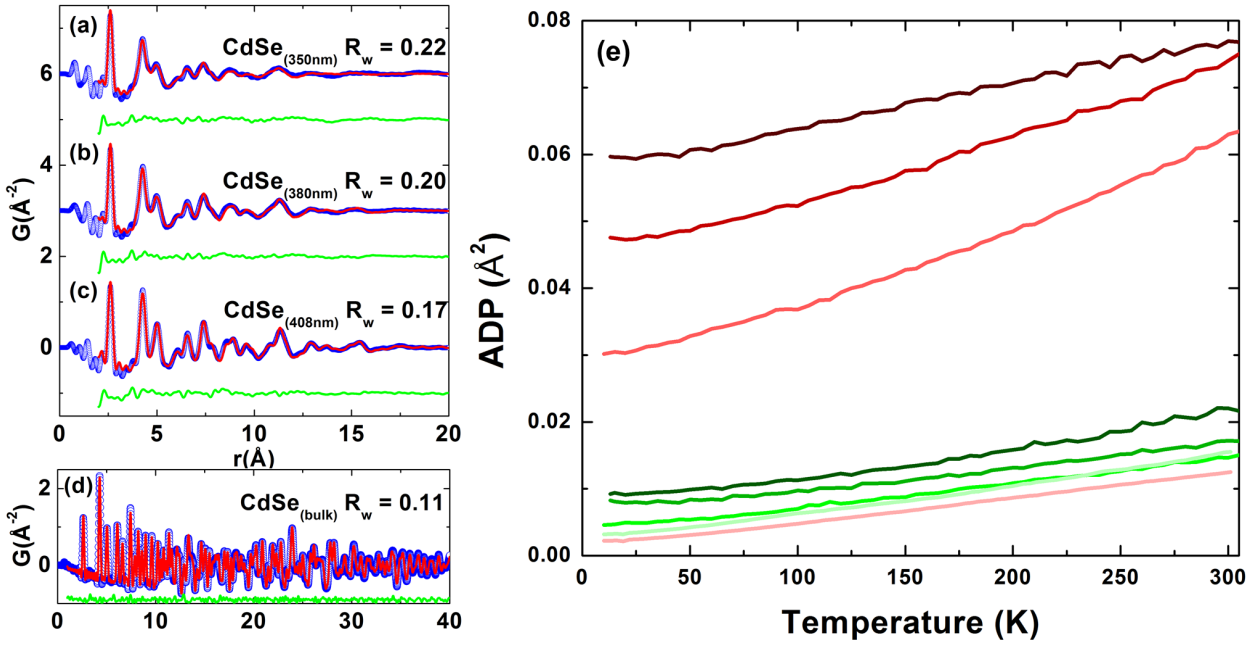

Figure 6.6: (a-d) PDF fits of clusters and bulk. The experimental PDFs, simulated PDFs are in blue circles and red solid lines, respectively, with green difference curve offset below. (e) The ADPs extracted from PDF modelling. The Cd and Se are in red and green colors where darker color corresponds to smaller cluster size.

resolution (compared with DFT) make them less pronounced. Consistent with the experimental results, an overall blue-shift of PDOS curves with reduced sizes are seen in simulated curves.

The temperature dependent PDF measurements were performed on all bulk and cluster samples from 10 K to 300 K. The PDF fits at base temperature 10 K using a tetrahedral structural model and the resulting atomic displacement parameters (ADP) are displayed in Fig. 6.6. The simulated PDFs well capture the main structural features in the measured PDFs. The agreement factors R_w for the PDF fits are ~20% for clusters which are reasonably good for low dimensional materials with size below 2 nm [Shi *et al.*, 2013; Yang *et al.*, 2013; Masadeh *et al.*, 2007; Shi *et al.*, 2014; Farrow *et al.*, 2013] indicating a good structural model. We also notice that the R_w values increase with deceasing cluster size. Since in the PDF modelling we adopt a tetrahedral structural model cut from a bulk crystalline sample and let it vary isotropically, any possible local distortion of

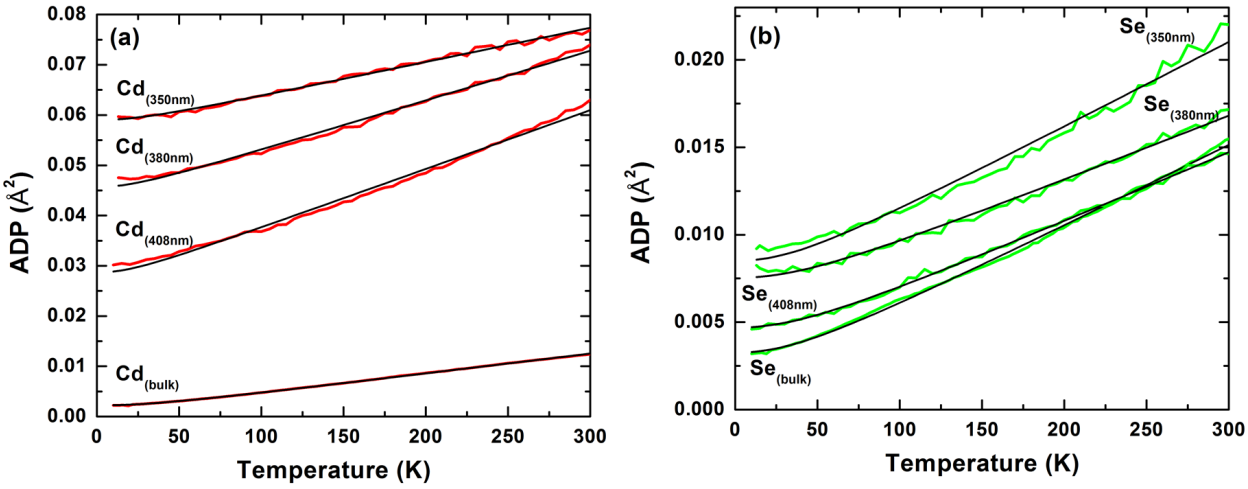

Figure 6.7: The fits of thermal curves of (a) Cd and (b) Se using a Debye model. The Cd and Se are in red and green colors while the Debye fit in black lines. Clusters with different sizes are labelled.

individual atoms may be missing. The slight increase of R_w with reduced size suggests a larger deviation from ideal pyramid structure cut from a bulk lattice. As shown in Fig. 6.6(e), the ADP values for Cd are unphysically large, implying significant disorder in the clusters. The possible reasons for the large offset seen are either stacking faults in the clusters, which is common in II-V nanocrystals such as CdSe [Masadeh *et al.*, 2007; Yang *et al.*, 2013] and CdS [Farrow *et al.*, 2014], or increasing numbers of under-bonded surface atoms with decreased sizes that have large vibrational amplitude.

Looking closely at thermal curves in Fig. 6.6(e), one may see that the ADP curves of the clusters don't seem to follow a Debye behavior where ideally the thermal curves should bend at low temperature but increase linearly with temperature at a high temperature region. This indicates the presence of lattice anharmonicity and is further supported by the poor Debye model fits of the ADP curves from clusters as displayed in Fig. 6.7. The violent vibration of underbonded surface atoms may also account for the anharmonicity observed here.

To understand the blue-shift trend observed in measured PDOS, we look at the first PDF peak

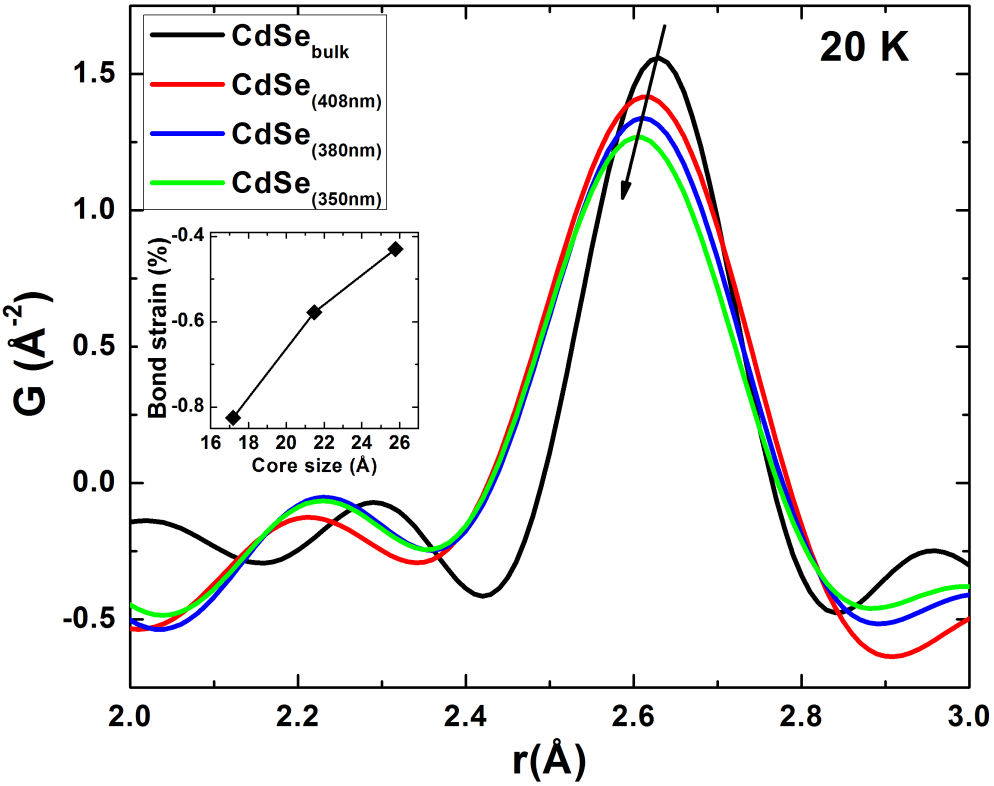

Figure 6.8: The first PDF peaks of CdSe clusters and bulk. The size dependent strain is shown in the inset.

of PDFs for all bulk and cluster samples. This peak comes from the covalently bonded Cd-Se in $CdSe_4$ tetrahedron. As shown in Fig. 6.8, the nearest neighbor Cd-Se peak shifts to low-r with decreasing size, indicating that the average bond gets shorter as size is reduced. The trend that the Cd-Se nearest neighbor bond becomes shorter with decreased size does not explain, but is consistent with, the blue-shift seen in measured PDOS.

One can quantitatively calculate the strains using the relation $\epsilon_{cluster} = [FPP(cluster) - FPP(bulk))/FPP(bulk)] \times 100\%$ where FPP stands for first peak positions. The FPP can be extracted by fitting a Gaussian function [Yang *et al.*, 2013; Masadeh *et al.*, 2007] which are summarized in Table. 6.7 together with first peak width. The strains are plotted as a function of cluster core size in the inset of Fig. 6.8. The compressive strains for sub-2 nm CdSe nanoclusters in current study are consistently less than 1 %, which is smaller than $\sim 2\%$ for CdSe nanoparticle with a size

Table 6.7: The first PDF peak positions (FPP) and peak widths (FPW) for CdSe clusters and bulk sample. Core size corresponds to the edge size of the cluster.

	Core Size (Å)	FPP (Å)	FPW (Å)
bulk	∞	2.6293	0.2064
408 nm	25.78	2.6180	0.2714
380 nm	21.48	2.6141	0.2558
350 nm	17.19	2.6076	0.2525

of 1.3 nm as reported by Yang *et al.* [Yang *et al.*, 2013].

6.3 Conclusion

In this chapter we first examined the lattice dynamics in bulk CdSe by testing the validity of theoretical techniques such as empirical interatomic potentials and density functional theory against experimental results from INS and IXS. We found that the DFT has a closer agreement with experiments than do force fields. This is maybe not surprising, given the greater accuracy of DFT. However, the discrepancy of the high frequency modes in the FF models is large, and any property that depends on these will not be well represented by the force fields. We then moved on to investigate the lattice dynamics of three "magic size" CdSe clusters by using inelastic x-ray scattering and temperature dependent PDF coupled with DFT simulation. We see that in clusters there are large disorders and the thermal curves show non-Debye behavior. The observed overall blue-shift in PDOS with reduced size is consistent with the shift to low-r of first PDF peak. We believe current exemplary study would open the door to a large number of future dynamic studies on low-dimensional systems.

Chapter 7

Summary and Outlook

Low-dimensional materials have been attracting tremendous attention in the past two decades and it is reasonable to believe they will continue to be the center of focus of numerous research in the years to come. Fundamental aspects, such as the structure and lattice dynamics, of these materials, will be the important key to better understand these materials and facilitate potential applications such as in energy storage or catalysts.

The current thesis work partially addressed the structural and dynamical aspects of a number of selected low-dimensional materials. We found that both MXene and zirconium phosphonate based ion exchange materials have two-dimensional layered structure. For these 2D nanocrystals the modeling approach using a shape function often breaks because, at this length scale, the layers are often not stacked in a good order which is known as "turbostratic disorder". As an alternative, we demonstrated that creating a model by cutting a single layer of atoms from bulk lattice and calculating its PDF using Debye scattering equation gives more physically reasonable parameters and better fits. Using this new approach, a complete structural solution rather than an approximated structure model using shape functions is obtained. Knowing precisely where each atom sits would enable first principles calculation, which would in turn help understand experimental results or provide guidance for future research direction.

On the lattice dynamics side, we first investigated the atomic bonding strength in size dependent

platinum nanoparticles. By employing a simple Debye model and analyzing the extracted Debye temperatures, we saw the bond softening below a particle size of 2 nm. However, in platinum project the Debye model is a much simplified model for lattice dynamics study. Also the way used to approximate "surface effect" in these particles is oversimplified. Motivated by this, we collected non-resonant inelastic x-ray scattering data on three quantized grown sub-2 nm CdSe quantum dots. The phonon density of states obtained from HERIX experiment gives a complete picture of lattice dynamics of material systems. In CdSe clusters we observed an overall blue-shift with decreased particle size.

This thesis would be beneficial for those studying low-dimensional materials. Not only did it exemplify the way for a structural solution on selected two-dimensional materials in particular but more importantly, it discusses and demonstrates, in general, the methodology (shape function versus Debye function analysis) for determining structures of low-dimensional materials. With the increasing number of novel nanoscaled materials being synthesized at laboratories across the globe, a precise picture of their three-dimensional structure would be of paramount importance to establish the structure-property correlation. On the other hand, the demonstrated work on mapping out PDOS of ultrasmall CdSe nanoclusters would provide a unique opportunity to find out the real lattice dynamics in these and other technologically important low-dimensional materials. The experimental approach described in the thesis yields lattice dynamical information of high level of accuracy when compared with other theoretical calculations such as force fields or DFT that have been extensively applied but suffer from approximations.

Looking ahead here are few thoughts on both topics. (i) For the purpose of extracting "robust" structural and morphological parameters from low-dimensional materials, solely based on one experimental probe such as PDF is not sufficient. It is preferred to combine data from various probes, both experimentally and theoretically, and put them in a "complex modeling" framework. One such example is to obtain reliable structural and morphological parameters on CdS nanoparticles by using a combination of PDF and small angle x-ray scattering (SAXS) data [Farrow *et al.*, 2014]. (ii) We are expecting more flexible and easy-to-use programs in modeling the low-

dimensional materials. Currently there are several PDF modeling software programs available including PDFgui [Farrow *et al.*, 2007], DiffPy-CMI [Juhs *et al.*, 2015], DISCUS [Neder and Proffen, 2008] and RMCprofile [Tucker *et al.*, 2007]. Considering the modeling programs in Billinge group, PDFgui is an easy-to-use program but incapable of tackling complex modeling problems. In contrast DiffPy-CMI is more versatile and capable of dealing with many complicated problems. It is Python-driven and users can write customized scripts. Despite of many well-written example scripts, to fully exploit DiffPy-CMI takes time and practice. The situation could be much improved if researchers in the community share their codes when they publish papers. These could be done in the form of IPython Notebooks. Also, a cookbook similar to DISCUS will be a great starting point for beginners. (iii) high energy resolution inelastic x-ray scattering technique is a powerful tool of mapping the collective motions of atoms in low-dimensional materials. However, the disadvantage with it is obvious. Due to limited number of slots for experiments, it is not unusual to wait up to two years for a single measurement. This could not satisfy the needs for the ever-increasing number of new low-dimensional materials synthesized in laboratories. To relieve the situation, it is worth exploring the possibility of extracting robust lattice dynamical information from a combination of more routine and easy-to-access probes/methods such as a combination of Raman scattering, temperature dependent PDF, molecular dynamics and density functional theory.

The thesis work resulted in ten manuscripts where six of them have been published, one is under review at *Journal of the American Chemical Society* and three others are in preparation. The published papers are [Tiano *et al.*, 2015; Shi *et al.*, 2014; Ghidiu *et al.*, 2014; Farrow *et al.*, 2014; Zhu *et al.*, 2014; Shi *et al.*, 2013]. Manuscripts based on Chapter 4 (structure investigation on zirconium phosphonate nanoparticles) and Chapter 6 (lattice dynamics of bulk CdSe and nanolcusters) are in preparation.

Part II

Bibliography

Bibliography

[Abel *et al.*, 2011] M. Abel, S. Clair, O. Ourdjini, M. Mossoyan, and L. Porte. Single layer of polymeric Fe-phthalocyanine: an organometallic sheet on metal and thin insulating film. *J. Am. Chem. Soc.*, 133:1203–1205, 2011.

[Abeykoon *et al.*, 2013] Milinda Abeykoon, Emil S. Bozin, Genda Gu, John Hill, John Tranquada, and Simon J. L. Billinge. Evidence for short-range-ordered charge stripes far above the charge-ordering transition in $La_{1.67}Sr_{0.33}NiO_4$. *Phys. Rev. Lett.*, 111:096404, 2013.

[Alberti *et al.*, 1993] G. Alberti, U. Costantino, F. Marmottini, R. Vivani, and P. Zappelli. Zirconium phosphite diphosphonate, a microporous, layered, inorganic-organic polymer. *Angew. Chem. Int. Ed.*, 32:1357–1359, 1993.

[Alexandrov *et al.*, 1993] A. S. Alexandrov, A. M.. Bratkovsky, N. F. Mott, and E. K. H. Salje. near-infrared absorption of YBCO. *Physica C*, 215:359, 1993.

[Alivisatos *et al.*, 1998] A. P. Alivisatos, P. F. Barbara, A. W. Castleman, J. Chang, D. A. Dixon, M. L. Kline, G. L. McLondon, J. S. Miller, M. A. Ratner, P. J. Rossky, S. I. Stupp, and M. I. Thompson. From molecules to materials: Current trends and future directions. *Adv. Mater.*, 10:1297–1336, Nov. 1998.

[Alivisatos, 1996] A. P. Alivisatos. Semiconductor clusters, nanocrystals, and quantum dots. *Science*, 271:933–937, 1996.

[Alivisatos, 2004] P. Alivisatos. The use of nanocrystals in biological detection. *Nat. Biotechnol*, 22:47–52, 2004.

[Amo-Ochoa *et al.*, 2010] P. Amo-Ochoa, L. Welte, R. Gonzalez-Prieto, P. J. Sanz Miguel, C. J. Gomez-Garcia, E. Mateo-Marti, S. Delgado, J. Gomez-Herrero, and F. Zamora. Single layers of a multifunctional laminar Cu(I,II) coordination polymer. *Chem. Commun.*, 46:3262–3264, 2010.

[Anderson, 1963] O. L. Anderson. A simplified method for calculating the Debye temperature from elastic constants. *J. Phys. Chem. Solids*, 24:909–917, 1963.

[Araujo *et al.*, 2006] L. L. Araujo, P. Kluth, G. de M. Azevedo, and M. C. Ridgway. Vibrational properties of Ge nanocrystals determined by EXAFS. *Phys. Rev. B*, 74:184102, 2006.

[Ashcroft and Mermin, 1976] N. W. Ashcroft and N. D. Mermin. *Solid State Physics*. Holt, Rinehart and Winston, New York, USA, 1976.

[Balerna and Mobilio, 1986] A. Balerna and S. Mobilio. Dynamic properties and debye temperatures of bulk Au and Au clusters studied using extended x-ray-absorption fine-structure spectroscopy. *Phys. Rev. B*, 34:2293–2298, 1986.

[Ball and Garwin, 1992] P. Ball and L. Garwin. Science at the atomic scale. *Nature*, 355:761–766, Feb. 1992.

[Baroni *et al.*, 2001] Stefano Baroni, Stefano de Gironcoli, Andrea Dal Corso, and Paolo Giannozzi. Phonons and related crystal properties from density-functional perturbation theory. *Rev. Mod. Phys.*, 73:515–562, Jul 2001.

[Barsoum, 2013] M. W. Barsoum. *MAX phases: properties of machinable ternary carbides and nitrides*. John Wiley & Sons, 2013.

[Bealing *et al.*, 2012] C. R. Bealing, W. J. Baumgardner, J. J. Choi, T. Hanrath, and R. G. Hennig. Predicting nanocrystal shape through consideration of surface-ligand interactions. *ACS Nano*, 6:2118–2127, 2012.

[Bediako *et al.*, 2012] D. K. Bediako, B. Lassalle-Kaiser, Y. Surendranath, J. Yano, V. K. Yachandra, and D. G. Nocera. Structure-activity correlation in a nickel-borate oxygen evolution catalyst. *J. Am. Chem. Soc.*, 134:6801–6809, March 14 2012.

[Beecher *et al.*, 2014] Alexander N. Beecher, Xiaohao Yang, Joshua H. Palmer, Alexandra L. LaGrassa, Pavol Juhas, Simon J. L. Billinge, and Jonathan S. Owen. Atomic structures and gram scale synthesis of three tetrahedral quantum dots. *J. Am. Chem. Soc.*, 136(30):10645–10653, 2014.

[Bell, 2003] Alexis T Bell. The impact of nanoscience on heterogeneous catalysis. *Science*, 299(5613):1688–1691, 2003.

[Benkabou *et al.*, 2000] F. Benkabou, H. Aourag, and M. Certier. Atomistic study of zinc-blende CdS, CdSe, ZnS, and ZnSe from molecular dynamics. *Mater. Chem. Phys.*, 66:10, 2000.

[Billinge and Farrow, 2013] Simon J. L. Billinge and Christopher L. Farrow. Towards a robust *ad-hoc* data correction approach that yields reliable atomic pair distribution functions from powder diffraction data. *J. Phys: Condens. Mat.*, 25:454202, 2013.

[Billinge and Kanatzidis, 2004] S. J. L. Billinge and M. G. Kanatzidis. Beyond crystallography: the study of disorder, nanocrystallinity and crystallographically challenged materials. *Chem. Commun.*, 7:749–760, 2004.

[Billinge and Levin, 2007] S. J. L. Billinge and I. Levin. The problem with determining atomic structure at the nanoscale. *Science*, 316:561–565, 2007.

[Billinge *et al.*, 1991] S. J. L. Billinge, P. K. Davies, T. Egami, and C. R. A. Catlow. Deviations from planarity of copper-oxygen sheet in $Ca_{0.85}Sr_{0.15}CuO_2$. *Phys. Rev. B*, 43:10340, 1991.

[Billinge, 2008] Simon J. L. Billinge. Nanoscale structural order from the atomic pair distribution function (PDF): There's plenty of room in the middle. *J. Solid State Chem.*, 181:1695–1700, 2008.

[Blöchl, 1994] P. E. Blöchl. Projector augmented-wave method. *Phys. Rev. B*, 50(24):17953, Dec 1994.

[Bonello and Fernandez, 1993] B. Bonello and B. Fernandez. Elastic constants of CdSe at low temperature. *J. Phys. Chem. Solids*, 54:209, 1993.

[Bosak and Krisch, 2005] Alexey Bosak and Michael Krisch. Phonon density of states probed by inelastic x-ray scattering. *Phys. Rev. B*, 72:224305, 2005.

[Bouamama *et al.*, 2009] K. Bouamama, P. Djemia, N. Lebga, and K. Kassali. Ab initio calculation of the elastic properties and the lattice dynamics of the $Zn_xCd_{1-x}Se$ alloy. *Semicond. Sci. Technol.*, 24:045005, 2009.

[Bragg and Bragg, 1913] W. H. Bragg and W. L. Bragg. The reflection of x-rays by crystals. *Proc. R. Soc. Lond. A*, 88:428–438, 1913.

[Bragg, 1914] Wm. H. Bragg. X-rays and crystalline structure. *Science*, 40:795–802, 1914.

[Brockhouse and Hurst, 1952] B. N. Brockhouse and D. G. Hurst. Energy distribution of slow neutrons scattered from solids. *Phys. Rev.*, 88:542, 1952.

[Brown and Altermatt, 1985] I. D. Brown and D. Altermatt. Bond-valence parameters obtained from a systematic analysis of the inorganic crystal structure database. *Acta Crystallogr. B*, 41(4):244–247, 1985.

[Brown *et al.*, 2014] P. R. Brown, D. Kim, R. R. Lunt, N. Zhao, M. G. Bawendi, J. C. Grossman, and V. Bulovic. Energy level modification in lead sulfide quantum dot thin films through ligand exchange. *ACS Nano*, 8:5863–5872, 2014.

[Budai *et al.*, 2014] John D. Budai, Jiawang Hong, Michael E. Manley, Eliot D. Specht, Chen W. Li, Jonathan Z. Tischler, Douglas L. Abernathy, Ayman H. Said, Bogdan M. Leu, Lynn A. Boatner, Robert J. McQueeney, and Olivier Delaire. Metallization of vanadium dioxide driven by large phonon entropy. *Nature*, 515:535–539, 2014.

[Burkel, 2003] E. Burkel. Dynamics of new materials probed by inelastic x-ray scattering. *Nucl. Instrum. Meth. B*, 199:143–150, 2003.

[Burns *et al.*, 2012] J. D. Burns, T. C. Shehee, A. Clearfield, and D. T. Hobbs. Separation of americium from curium by oxidation and ion exchange. *Anal. Chem.*, 84:6930–6932, 2012.

[Byrd *et al.*, 1996] H. Byrd, A. Clearfield, D. Poojary, K. P. Reis, and M. E. Thompson. Crystal structure of a porous zirconium phosphate/phosphonate compound and photocatalytic hydrogen production from related materials. *Chem. Mater.*, 8:2239–2246, 1996.

[Cademartiri *et al.*, 2006] L. Cademartiri, E. Montanari, G. Calestani, A. Migliori, A. Guagliardi, and G. A. Ozin. Size-dependent extinction coefficients of PbS quantum dots. *J. Am. Chem. Soc.*, 128:10337–10346, 2006.

[Cardona and Merlin, 2007] M. Cardona and R. Merlin. *Light scattering in solid IX*. Springer, 2007.

[Cernuto *et al.*, 2011] G. Cernuto, N. Masciocchi, A. Cervellino, G. M. Colonna, and A. Guagliardi. Size and shape dependence of the photocatalytic activity of TiO_2 nanocrystals: a total scattering debye function study. *J. Am. Chem. Soc.*, 133:3114–3119, 2011.

[Cervellino *et al.*, 2010] Antonio Cervellino, Cinzia Giannini, and Antonietta Guagliardi. DEBUSSY: a Debye user system for nanocrystalline materials. *J. Appl. Crystallogr.*, 43:1543–1547, 2010.

[Chan and Nie, 1998] W. C.W Chan and S. M. Nie. Quantum dot bioconjugates for ultrasensitive nonisotopic detection. *Science*, 281(5385):2016–2018, 1998.

[Chan *et al.*, 2004] C. P. Chan, Y. Bruemmel, M. Seydack, K. Sin, L. Wong, E. Merisko-Liversidge, D. Trau, and R. Renneberg. Nanocrystal biolabels with releasable fluorophores for immunoassays. *Anal. Chem.*, 76:3638–3645, Jul. 2004.

[Chaplot *et al.*, 2010] S. L. Chaplot, R. Mittal, and N. Choudhury. *Thermodynamic properties of solids*. Wiley-VCH, 2010.

[Chapman *et al.*, 2005] Karena W. Chapman, Peter J. Chupas, and Cameron J. Kepert. Selective recovery of dynamic guest structure, in a nanoporous Prussian Blue through in situ X-ray diffraction: A differential pair distribution function analysis. *J. Am. Chem. Soc.*, 127(32):11232–11233, 2005.

[Chapman *et al.*, 2006] Karena W. Chapman, Peter J. Chupas, Evan R. Maxey, and James W. Richardson. Direct observation of adsorbed H_2-framework interactions in the Prussian Blue analogue Mn-3(II)[Co-III$(CN)_6]_2$: The relative importance of accessible coordination sites and van der Waals interactions. *Chem. Commun.*, pages 4013–4015, 2006.

[Chen *et al.*, 2006] Jian-Feng Chen, Ji-Yao Zhang, Zhi-Gang Shen, Jie Zhong, and Jimmy Yun. Preparation and Characterization of Amorphous Cefuroxime Axetil Drug Nanoparticles with Novel Technology: High-Gravity Antisolvent Precipitation. *Ind. Eng. Chem. Res.*, 45(25):8723–8727, December 2006.

[Chupas *et al.*, 2003] Peter J. Chupas, Xiangyun Qiu, J. C. Hanson, P. L. Lee, Clare P. Grey, and Simon J. L. Billinge. Rapid acquisition pair distribution function analysis (RA-PDF). *J. Appl. Crystallogr.*, 36:1342–1347, 2003.

[Chupas *et al.*, 2007] Peter J. Chupas, Karena W. Chapman, Guy Jennings, Peter L. Lee, and Clare P. Grey. Watching nanoparticles grow: The mechanism and kinetics for the formation of TiO_2-supported platinum nanoparticles. *J. Am. Chem. Soc.*, 129(45):13822–13824, 2007.

[Ci *et al.*, 2010] L. Ci, L. Song, C. Jin, D. Jariwala, D. Wu, Y. Li, A. Srivastava, Z. F. Wang, K. Storr, L. Balicas, F. Liu, and P. M. Ajayan. Atomic layers of hybridized boron nitride and graphene domains. *Nature Mater.*, 9:430–435, 2010.

[Clearfield and Smith, 1969] A. Clearfield and G. D. Smith. The crystallography and structure of α-zirconium bis(monohydrogen orthophosphate) monohydrate. *Inorg. Chem.*, 8(3):431–436, 1969.

[Clearfield, 2008] A. Clearfield. Unconventional metal organic frameworks: porous cross-linked phosphonates. *Dalton Trans.*, (44):6089–6103, 2008.

[Cline *et al.*, 1967] C. F. Cline, H. L. Dunegan, and G. W. Henderson. Elastic constants of hexagonal BeO, ZnS, and CdSe. *J. Appl. Phys.*, 38:1946, 1967.

[Coleman *et al.*, 2011] J. N. Coleman, M. Lotya, A. O'Neill, S. D. Bergin, P. J. King, U. Khan, K. Young, A. Gaucher, S. De, R. J. Smith, I. V. Shvets, S. K. Arora, G. Stanton, H. Kim, K. Lee, G. T. Kim, G. S. Duesberg, T. Hallam, J. J. Boland, J. J. Wang, J. F. Donegan, J. C. Grunlan, G. Moriaty, A. Shmeliov, R. J. Nicholls, J. M. Perkins, E. M. Grieveson, K. Theuwissen, D. W. McComb, P. D. Nellist, and V. Nicolosi. Two-dimensional nanosheets produced by liquid exfoliation of layered mmaterials. *Science*, 331(6017):568–571, 2011.

[Come *et al.*, 2012] J. Come, M. Naguib, P. Rozier, M. W. Barsoum, Y. Gogotsi, P. L. Taberna, M. Morcrette, and P. Simon. A non-aqueous asymmetric cell with a Ti_2C-based two-dimensional negative electrode. *J. Electrochem. Soc.*, 159:A1368–A1373, 2012.

[Corso *et al.*, 1993] A. D. Corso, S. Baroni, R. Resta, and S. de Gironcoli. Ab initio calculation of phonon dispersions in II-VI semiconductors. *Phys. Rev. B*, 47:3588, Feb 1993.

[Cossairt *et al.*, 2011] Brandi M. Cossairt, Pavol Juhás, Simon J. L. Billinge, and Jonathan S. Owen. Tuning the surface structure and optical properties of CdSe clusters using coordination chemistry. *J. Phys. Chem. Lett.*, 2:3075–3080, 2011.

[Cuenya *et al.*, 2007] B. R. Cuenya, A. Naitabdi, J. Croy, W. Sturhahn, J. Y. Zhao, E. E. Alp, R. Meyer, D. Sudfeld, E. Schuster, and W. Keune. Atmoic vibrations in iron nanoclusters:

Nuclear resonant inelastic x-ray scattering and molecular dynamics simulations. *Phys. Rev. B*, 76:195422, Nov 15 2007.

[Cuenya *et al.*, 2009] B. R. Cuenya, J. R. Croy, L. K. Ono, A. Naitabdi, H. Heinrich, W. Keune, J. Zhao, W. Sturhahn, E. E. Alp, and M. Hu. Phonon density of states of self-assembled isolated Fe-rich Fe-Pt alloy nanoclusters. *Phys. Rev. B*, 80:125412, Sep 16 2009.

[Cuenya *et al.*, 2011] B. R. Cuenya, M. A. Ortigoza, L. K. Ono, F. Behafarid, S. Mostafa, J. R. Croy, K. Paredis, G. shafai, T. S. Rahman, L. Li, Z. Zhang, and J. C. Yang. Thermodynamic properties of Pt nanoparticles: size, shape, support, and adsorbate effects. *Phys. Rev. B*, 84:245438, 2011.

[Cuenya *et al.*, 2012] B. R. Cuenya, L. K. Ono, J. R. Croy, K. Paredis, A. Kara, H. Heinrich, J. Zhao, E. E. Alp, A. T. DelaRiva, A. Datye, E. A. Stach, and W. Keune. Size-dependent evolution of the atomic vibrational density of states and thermodynamic properties of isolated Fe nanoparticles. *Phys. Rev. B*, 86:165406, Oct. 2 2012.

[Debye, 1912] P. Debye. Zur theorie der spezifischen wärmen. *Ann. Phys.-Berlin*, 39:789, 1912.

[Debye, 1915] P. Debye. Dispersion of Röntgen rays. *Annalen der Physik (Berlin, Germany)*, 351:809–823, 1915.

[Dines *et al.*, 1983] M. B. Dines, R. E. Cooksey, P. C. Griffith, and R. H. Lane. Mixed-component layered tetravalent metal phosphonates phosphates as precursors for microporous materials. *Inorg. Chem.*, 22:1003–1004, 1983.

[Dore *et al.*, 2004] P. Dore, A. Funaro, A. Sacchetti, M. Angeloni, and G. Balestrino. Study of infrared phonons in the $La_{0.7}Sr_{0.3}MnO_3$ manganite by means of reflectance measurements on epitaxial films. *Eur. Phys. J. B*, 37:339–344, 2004.

[Dove, 1993] M. T. Dove. *Introduction to lattice dynamics*. Cambridge University Press, 1993.

[Dove, 2003] M. T. Dove. *Structure and dynamics: an atomic view of materials*. Oxford University Press, 2003.

[Du *et al.*, 2012] P. Du, O. Kokhan, K. W. Chapman, P. J. Chupas, and D. M. Tiede. Elucidating the domain structure of the cobalt oxide water splitting catalyst by x-ray pair distribution function analysis. *J. Am. Chem. Soc.*, 134:11096–11099, June 21 2012.

[Eda *et al.*, 2012] G. Eda, T. Fujita, H. Yamaguchi, D. Voiry, M. Chen, and M. Chhowalla. Coherent atomic and electronic heterostructures of single-layer MoS_2. *ACS Nano*, 6:7311–7317, 2012.

[Egami and Billinge, 2012] T. Egami and S. J. L. Billinge. *Underneath the Bragg peaks: structural analysis of complex materials*. Elsevier, Amsterdam, 2nd edition, 2012.

[Einstein, 1911] A. Einstein. Elementary observations on the thermic molecular movements in the firm bodies. *Ann. Phys.*, 35:679, 1911.

[El-Sayed *et al.*, 2006] Ivan H. El-Sayed, Xiaohua Huang, and Mostafa A. El-Sayed. Selective laser photo-thermal therapy of epithelial carcinoma using anti-egfr antibody conjugated gold nanoparticles. *Cancer Lett.*, 239:129–135, July 2006.

[Enyashin and Ivanovskii, 2012] A. N. Enyashin and A. L. Ivanovskii. Atomic structure, comparative stability and electronic properties of hydroxylated Ti_2C and Ti_3C_2 nanotubes. *Comput. Theor. Chem.*, 989:27–32, 2012.

[Fafard *et al.*, 1996] S. Fafard, K. Hinzer, S. Raymond, M. Dion, J. McCaffrey, Y. Feng, and S. Charbonneau. Red-emitting semiconductor quantum dot lasers. *Science*, 274:1350–1353, Nov. 1996.

[Fan *et al.*, 2000] H. Fan, Y. Lu, A. Stump, S. T. Reed, T. Baer, R. Schunk, V. Perez-Luna, G. P. Lopez, and C. J. Brinker. Rapid prototyping of patterned functional nanostructures. *Nature*, 405:56–60, May 2000.

[Farrow and Billinge, 2009] C. L. Farrow and S. J. L. Billinge. Relationship between the atomic pair distribution function and small angle scattering: implications for modeling of nanoparticles. *Acta Crystallogr. A*, 65(3):232–239, 2009.

[Farrow *et al.*, 2007] C. L. Farrow, P. Juhás, Jiwu Liu, D. Bryndin, E. S. Božin, J. Bloch, Th. Proffen, and S. J. L. Billinge. PDFfit2 and PDFgui: Computer programs for studying nanostructure in crystals. *J. Phys: Condens. Mat.*, 19:335219, 2007.

[Farrow *et al.*, 2013] Christopher L. Farrow, D. Kwabena Bediako, Yogesh Surendranath, Daniel G. Nocera, and Simon J. L. Billinge. Intermediate-range structure of self-assembled cobalt-based oxygen evolving catalysts. *J. Am. Chem. Soc.*, 135:6403–6406, 2013.

[Farrow *et al.*, 2014] Christoper L. Farrow, Chenyang Shi, Pavol Juhás, Xiaogang Peng, and Simon J. L. Billinge. Robust structure and morphology parameters for CdS nanoparticles by combining small angle X-ray scattering and atomic pair distribution function data in a complex modeling framework. *J. Appl. Crystallogr.*, 47:561–565, 2014. Selected as journal cover.

[Feng *et al.*, 2012] J. Feng, L. Peng, C. Wu, X. Sun, S. Hu, C. Lin, J. Dai, J. Yang, and Y. Xie. Giant moisture responsiveness of VS_2 ultrathin nanosheets for novel touchless positioning interface. *Adv. Mater.*, 24:1969–1974, 2012.

[Frase *et al.*, 1998] H. Frase, B. Fultz, and J. L. Robertson. Phonons in nanocrystalline Ni_3Fe. *Phys. Rev. B*, 57:898, 1998.

[Frenkel and Rehr, 1993] A. I. Frenkel and J. J. Rehr. Thermal expansion and x-ray-absorption fine-structure cumulants. *Phys. Rev. B*, 48:585–588, Jul 1993.

[Frenkel *et al.*, 2001] A. I. Frenkel, C. W. Hills, and R. G. Nuzzo. A view from the inside: complexity in the atomic scale ordering of supported metal nanoparticles. *J. Phys. Chem. B*, 105(51):12689, Dec 27 2001.

[Frenkel *et al.*, 2012] A. I. Frenkel, R. Vasic, B. Dukesz, D. Li, M. Chen, and T. Fujita. Thermal properties of nanoporous gold. *Phys. Rev. B*, 85:195419, 2012.

[Fu *et al.*, 2003] Qi Fu, Howard Saltsburg, and Maria Flytzani-Stephanopoulos. Active nonmetallic Au and Pt species on ceria-based water-gas shift catalysts. *Science*, 301:935–938, July 2003.

[Fultz *et al.*, 1996] B. Fultz, J. L. Robertson, T. A. Stephens, L. J. Nagel, and S. Spooner. Phonon density of states of nanocrystalline Fe prepared by high-energy ball milling. *J. Appl. Phys.*, 79:8318, 1996.

[Gagnon *et al.*, 2012] K. J. Gagnon, H. P. Perry, and A. Clearfield. Conventional and unconventional metal-organic frameworks based on phosphonate ligands: MOFs and UMOFs. *Chem. Rev.*, 112:1034–1054, 2012.

[Gale and Rohl, 2003] J. D. Gale and A. L. Rohl. The general utility lattice program (GULP). *Mol. Simul.*, 29:291–341, 2003.

[Gale, 1997] J. D. Gale. Gulp: A computer program for the symmetry-adapted simulation of solids. *J. Chem. Soc. Faraday Trans.*, 93:629, 1997.

[Geim and Novoselov, 2007] A. K. Geim and K. S. Novoselov. The rise of graphene. *Nature Mater.*, 6:183–191, 2007.

[Ghidiu *et al.*, 2014] Michael Ghidiu, Michael Naguib, Chenyang Shi, Olha Mashtalir, Limei Pan, Bo Zhang, Jian Yang, Yury Gogotsi, Simon J. L. Billinge, and Michel W. Barsoum. Synthesis and charaterization of two-dimensional Nb_4C_3 (MXene). *Chem. Commun.*, 50:9517–9520, 2014.

[Ghosh *et al.*, 2003] S. Ghosh, A. K. Sood, and N. Kumar. Carbon nanotube flow sensors. *Science*, 299:1042–1044, Feb. 2003.

[Gilbert *et al.*, 2004] B. Gilbert, F. Huang, H. Zhang, G. A. Waychunas, and J. F. Banfield. Nanoparticles: Strained and stiff. *Science*, 305:651–654, 2004.

[Gilbert, 2008] Benjamin Gilbert. Finite size effects on the real-space pair distribution function of nanoparticles. *J. Appl. Crystallogr.*, 41:554, 2008.

[Giulian *et al.*, 2009] R. Giulian, L. L. Araujo, P. Kluth, D. J. Sprouster, C. S. Schnohr, G. J. Foran, and M. C. Ridgway. Temperature-dependent exafs analysis of embedded Pt nanocrystals. *J. Phys.: Condens. Mat.*, 21:155302, 2009.

[Goldstein *et al.*, 1992] A. N. Goldstein, C. M. Echer, and A. P. Alivisatos. Melting in semiconductor nanocrystals. *Science*, 256(5062):1425–1427, 1992.

[Gorbachev *et al.*, 2011] R. V. Gorbachev, I. Riaz, R. R. Nair, R. Jalil, L. Britnell, B. D. Belle, E. W. Hill, K. S. Novoselov, K. Watanabe, T. Taniguchi, A. K. Geim, and P. Blake. Hunting for monolayer boron nitride: optical and raman signatures. *Small*, 7:465–468, Jan. 2011.

[Gretarsson *et al.*, 2013] H. Gretarsson, J. P. Clancy, X. Liu, J. P. Hill, E. S. Bozin, Y. Singh, S. Manni, P. Gegenwart, J. H. Kim, A. H. Said, D. Casa, T. Gog, M. H. Upton, H.-S. Kim, J. Yu, V. M. Katukuri, L. Hozoi, J. van den Brink, and Y.-J. Kim. Crystal-field splitting and correlation effect on the electronic structure of A_2IrO_3. *Phys. Rev. Lett.*, 110:076402, 2013.

[Gu *et al.*, 2003] H. Gu, P. L. Ho, K. W. T. Tsang, L. Wang, and B. Xu. Using biofunctional magnetic nanoparticles to capture vancomycin-resistant enterococci and other gram-positive bacteria at ultralow concentration. *J. Am. Chem. Soc.*, 125:15702–15703, Dec. 2003.

[Gu *et al.*, 2004] Y. Gu, I. L. Kuskovsky, M. Yin, S. O'Brien, and G. F. Neumark. Quantum confinement in ZnO nanorods. *Appl. Phys. Lett.*, 85:3833–3835, Oct. 2004.

[Guagliardi *et al.*, 2010] A. Guagliardi, A. Cedola, C. Giannini, M. Ladisa, A. Cervellino, A. Sorrentino, S. Lagomarsino, Cancedda R, and M. Mastrogiacomo. Debye function analysis and 2D imaging of nanoscaled engineered bone. *Biomaterials*, 31:8289–8298, 2010.

[Guo and Dong, 2011] S. Guo and S. Dong. Graphene nanosheet: synthesis, molecular engineering, thin film, hybrids, and energy and analytical applications. *Chem. Soc. Rev.*, 40:2644–2672, 2011.

[Hammersley *et al.*, 1996] A. P. Hammersley, S. O. Svenson, M. Hanfland, and D. Hauserman. Two-dimensional detector software: from real detector to idealised image or two-theta scan. *High Pressure Res.*, 14:235–248, 1996.

[Han and Bester, 2011] Peng Han and Gabriel Bester. Interatomic potentials for the vibrational properties of III-V semiconductor nanostructures. *Phys. Rev. B*, 83:174304, 2011.

[Han and Bester, 2012a] Peng Han and Gabriel Bester. Confinement effects on the vibrational properties of III-V and II-VI nanoclusters. *Phys. Rev. B*, 85:041306(R), 2012.

[Han and Bester, 2012b] Peng Han and Gabriel Bester. Insights about the surface of colloidal nanoclusters from their vibrational and thermodynamic properties. *J. Phys. Chem. C*, 116:10790–10795, 2012.

[Han *et al.*, 2008] W. Han, L. Wu, Y. Zhu, K. Watanabe, and T. Taniguchi. Structure of chemically derived mono- and few-atomic-layer boron nitride sheets. *Appl. Phys. Lett.*, 93:223103, 2008.

[Harrington *et al.*, 2010] Richard Harrington, Douglas B. Hausner, Narayan Bhandari, Daniel R. Strongin, and Karena W. Chapman. Investigation of surface structures by powder diffraction: A differential pair distribution function study on arsenate sorption on ferrihydrite. *Inorg. Chem.*, 49(1):325–330, 2010.

[Hossain *et al.*, 2011] M. Z. Hossain, S. L. Rumyantsev, K. M. F. Shahil, D. Teweldebrhan, M. Shur, and A. A. Balandin. Low-frequency current fluctuations in graphene-like exfoliated thin-films of bismuth selenide topological insulators. *ACS Nano*, 5:2657–2663, March 2011.

[Hu *et al.*, 2007] Chunfeng Hu, Fangzhi Li, Jie Zhang, Jiemin Wang, Jingyang Wang, and Yanchun Zhou. Nb_4AlC_3: A new compound belong to the max phases. *Scripta Mater.*, 57:893–896, 2007.

[Hu *et al.*, 2012] P. Hu, Z. Wen, L. Wang, P. Tan, and K. Xiao. Synthesis of few-layer gase nanosheets for high performance photodetectors. *ACS Nano*, 6:5988–5994, June 2012.

[Jensen *et al.*, 2012] Kirsten M. Ø Jensen, Mogens Christensen, Pavol Juhás, Christoffer Tyrsted, Espen D. Bøjesen, Nina Lock, Simon J. L. Billinge, and Bo B. Iversen. Revealing the mechanisms behind SnO_2 nanoparticle formation and growth during hydrothermal synthesis: an in situ total scattering study. *J. Am. Chem. Soc.*, 134:6785 – 6792, 2012.

[Jeong *et al.*, 1999] I.-K. Jeong, Th. Proffen, F. Mohiuddin-Jacobs, and S. J. L. Billinge. Measuring correlated atomic motion using x-ray diffraction. *J. Phys. Chem. A*, 103:921–924, 1999.

[Jeong *et al.*, 2001] I.-K. Jeong, F. Mohiuddin-Jacobs, V. Petkov, S. J. L. Billinge, and S. Kycia. Local structure study of $In_xGa_{1-x}As$ semiconductor alloys using high energy synchrotron X-ray diffraction. *Phys. Rev. B*, 63:205202, 2001.

[Jeong *et al.*, 2003] I. K. Jeong, R. H. Heffner, M. J. Graf, and S. J. L. Billinge. Lattice dynamics and correlated atomic motion from the atomic pair distribution function. *Phys. Rev. B*, 67:104301, 2003.

[Johnson *et al.*, 2002] J. C. Johnson, H. Yan, R. D. Schaller, P. B. Petersen, P. Yang, and R. J. Saykally. Near-field imaging of nonlinear optical mixing in single zinc oxide nanowires. *Nano Lett.*, 2:279–283, Apr. 2002.

[Juhás *et al.*, 2006] P. Juhás, D. M. Cherba, P. M. Duxbury, W. F. Punch, and S. J. L. Billinge. Ab initio determination of solid-state nanostructure. *Nature*, 440(7084):655–658, 2006.

[Juhas *et al.*, 2013] P. Juhas, T. Davis, C. L. Farrow, and S. J. L. Billinge. PDFgetX3: A rapid and highly automatable program for processing powder diffraction data into total scattering pair distribution functions. *J. Appl. Crystallogr.*, 46:560–566, 2013.

[Juhs *et al.*, 2015] Pavol Juhs, Christopher L. Farrow, Xiaohao Yang, Kevin R. Knox, and Simon J. L. Billinge. Complex modeling: a strategy and software program for combining multiple information sources to solve ill-posed structure and nanostructure inverse problems. *Acta Crystallogr. A*, 2015. accepted.

[Kang *et al.*, 2006] J. H. Kang, L. D. Menard, R. G. Nuzzo, and A. I. Frenkel. Unusual non-bulk properties in nanoscale materials: Thermal metal-metal bond contraction of γ-alumina-supported Pt catalysts. *J. Am. Chem. Soc.*, 128:12068–12069, 2006.

[Kara *et al.*, 2012] A. Kara, H. Enriquez, A. P. Seitsonen, L. C. Lew Yan Voon, S. Vizzini, B. Aufray, and H. Oughaddou. A review on silicene-new candidate for electronics. *Surf. Sci. Rep.*, 67:1–18, 2012.

[Kelley *et al.*, 2013] Anne Myers Kelley, Quanqin Dai, Zhong jie Jiang, Joshua A. Baker, and David F. Kelley. Resonance Raman spectra of wurtzite and zincblende CdSe nanocrystals. *Chem. Phys.*, 422:272–276, 2013.

[Kim *et al.*, 2008] Y.-I. Kim, S. Cadars, R. Shayib, T. Proffen, C. S. Feigerle, B. F. Chmelka, and R. Seshadri. Local structures of polar wurtzites studied by raman and ^{67}Zn/^{25}Mg NMR spectroscopies and by total neutron scattering. *Phys. Rev. B*, 78:195205, 2008.

[Klimov *et al.*, 2007] V. I. Klimov, S. A. Ivanov, J. Nanda, M. Achermann, I. Bezel, J. A. McGuire, and A. Pirystinski. Single-excition optical gain in semiconductor nanocrystals. *Nature*, 447:441–446, 2007.

[Kodama *et al.*, 2006] K. Kodama, S. Iikubo, T. Taguchi, and S. Shamoto. Finite size effects of nanoparticles on the atomic pair distribution functions. *Acta Crystallogr. A*, 62:444–453, 2006.

[Koga *et al.*, 2004] K. Koga, T. Ikeshoji, and K. Sugawara. Size- and temperature-dependent structural transitions in gold nanoparticles. *Phys. Rev. Lett.*, 92:115507, Jan. 2004.

[Kohn and Chumakov, 2000] V. G. Kohn and A. I. Chumakov. DOS: Evaluation of phonon density of states from nuclear resonant inelastic absorption. *Hyperfine Interact.*, 125:205, 2000.

[Kohn *et al.*, 2001] A. Kohn, F. Weigend, and R. Ahlrichs. Theoretical study on clusters of magnesium. *Phys. Chem. Chem. Phys.*, 3:711–719, Jan. 2001.

[Kootstra *et al.*, 2000] F. Kootstra, P. L. de Boeij, and J. G. Snijders. Application of time-dependent density-functional theory to the dielectric function of various nonmetallic crystals. *Phys. Rev. B*, 62:7071, 2000.

[Kresse and Furthmuller, 1996] G. Kresse and J. Furthmuller. Efficient iterative schemes for *abinitio* total-energy calculations using a plane-wave basis set. *Phys. Rev. B*, 54:11169 – 11186, 1996.

[Kuila *et al.*, 2012] T. Kuila, S. Bose, A. K. Mishra, P. Khanra, N. H. Kim, and J. H. Lee. Chemical functionalization of graphene and its applications. *Prog. Mater. Sci.*, 57:1061–1105, 2012.

[Kyratsi *et al.*, 2003] T. Kyratsi, K. Chrissafis, J. Wachter, K. M. Paraskevopoulos, and M. G. Kanatzidis. KSb_5S_8: A wide bandgap phase-change material for ultra high density rewritable information storage. *Adv. Mater.*, 15:1428–1431, 2003.

[Lai *et al.*, 1996] S. Lai, J. Guo, V. Petrova, G. Rammanath, and L. H. Allen. Size-dependent melting properties of small tin particles: Nanocalorimetric measurements. *Phys. Rev. Lett.*, 77:99–102, July 1996.

[Lane *et al.*, 2012] N. J. Lane, S. C. Vogel, G. Hug, A. Togo, L. Chaput, L. Hultman, and M. W. Barsoum. Neutron diffraction measurements and first-principles study of thermal motion of atoms in select $M_{n+1}AX_n$ and binary MX transition-metal carbide phases. *Phys. Rev. B*, 86:214301, 2012.

[Late *et al.*, 2012] D. J. Late, B. Liu, J. Luo, A. Yan, H. S. S. Ramakrishna Matte, M. Grayson, C. N. R. Rao, and V. P. Dravid. Gas and gase ultrathin layer transistors. *Adv. Mater.*, 24:3549–3554, July 2012.

[Lee *et al.*, 2009] D. C. Lee, J. M. Pietryga, I. Robel, D. J. Werder, R. D. Schaller, and V. I. Klimov. Colloidal synthesis of infrared-emitting germanium nanocrystals. *J. Am. Chem. Soc.*, 131:3436–3437, 2009.

[Lee *et al.*, 2010] C. Lee, H. Yan, L. E. Brus, T. F. Heinz, H. Hone, and S. Ryu. Anomalous lattice vibrations of single- and few-layer MoS_2. *ACS Nano*, 4:2695–2700, April 2010.

[Li *et al.*, 2011a] Chen W. Li, Xiaoli Tang, J. A. Munoz, J. B. Keith, S. J. Tracy, D. L. Abernathy, and B. Fultz. Structural relationship between negative thermal expansion and quartic anharmonicity of cubic ScF_3. *Phys. Rev. Lett.*, 107:195504, 2011.

[Li *et al.*, 2011b] Wei Li, Richard Harrington, Yuanzhi Tang, James D. Kubicki, Masoud Aryanpour, Richard J. Reeder, John B. Parise, and Brian L. Phillips. Differential pair distribution function study of the structure of arsenate adsorbed on nanocrystalline gamma-Alumina. *Environ. Sci. Technol.*, 45(22):9687–9692, 2011.

[Li *et al.*, 2013] X. Li, X. Hao, M. Zhao, Y. Wu, J. Yang, Y. Tian, and G. Qian. Exfoliation of hexagonal boron nitride by molten hydroxides. *Adv. Mater.*, 25:2200–2204, 2013.

[Lin *et al.*, 2014a] C. Lin, D. F. Kelley, M. Rico, and A. M. Kelley. The surface optical phonon in CdSe nanocrystals. *ACS Nano*, 8(4):3928–3938, 2014.

[Lin *et al.*, 2014b] Jung-Fu Lin, Junjie Wu, Jie Zhu, Zhu Mao, Ayman H. Said, Bogdan M. Leu, Jinguang Cheng, Yoshiya Uwatoko, Changqing Jin, and Jianshi Zhou. Abnormal elastic and vibrational behaviors of magnetite at high pressures. *Sci. Rep.*, 4:6282, 2014.

[Lu *et al.*, 2004] L. Lu, Y. Shen, X. Chen, L. Qian, and K. Lu. Ultrahigh strength and high electrical conductivity in copper. *Science*, 304:422–426, Apr. 2004.

[Lukatskaya *et al.*, 2013] M. R. Lukatskaya, O. Mashtalir, C. E. Ren, Y. Dall'Agnese, P. Rozier, P. L. Taberna, M. Naguib, P. Simon, M. W. Barsoum, and Y. Gogotsi. Cation intercalation and high volumetric capacitance of two-dimensional titanium carbide. *Science*, 341:1502, 2013.

[Lutterman *et al.*, 2009] Daniel A. Lutterman, Yogesh Surendranath, and Daniel G. Nocera. A self-healing oxygen-evolving catalyst. *J. Am. Chem. Soc.*, 131(11):3838–3839, 2009.

[Lyon and Somorjai, 1966] H. B. Lyon and G. A. Somorjai. Surface Debye temperatures of the (100), (111), and (110) faces of platinum. *J. Chem. Phys.*, 44:3707, 1966.

[Madelung *et al.*, 1982] O. Madelung, M. Schulz, and H. Weiss. *Number data and functional relationship in science and technology.* Springer, Berlin, 1982.

[Mal *et al.*, 2005] N. K. Mal, M. Fujiwara, and M. Matsukata. Synthesis of organic-inorganic hybrid mesoporous tin oxophosphate in the presence of anionic surfactant. *Chem. Commun.*, pages 5199–5201, 2005.

[Manaa, 2004] M. R. Manaa. Raman scattering of azafullerene $C_{48}N_{12}$. *Chem. Phys. Lett.*, 400(1-3):23–25, 2004.

[Manabe *et al.*, 1967] A. Manabe, A. Mitsuishi, and H. Yoshinaga. Infrared lattice reflection spectra of II-VI compounds. *Jpn. J. Appl. Phys.*, 6:593, 1967.

[Masadeh *et al.*, 2007] A. S. Masadeh, E. S. Božin, C. L. Farrow, G. Paglia, P. Juhás, A. Karkamkar, M. G. Kanatzidis, and S. J. L. Billinge. Quantitative size-dependent structure and strain determination of CdSe nanoparticles using atomic pair distribution function analysis. *Phys. Rev. B*, 76:115413, 2007.

[Mashtalir *et al.*, 2013a] O. Mashtalir, M. Naguib, B. Dyatkin, Y. Gogotsi, and M. W. Barsoum. Kinetics of aluminum extraction from Ti_3AlC_2 in hydrofluoric acid. *Mater. Chem. Phys.*, 139:147–152, 2013.

[Mashtalir *et al.*, 2013b] O. Mashtalir, M. Naguib, V. N. Mochalin, Y. Dall'Agnese, M. Heon, M. W. Barsoum, and Y. Gogotsi. Intercalation and delamination of layered carbides and carbonitrides. *Nat. Commun.*, 4:1716, 2013.

[Matte *et al.*, 2011] H. S. S. Ramakrishna Matte, B. Plowman, R. Datta, and C. N. R. Rao. Graphene analogues of layered metal selenides. *Dalton Trans.*, 40:10322–10325, 2011.

[McAlpin *et al.*, 2010] J. Gregory McAlpin, Yogesh Surendranath, Mircea Dinca, Troy A. Stich, Sebastian A. Stoian, William H. Casey, Daniel G. Nocera, and R. David Britt. Epr evidence for Co(IV) species produced during water oxidation at neutral pH. *J. Am. Chem. Soc.*, 132(20):6882–6883, 2010.

[McGreevy and Pusztai, 1988] R. L. McGreevy and L. Pusztai. Reverse Monte Carlo simulation: a new technique for the determination of disordered structures. *Mol. Simul.*, 1:359–367, 1988.

[Micic *et al.*, 1994] O. I. Micic, C. J. Curtis, K. M. Jones, J. R. Sprague, and A. J. Nozik. Synthesis and characterization of InP quantum dots. *J. Phys. Chem.*, 98:4966–4969, 1994.

[Mino *et al.*, 2013] L. Mino, G. Agostini, E. Borfecchia, D. Gianolio, A. Piovano, E. Gallo, and C. Lamberti. Low-dimensional systems investigated by x-ray absorption spectroscopy: a selection of 2D, 1D and 0D cases. *J. Phys. D: Appl. Phys.*, 46:423001, 2013.

[Mohr and Thomsen, 2009] Marcel Mohr and Christian Thomsen. Phonons in bulk CdSe and CdSe nanowires. *Nanotechnology*, 20:115707, 2009.

[Murphy *et al.*, 2006] J. E. Murphy, M. C. Beard, A. G. Norman, S. P. Ahrenkiel, J. C. Johnson, P. Yu, O. I. Micic, R. J. Ellington, and A. J. Nozik. Pbte colloidal nanocrystals: synthesis, characterization, and multiple exciton generation. *J. Am. Chem. Soc.*, 128:3241–3247, 2006.

[Murray *et al.*, 1993] C. B. Murray, D. J. Norris, and M. G. Bawendi. Synthesis and characterization of nearly monodisperse CdE (E = S, Se, Te) semiconductor nanocrystallites. *J. Am. Chem. Soc.*, 115:8706–8715, 1993.

[Naguib *et al.*, 2011] M. Naguib, M. Kurtoglu, V. Presser, J. Lu, J. Niu, M. Heon, L. Hultman, Y. Gogotsi, and M. W. Barsoum. Two-dimensional nanocrystals produced by exfoliation of Ti_3AlC_2. *Adv. Mater.*, 23:4248–4253, 2011.

[Naguib *et al.*, 2012a] M. Naguib, J. Come, B. Dyatkin, V. Presser, P. L. Taberna, M. W. Barsoum, and Y. Gogotsi. MXene: a promising transiton metal carbide anode for lithium-ion batteries. *Electrochem. Commun.*, 16:61–64, 2012.

[Naguib *et al.*, 2012b] M. Naguib, O. Mashtalir, J. Carle, V. Presser, J. Lu, L. Hultman, Y. Gogotsi, and M. W. Barsoum. Two-dimensional transition metal carbides. *ACS Nano*, 6:1322–1331, 2012.

[Naguib *et al.*, 2013] M. Naguib, J. Halim, J. Lu, K. Cook, L. Hultman, Y. Gogotsi, and M. W. Barsoum. New two-dimensional niobium and vanadium carbides as promising materials for Li-ion batteries. *J. Am. Chem. Soc.*, 135:15966–15969, 2013.

[Naguib *et al.*, 2014] M. Naguib, V. N. Mochalin, M. W. Barsoum, and Y. Gogotsi. MXenes: A new family of two-dimensional materials. *Adv. Mater.*, 26:992–1005, 2014.

[Neder and Proffen, 2008] Reinhard B. Neder and Thomas Proffen. *Diffuse Scattering and Defect Structure Simulations: A cook book using the program DISCUS*. Oxford University Press, Oxford, 2008.

[Novoselov *et al.*, 2004] K. S. Novoselov, A. K. Geim, S. V. Morozov, D. Jiang, Y. Zhang, S. V. Dubonos, I. V. Grigorieva, and A. A. Firsov. Electric field effect in atomically thin carbon films. *Science*, 306:666–669, 2004.

[Novoselov *et al.*, 2005] K. S. Novoselov, D. Jiang, F. Schedin, T. J. Booth, V. V. Khotkevich, S. V. Morozov, and A. K. Geim. Two-dimensional atomic crystals. *Proc. Natl. Acad. Sci. USA*, 102:10451–10453, 2005.

[O'Neill *et al.*, 2012] A. O'Neill, U. Khan, and J. N. Coleman. Preparation of high concentration dispersions of exfoliated MoS_2 with increased flake size. *Chem. Mater.*, 24:2414–2421, 2012.

[Pacile *et al.*, 2008] D. Pacile, J. C. Meyer, C. O. Girit, and A. Zettl. The two-dimensional phase of boron nitride: Few-atomic-layer sheets and suspended membranes. *Appl. Phys. Lett.*, 92:133107, 2008.

[Padova *et al.*, 2011] P. D. Padova, C. Quaresima, B. Olivieri, P. Perfetti, and G. L. Lay. sp^2-like hybridization of silicon valence orbitals in silicene nanoribbons. *Appl. Phys. Lett.*, 98:081909, 2011.

[Pandey and Guyot-Sionnest, 2008] A. Pandey and P. Guyot-Sionnest. Slow electron cooling in colloidal quantum dots. *Science*, 322:929–932, 2008.

[Parala *et al.*, 2000] H. Parala, H. Winkler, M. Kolbe, A. Wohlfart, R. A. Fischer, R. Schmechel, and H. von Seggern. Confinement of CdSe nanoparticles inside MCM-41. *Adv. Mater.*, 12:1050–1055, July 2000.

[Peng and Peng, 2001] Z. A. Peng and X. Peng. Formation of high-quality CdTe, CdSe, and CdS nanocrystals using CdO as precursor. *J. Am. Chem. Soc.*, 123:183, 2001.

[Perry *et al.*, 2012] H. P. Perry, J. Law, J. Zon, and A. Clearfield. Porous zirconium and tin phosphonates incorporating 2,2'-bipyridine as supports for palladium nanoparticles. *Micropor. Mesopor. Mat.*, 149:172–180, 2012.

[Petkov *et al.*, 1999a] V. Petkov, R. G. DiFrancesco, S. J. L. Billinge, M. Acharya, and H. C. Foley. Local structure of nanoporous carbons. *Philos. Mag. B*, 79:1519, 1999.

[Petkov *et al.*, 1999b] V. Petkov, I.-K. Jeong, J. S. Chung, M. F. Thorpe, S. Kycia, and S. J. L. Billinge. High real-space resolution measurement of the local structure of $Ga_{1-x}In_xAs$ using X-ray diffraction. *Phys. Rev. Lett.*, 83(20):4089–4092, 1999.

[Petkov *et al.*, 2002a] V. Petkov, S. J. L. Billinge, T. Vogt, A. S. Ichimura, and J. L. Dye. Structure of intercalated Cs in zeolite ITQ-4: an array of metal ions and electrons confined in a pseudo-1D nanoporous host. *Phys. Rev. Lett.*, 89:075502, 2002. (Highlighted in Phys. Rev. Focus: http://focus.aps.org/story/v10/st4).

[Petkov *et al.*, 2002b] V. Petkov, P. N. Trikalitis, E. S. Božin, S. J. L. Billinge, T. Vogt, and M. G. Kanatzidis. Structure of $V_2O_5.nH_2O$ xerogel solved by the atomic pair distribution function technique. *J. Am. Chem. Soc.*, 124:10157, 2002.

[Pietryga *et al.*, 2004] J. M. Pietryga, R. D. Schaller, D. Werder, M. H. Stewart, V. I. Klimov, and J. A. Hollingsworth. Pushing the band gap envelope:mid-infrared emitting colloidal pbse quantum dots. *J. Am. Chem. Soc.*, 126:11752–11753, 2004.

[Poojary *et al.*, 1993] M. D. Poojary, H. L. Hu, F. L. Campbell, and A. Clearfield. Determination of crystal structures from limited powder data sets: crystal structure of zirconium phenylphosphonate. *Acta Crystallogr. B*, 49:996–1001, 1993.

[Poojary *et al.*, 1994] D. M. Poojary, B. Zhang, and A. Clearfield. Structure of a mixed phosphate/phosphonate layered zirconium compound from synchrotron x-ray powder diffraction data. *Angew. Chem. Int. Ed.*, 33(22):2324–2326, 1994.

[Poojary *et al.*, 1995] D. M. Poojary, B. Shpeizer, and A. Clearfield. X-ray powder structure and rietveld refinement of γ-zirconium phosphate, $Zr(PO_4)(H_2PO_4).2H_2O$. *J. Chem. Soc. Dalton Trans.*, pages 111–113, 1995.

[Pourbaix, 1974] M Pourbaix. *Atlas of Electrochemical Equilibria in Aqueous Solutions, 2nd ed.* National Association of Corrosion Engineers, Houston, TX, 1974.

[Proffen and Billinge, 1999] Th. Proffen and S. J. L. Billinge. PDFFIT, a program for full profile structural refinement of the atomic pair distribution function. *J. Appl. Crystallogr.*, 32:572–575, 1999.

[Purans *et al.*, 2007] J. Purans, A. Kuzmin, E. Cazzanelli, and G. Mariotto. Disorder-induced raman scattering in rhenium trioxide (ReO_3). *J. Phys.: Condens. Mat.*, 19:226206, 2007.

[Rabani, 2002] E. Rabani. An interatomic pair potential for cadmium selenide. *J. Chem. Phys.*, 116:258, 2002.

[Roduner, 2006a] E Roduner. *Nanoscopic materials: Size-Dependent Phenomena*. The Royal Society of Chemistry, Cambridge, 2006.

[Roduner, 2006b] Emil Roduner. Size matters: why nanomaterials are different. *Chem. Soc. Rev.*, 35:583–592, May 2006.

[Rossetti *et al.*, 1983] R. Rossetti, S. Nakahara, and L. E. Brus. Quantum size effects in the redox potentials, resonance raman spectra, and electronic spectra of cds crystallites in aqueous solution. *J. Chem. Phys.*, 79:1086, 1983.

[Rui *et al.*, 2013] X. Rui, Z. Lu, H. Yu, D. Yang, H. Hng, T. M. Lim, and Q. Yan. Ultrathin v_2o_5 nanosheet cathodes: realizing ultrafast reversible lithium storage. *Nanoscale*, 5:556–560, 2013.

[Sanchez *et al.*, 2009] S. I. Sanchez, L. D. Menard, A. Bram, J. H. Kang, M. W. Small, R. G. Nuzzo, and A. I. Frenkel. The emergence of nonbulk properties in supported metal clusters: Negative thermal expansion and atomic disorder in pt nanoclusters supported on γ-Al_2O_3. *J. Am. Chem. Soc.*, 131:7040–7054, May 4 2009.

[Sarasamak *et al.*, 2010] K. Sarasamak, S. Limpijumnong, and W. R. L. Lambrecht. Pressure-dependent elastic constants and sound velocities of wurtzite SiC, GaN, InN, ZnO, and CdSe, and their relation to the high-pressure phase transition: A first-principles study. *Phys. Rev. B*, 82:035201, Jul 2010.

[Schowalter *et al.*, 2009] M. Schowalter, A. Rosenauer, J. T. Titantah, and D. Lamoen. Computation and parametrization of the temperature dependence of Debye-Waller factors for group IV, III-V and II-VI semiconductors. *Acta Crystallogr. A*, 65:5–17, 2009.

[Schroedter *et al.*, 2002] A. Schroedter, H. Weller, R. Eritja, W. E. Ford, and J. M. Wessels. Biofunctionalization of silica-coated CdTe and gold nanocrystals. *Nano Lett.*, 2:1363–1367, Dec. 2002.

[Scopigno *et al.*, 2011] T. Scopigno, W. Steurer, S. N. Yannopoulos, A. Chrissanthopoulos, M. Krisch, G. Ruocco, and T. Wagner. vibrational dynamics and surface structure of amorphous Se. *Nat. Commun.*, 2:195, 2011.

[Shi *et al.*, 2010] Y. Shi, C. Hamsen, X. Jia, K. K. Kim, A. Reina, M. Hofmann, A. L. Hsu, K. Zhang, H. Li, Z. Juang, M. S. Dresselhaus, L. Li, and J. Kong. Synthesis of few-layer hexagonal boron nitride thin film by chemical vapor deposition. *Nano Lett.*, 10:4134–4139, 2010.

[Shi *et al.*, 2013] Chenyang Shi, Erin L. Redmond, Amir Mazaheripour, Pavol Juhás, Thomas F. Fuller, and Simon J. L. Billinge. Evidence for anomalous bond softening and disorder below 2 nm diameter in carbon supported platinum nanoparticles from the temperature dependent peak width of the atomic pair distribution function. *J. Phys. Chem. C*, 117:7226–7230, 2013.

[Shi *et al.*, 2014] Chenyang Shi, Majid Beidaghi, Michael Naguib, Olha Mashtalir, Yury Gogotsi, and Simon J. L. Billinge. Structure of nanocrystalline Ti_3C_2 MXene using atomic pair distribution function. *Phys. Rev. Lett.*, 112:125501, 2014.

[Singh *et al.*, 2011] V. Singh, D. Joung, L. Zhai, S. Das, S. I. Khondaker, and S. Seal. Graphene based materials: past, present and future. *Prog. Mater. Sci.*, 56:1178–1271, 2011.

[Stankov *et al.*, 2008] S. Stankov, Y. Z. Yue, M. Miglierini, B. Sepiol, I. Sergueev, A. I. Chumakov, L. Hu, P. Svec, and R. Rüffer. Vibrational properties of nanograins and interfaces in nanocrystalline materials. *Phys. Rev. Lett.*, 100:235503, June 1 2008.

[Stoffel *et al.*, 2010] R. P. Stoffel, C. Wessel, M. Lumey, and R. Dronskowski. *abinitio* thermochemistry of solid-state materials. *Angew. Chem. Int. Ed.*, 49:5242–5266, 2010.

[Subbiah *et al.*, 2005] A. Subbiah, D. Pyle, A. Rowland, J. Huang, R. A. Narayanan, P. Thiyagarajan, J. Zon, and A. Clearfield. A family of microporous materials formed by Sn(IV) phosphonate nanoparticles. *J. Am. Chem. Soc.*, 127:10826–10827, 2005.

[Tang and Zhou, 2013] Q. Tang and Z. Zhou. Graphene-analogous low-dimensional materials. *Prog. Mater. Sci.*, 58:1244–1315, 2013.

[Tang *et al.*, 2012] Q. Tang, Z. Zhou, and P. Shen. Are mxenes promising anode materials for Li ion batteries? computational studies on electronic properties and Li storage capabilities of Ti_3C_2 and $Ti_3C_2X_2$ (X=F,OH) monolayer. *J. Am. Chem. Soc.*, 134:16909–16916, 2012.

[Tang *et al.*, 2013] Q. Tang, Z. Zhou, and Z. Chen. Graphene-related nanomaterials: tuning properties by functionalization. *Nanoscale*, 5:4541–4583, 2013.

[Teweldebrhan *et al.*, 2010] D. Teweldebrhan, V. Goyal, and A. A. Balandin. Exfoliation and characterization of bismuth telluride atomic quintuples and quasi-two-dimensional crystals. *Nano Lett.*, 10:1209–1218, March 2010.

[Thorpe *et al.*, 2002] M. F. Thorpe, V. A. Levashov, M. Lei, and S. J. L. Billinge. Notes on the analysis of data for pair distribution functions. In S. J. L. Billinge and M. F. Thorpe, editors, *From semiconductors to proteins: beyond the average structure*, pages 105–128, New York, 2002. Kluwer/Plenum.

[Tiano *et al.*, 2015] Amanda L. Tiano, Georgia C. Papaefthymiou, Crystal S. Lewis, Jinkyu Han, Cheng Zhang, Qiang Li, Chenyang Shi, A. M. Milinda Abeykoon, Simon J. L. Billinge, Eric Stach, Justin Thomas, Kevin Guerrero, Pablo Munayco, Jimmy Munayco, Rosa B. Scorzelli, Philip Burnham, Arthur J. Viescas, and Stanislaus S. Wong. Correlating size and composition-dependent effects with magnetic, Mössbauer, and pair distribution function measurements in a family of catalytically active ferrite nanoparticles. *Chem. Mater.*, 27:3572–3592, 2015.

[Togo *et al.*, 2008] A. Togo, F. Oba, and I. Tanaka. First-principles calculations of the ferroelastic transition between rutile-type and $CaCl_2$-type SiO_2 at high pressures. *Phys. Rev. B*, 78:134106, Oct 2008.

[Tucker *et al.*, 2007] Matthew G. Tucker, David A. Keen, Martin T. Dove, Andrew L. Goodwin, and Qun Hui. RMCProfile: reverse Monte Carlo for polycrystalline materials. *J. Phys.: Condens. Mat.*, 19:335218, 2007.

[Ueno *et al.*, 2006] A. Ueno, T. Fujita, M. Matsue, H. Yanagisawa, C. Oshima, F. Patthey, H. C. Ploigt, W. D. Schneider, and S. Otani. Scanning tunneling microscopy study on a BC_3 covered NbB_2 (0001) surface. *Surf. Sci.*, 600:3518–3521, 2006.

[Unruh *et al.*, 1993] K.M. Unruh, T.E. Huber, and C.A. Huber. Melting and freezing behavior of indium metal in porous glasses. *Phys. Rev. B*, 48:9021–9027, 1993.

[Valden *et al.*, 1998] M. Valden, X. Lai, and D. W. Goodman. Onset of catalytic activity of gold clusters on titania with the appearance of nonmetallic properties. *Science*, 281:1647–1650, September 1998.

[Vivani *et al.*, 2008] R. Vivani, G. Alberti, F. Costantino, and M. Nocchetti. New advances in zirconium phosphate and phosphonate chemistry: structural archetypes. *Micropor. Mesopor. Mat.*, 107:58–70, 2008.

[Wang *et al.*, 2003] Z. Wang, J. M. Heising, and A. Clearfield. Sulfonated microporous organic-inorganic hybrids as strong bronsted acids. *J. Am. Chem. Soc.*, 125:10375–10383, 2003.

[Wang *et al.*, 2005] Y. Wang, X. Xie, and T. Goodson. Enhanced third-order nonlinear optical properties in dendrimer-metal nanocomposites. *Nano Lett.*, 5:2379–2384, Dec. 2005.

[Wei *et al.*, 2012] H. H. Wei, C. M. Evans, B. D. Swartz, A. J. Neukirch, J. Young, O. V. Prezhdo, and T. D. Krauss. Colloidal semiconductor quantum dots with tunable surface composition. *Nano Lett.*, 12:4465–4471, 2012.

[Widulle *et al.*, 1999] F. Widulle, S. Kramp, N. M. Pyka, A. Göbel, T. Ruf, A. Debernardi, R. Lauck, and M. Cardona. The phonon dispersion of wurtzite CdSe. *Physica B*, 263-264:448–451, 1999.

[Wood *et al.*, 2002] I. G. Wood, K. S. Knight, G. D. Price, and J. A. Stuart. Thermal expansion and atomic displacement parameters of cubic $KMgF_3$ perovskite determined by high-resolution neutron powder diffraction. *J. Appl. Crystallogr.*, 35:291–295, 2002.

[Xie and Kent, 2013] Y. Xie and P. R. C. Kent. Hybrid density functional study of structural and electronic properties of functionalized $Ti_{n+1}X_n$ (X = C, N) monolayers. *Phys. Rev. B*, 87:235441, June 2013.

[Yang *et al.*, 2013] Xiaohao Yang, Ahmad S. Masadeh, James R. McBride, Emil S. Božin, Sandra J. Rosenthal, and Simon J. L. Billinge. Confirmation of disordered structure of ultrasmall CdSe nanoparticles from x-ray atomic pair distribution function analysis. *Phys. Chem. Chem. Phys.*, 15(22):8480–8486, 2013.

[Yang *et al.*, 2015] Xiaohao Yang, Pavol Juhas, Christopher Farrow, and Simon J. L. Billinge. xPDFsuite: an end-to-end software solution for high throughput pair distribution function transformation, visualization and analysis. *arXiv*, 2015. 1402.3163.

[Young and Goodwin, 2011] Callum A. Young and Andrew L. Goodwin. Applications of pair distribution function methods to contemporary problems in materials chemistry. *J. Mater. Chem.*, 21:6464–6476, 2011.

[Zachariasen, 2004] W. H. Zachariasen. *Theory of X-Ray Diffraction in Crystals*. Dover Publications, 2004.

[Zeng *et al.*, 2011] Z. Zeng, Z. Yin, X. Huang, H. Li, Q. He, G. Lu, F. Boey, and H. Zhang. Single-layer semiconducting nanosheets: high-yield preparation and device fabrication. *Angew. Chem. Int. Ed.*, 50:11093–11097, 2011.

[Zhan *et al.*, 2012] Y. Zhan, Z. Liu, S. Najmaei, P. M. Ajayan, and J. Lou. Large-area vapor-phase growth and characterization of MoS_2 atomic layers on a SiO_2 substrate. *Small*, 8:966–971, 2012.

[Zhou *et al.*, 2013] X. W. Zhou, D. K. Ward, J. E. Martin, F. B. van Swol, J. L. Cruz-Campa, and D. Zubia. Stillinger-Weber potential for the II-VI elements Zn-Cd-Hg-S-Se-Te. *Phys. Rev. B*, 88:085309, 2013.

[Zhu *et al.*, 2014] Mengqiang Zhu, Paul Northrup, Chenyang Shi, Simon J. L. Billinge, Donald L. Sparks, and Glenn A. Waychunas. The structure of sulfate adsorption complexes on ferrihydrite. *Environ. Sci. Technol. Lett.*, 1:97–101, 2014.